Integrated Sensor-based Condition Monitoring in Advanced Manufactured 3D-Printed Equipment

by

M. I. N. P. Munasinghe

A thesis submitted in partial fulfilment of the
requirements for the degree of Doctor of Philosophy

at the
Centre for Autonomous Systems
Faculty of Engineering and Information Technology
University of Technology Sydney

September 2021

Certificate of Original Authorship

I, M. I. N. P. Munasinghe declare that this thesis, is submitted in fulfilment of the requirements for the award of Doctor of Philosophy, in the School of Mechanical and Mechatronic Engineering, Faculty of Engineering and Information Technology at the University of Technology Sydney.

This thesis is wholly my own work unless otherwise referenced or acknowledged. In addition, I certify that all information sources and literature used are indicated in the thesis. This document has not been submitted for qualifications at any other academic institution.

This research is supported by the Australian Government Research Training Program, The Commonwealth of Australia's Department of Industry, Innovation and Science (Innovative Manufacturing CRC Ltd) and Downer, via its subsidiary Mineral Technologies.

Production Note:
Signed: Signature removed prior to publication.

Date: 28/09/2021

Integrated Sensor-based Condition Monitoring in Advanced Manufactured 3D-Printed Equipment

by

M. I. N. P. Munasinghe

A thesis submitted in partial fulfilment of the requirements for the degree of Doctor of Philosophy

Abstract

The future vision of advanced manufacturing is one of connected smart manufacturing equipment that takes advantage of data capture and analysis systems to optimise operations. Australia's manufacturing sector is a vital component of the economy. A key to progress is the application of advanced manufacturing technologies, systems and processes. Additive Manufacturing (AM), also known as 3D printing, is an advanced manufacturing technology that plays a significant role in the fourth industrial revolution (Industry 4.0). In recent years, manufacturers in the mining sector have been looking to leverage advanced manufacturing technologies to help improve productivity, efficiency and safety. Gravity Separation Spirals (GSS) are vital to mineral processing operations in the mining sector for separating mineral-rich slurry into its different density components, particularly when high throughput is required. GSS have traditionally been manufactured in moulds, using a manual process that is subject to numerous inherent drawbacks, including significant tooling costs, limited customisation, and the risk of worker exposure to hazardous materials.

A multi-partner project is underway to develop a bespoke 3D printer to print an upgraded and customisable GSS. By embedding Internet of Things (IoT) sensors inside the GSS, it is possible to remotely determine the operation conditions, perform predictive maintenance, and use the collected data to optimise the production output. The research in this thesis

is focused on developing the required sensors that can be embedded in the printed spiral. These sensors can be either 3D printed or conventional sensors. Research also focuses on the sensor placement problem to determine the ideal location to place sensors so as to maximise the information gain whilst simultaneously considering the 3D printing process, and the required structural integrity. In order to print the structure with the sensors inline, a novel radial slicing algorithm has been devised to slice helical objects, along with a path planning algorithm for radial robot-based 3D printing.

Experiments using conductive filament have shown how the devised 3D printed sensors can be used to measure, with acceptable accuracy, the required physical quantities, such as strain, temperature, and vibration. The design of the traditional 3D strain sensor has been improved to compensate for temperature changes. A partial pipe flow meter has been developed based on ultrasonic velocity measurement and capacitance level sensing. Experimental results showed that this sensor performed better than a conventional flow meter. The devised voxel-based sensor placement approach has been shown to propose ideal locations that consider various competing objectives. Then, in combination with the proposed radial slicing algorithm, the proposed cost-based path planning approach is able to print the structure accurately in the developed simulation environment.

This thesis presented novel sensors and approaches, verified by experiments, for the strategic placement of 3D printed sensors combined with conventional sensors, in radially 3D printed objects, which are sliced for robot path planning, and hence furthers the new era of large-scale smart, connected, bespoke manufactured equipment.

Acknowledgements

I would like to thank my principal supervisor, Dr Gavin Paul for providing all the support and guidance he has provided throughout the degree, and for the amount of valuable time he spent on my research.

Thanks to the team at Centre for Autonomous Systems (CAS) and my co-supervisor, Dr Ying He for providing feedback related to my research.

Thank you to Rapido, in particular, Hervé Harvard and Michael Behrens for establishing this overall research activity and leading the overall R&D engineering project.

Thanks to the students: Matthew Woods, Joel Marini and John Masangkay, who worked with me in various parts of my research.

Thanks to my friend Lewis Miles, for providing help and support in my research.

Thanks to my family, especially my mother, for motivating me, and supporting me throughout my education.

This thesis was edited by Elite Editing, and editorial intervention was restricted to Standards D and E of the *Australian Standards for Editing Practice*.

Contents

List of Figures

List of Tables

Acronyms & Abbreviations

ABS	Acrylonitrile Butadiene Styrene
AE	Acoustic Emission
AM	Additive Manufacturing
CAD	Computer-aided Design
CAS	Centre for Autonomous Systems
CNC	Computer Numerical Control
CPS	Cyber-Physical Systems
CSIRO	Australian Commonwealth Scientific and Industrial Research Organisation
DAQ	Data Acquisition Device
DH	Denavit–Hartenberg
DOF	Degrees of Freedom
DW	Direct Wire
FBG	Fibre Bragg Grating
FDM	Fused Deposition Modelling
FEA	Finite Element Analysis
FEM	Finite Element Model
FK	Forward Kinematics

GSS Gravity Separation Spirals

IE Information Entropy

IK Inverse Kinematics

IMCRC Innovative Manufacturing Cooperative Research Centre

IoT Internet of Things

LENS Laser Engineered Net Shaping

LOM Laminated Object Manufacturing

LSS Large Space Structures

LVDT Linear Variable Differential Transformer

MT Mineral Technologies, a subsidiary of Downer EDI Limited

OSP Optimal Sensor Placement

PCB Printed Circuit Board

PLA Polylactic Acid Base

PLY Polygon File Format

PRM Probabilistic Road Maps

RMS Root Mean Square

SHM Structural Health Monitoring

SLA Stereolithography Apparatus

SLS Selective Laser Sintering

STL Standard Triangulation Language

TCR Temperature Coefficient of Resistance

UTS University of Technology Sydney

Chapter 1

Introduction

Advanced manufacturing technologies are transforming industries around the world. They can enhance output, increase value and flexibility, while reducing the time-to-market, material waste and under-utilised equipment. Advanced manufacturing can accommodate the varying production and mass customisation that is increasingly important to many companies, even without large capital investment. It encompasses all aspects of the value chain from concept to end-of-life considerations and, relies on information and communication technologies to integrate business activities and manufacturing processes for seamless operation [13].

Over the next 20 years, Australia's manufacturing industry is set to transform into an integrated, collaborative and export-focused industry, providing customised, high-value solutions within global value chains. Australian manufacturing will be a thriving component in the economy through advanced manufacturing technologies, systems and processes. The advanced manufacturing sector will focus on pre- (R&D, design) and post-production value-adding, customised manufacturing with high margins, low volumes and sustainable manufacturing [14].

Additive manufacturing has started to gain popularity because of its many advantages over traditional manufacturing methods. Embedding sensors inside 3D-printed equipment and gathering data is essential for applications like predictive maintenance. This thesis focuses on developing sensors that can measure various parameters of 3D printed equipment, and

on the optimal placement of 3D printed sensors to increase their information gain while considering the constraints. It also presents a method of slicing and optimal print-head path planning for radial 3D printing of objects that can incorporate the sensors.

Placing 3D printed sensors directly into the equipment rather than embedding conventional sensors has many advantages. Most significantly, 3D printed sensors are low-cost and can be integrated into the large volume of the structural material without compromising the equipment's mechanical integrity. Therefore, the development of 3D printed sensors to measure the required parameters—such as strain, wear, vibration and temperature using conductive filaments—has been investigated.

In this research, radial printing has been used for an industrial application. As distinct from traditional vertical slicing, a novel radial slicing algorithm has been developed specifically for the application. To reduce print failures, an optimal path planning method for 3D printing has also been proposed. Identifying optimal locations in a 3D printed object in which to place sensors is vital to collecting quality information. Therefore, an optimal sensor placement algorithm for placing 3D printed sensors in a 3D printed object has been developed and tested. This algorithm considers factors like information gain and the ability to print a sensor in a given location and it penalises areas in which sensors should not be placed for a variety of reasons, including an undesirable impact on the object's structural integrity.

1.1 Background

Additive Manufacturing (AM), widely known as 3D printing, is the process of the conversion of Computer-aided Design (CAD) to a printed physical object. AM has evolved from a prototyping tool to manufacture finished products [15]. The main advantage of AM, in contrast to other manufacturing methods, is the ability to readily achieve mass customisation. Since the shape or the dimensions of the physical printed object depend on the CAD model, by changing a CAD model, it is possible to change the printed object as required. Additionally, AM can be used to manufacture optimised components, which would otherwise be difficult to produce using traditional manufacturing methods.

Therefore, many industries have begun to adopt AM into their manufacturing practices. Examples of such industries include the construction, medical and aerospace sectors. The construction industry uses AM for customised parts, in situ repair and topology optimisation [16]. AM enables the creation of sophisticated and intricate components; the medical industry uses it in various applications, such as customised airway stents [17]. The ability to print hollow structures with stronger materials has made it possible to improve the power-to-weight ratio in aerospace applications [18]. Another crucial advantage of using AM in the aerospace industry is the ability to combine multiple components into one, reducing the complexity of the assembly process.

The number of IoT-based applications has undergone a significant increase over the past decade. In 2017, there are approximately 6.4 billion IoT devices and that number is increasing rapidly [19]. The combination of Cyber-Physical Systems (CPS) and IoT has been applied to the industrial domain and led the fourth industrial revolution, also known as Industry 4.0. This new industrial revolution has resulted in smart products, smart production and smart services [20]. This thesis and project are aligned with smart products and the smart production components of Industry 4.0. Using IoT for industrial automation has made the collaboration of automation and heterogeneous systems more fault-tolerant, real-time and closed-loop [21]. Device collaboration and the exchange of data will reduce the requirement of manual labour to configure the equipment and the connection of many such units will provide valuable data that can be used to make smart applications [21]. Because of these advancements, many organisations have already started to consider IoT as a valuable addition to their businesses by combining interconnected machines and data analytics.

A combination of components manufactured using AM techniques with IoT-enabled sensors embedded into 3D printed components will produce smart industrial units that have advantages in both areas. This will help to develop IoT-enabled 3D printed products with greater customisation capabilities and complexity.

GSS comprise vital equipment in the mining industry for separating mineral-rich slurry into its components of different density. When the slurry is poured into the top, the spiral slope naturally separates the slurry according to its different particle densities. The sizes

(a) (b)

FIGURE 1.1: a) GSS manufacturing factory floor. b) Bank of GSS in the field.

of these GSS vary, depending on the application and, ideally, the spiral profile can be modified slightly for every single customer, depending on the composition of their slurry and their desired outcomes. Images of GSS are shown in Fig. 1.1. These GSS are used in various mining locations all around the world, such as in South Africa, the US, India, Brazil and Australia.

This thesis is part of a project conducted at University of Technology Sydney (UTS) with UTS Rapido and supported by the Innovative Manufacturing Cooperative Research Centre (IMCRC) and the industry partner, Mineral Technologies, a subsidiary of Downer EDI Limited (MT). The objective is to use AM to develop a bespoke 3D printer for GSS and to embed the required sensors inside it that will monitor its operational condition remotely and use the collected data to make decisions about, for example, predictive maintenance, online control and design improvements.

1.2 Motivation

At the moment, GSS are manufactured using moulding techniques. There are drawbacks inherent in this method. Mainly, the manufacturing cost of the spiral comprises 60% labour and 40% material. Therefore, to achieve a competitive price point in the international market, reducing manufacturing costs is crucial. Upgrading moulding techniques would result in expensive tooling costs and could impact lead times. The production output of a GSS is a measure of the spiral's ability to separate slurry into the important constituent

parts, and this depends greatly on the spiral's shape [22]. Therefore, to separate particular minerals from a variety of different slurries, the spiral's shape needs to be customised for each customer and location to obtain the optimal separation. Currently, when a new mineral type needs to be separated from the spiral, workers change the shape of the helix and test it. Based on the test results, workers tweak the shape to create the best separation, and this is stored in a limited database of designs. This process is difficult using the mould-based manufacturing method since different moulds must be created for different spiral shapes, which is expensive and time-consuming. Additionally, during this manufacturing process, toxic chemicals such as fibreglass and polyurethane need to be manually handled, risking the exposure of workers to hazardous chemicals. Therefore, transitioning to a new manufacturing method and up-skilling the labour force is vital.

Currently, all manufactured GSS are passive devices that are observed and operated manually. This is a labour-intensive process. Since these spirals operate in various remote mining locations worldwide, manual inspection is difficult and time-consuming. Inspection and maintenance often require equipment downtime, which interferes with production and, ultimately, leads to profit loss. Thus, the remote monitoring of GSS operation conditions has many advantages. Such monitoring enables the measurement of wear and creep in the GSS over time and opens up the possibility to address these issues accordingly. In situ and real-time monitoring will help with understanding improper use of the spiral, which can permanently damage the GSS—for example, via creep—and cause them to require replacement, costing both time and money. Additionally, collected data, especially concerning the wear of the spiral, can be used to refine the future design and manufacturing by refining the material or printing properties.

For these reasons and to increase production efficiency, there is a strong need to transform traditional manufacturing methods in the mining industry to more advanced manufacturing methods, while enabling manufactured equipment IoT to undertake monitoring, predictive maintenance and centralised control.

1.3 Scope

This research project's overall aim is to move towards a 3D-printed GSS, which is IoT enabled so that its operating conditions can be monitored remotely. To achieve this, various types of 3D printed and conventional sensors have been developed. These sensors can be used with any type of 3D printed object since they are not specific to GSS.

To print the GSS, it is necessary to slice the 3D spiral model. Therefore, a novel slicing algorithm has been developed to specifically slice helical shaped objects. The path planning algorithm for 3D printing has been developed specifically for use in robot-based 3D printing and is not generalisable to other 3D printers. Similarly, the sensor placement methodology developed to place 3D printed sensors is also for 3D printers that use a robotic arm.

1.4 Contributions

The main objective of this thesis is to present 3D printable and conventional sensors that have been researched and developed to measure the parameters that are important to GSS operation. Contributions 1-3 are related to this. Since the developed bespoke printer is a radial printer, it was necessary to develop a radial slicing algorithm and a path planning algorithm to print the spiral and these elements are related to Contribution 4. After developing 3D printable sensors, and developing algorithms to slice the object and plan the robot path, it was important to identify ideal locations to place the sensors, which is covered by Contribution 5.

The contributions of this thesis are as follows:

1. The design and testing of a 3D printable wear sensor that can measure the location and the depth of the wear, as well as a temperature sensor, a strain sensor and a sensor that integrates the strain, and temperature sensors to produce a temperature-compensated strain sensor [4–6, 8].

2. The design, simulation and characterisation of a 3D printed vibration sensor based on electromagnetism. The sensor consists of a 3D printed coil with a moving permanent magnet [7].

3. The design and testing of a partial pipe flow meter using a sensor fusion approach, which combines level sensing from the capacitance sensor and velocity measurements from an ultrasonic sensor [9].

4. A radial slicing algorithm for helical 3D printing as opposed to traditional horizontal slicing and an optimal path planning algorithm for robot-based radial 3D printing using print space sampling [10, 11].

5. A voxel-based method to optimise 3D-printed sensor placement in 3D printed objects, that considers sensor design, information gain, printability and placement constraints [12].

1.5 Publications

1. **Munasinghe, M.I.N.P.**, Miles, L. and Paul, G., 2019. Direct-write fabrication of wear profiling IoT sensor for 3D printed industrial equipment. In Proceedings of the 36th International Symposium on Automation and Robotics in Construction, (ISARC) 2019.

2. **Munasinghe, N.**, Woods, M., Miles, L. and Paul, G., 2019. 3-D printed strain sensor for structural health monitoring. In 2019 IEEE International Conference on Cybernetics and Intelligent Systems (CIS) and IEEE Conference on Robotics, Automation and Mechatronics (RAM) (pp. 275-280). IEEE.

3. **Munasinghe, N.** and Paul, G., 2019. Advanced Manufacturing of Spirals for Mineral Separation with Integrated Smart Sensing. IEEE UNITE 2019.

4. **Munasinghe, N.** and Paul, G., 2020. Ultrasonic-Based Sensor Fusion Approach to Measure Flow Rate in Partially Filled Pipes. IEEE Sensors Journal, 20(11), pp. 6083-6090.

5. **Munasinghe, N.**, and Paul, G., 2020. Radial Slicing for Helical-Shaped Advanced Manufacturing Applications. International Journal of Advanced Manufacturing Technology, 112(3–4), pp. 1089–1100.

6. **Munasinghe, N.**, and Paul, G., 2020. Path Planning for Robot Based Radial Advanced Manufacturing Using Print Space Sampling. In International Conference on Control, Automation, Robotics and Vision (ICARCV).

7. **Munasinghe, N.**, and Paul, G., 2020. Integrated 3-D Printable Temperature Sensor for Advanced Manufacturing. In Australasian Conference on Robotics and Automation (ACRA).

8. **Munasinghe, N.**, Masangkay, J., and Paul, G., 2021. Temperature Compensated 3D Printed Strain Sensor for Advanced Manufacturing Applications. In IEEE International Conference on Robotics and Automation (ICRA).

9. **Munasinghe, N.**, Romeijn, T., and Paul, G., 2021. Voxel-Based Sensor Placement for Additive Manufacturing Applications. Journal of Intelligent Manufacturing.

10. **Masangkay, J.**, Munasinghe, N., Watterson, P., and Paul, G., 2021. Simulation and Experimental Characterisation of a 3D-Printed Electromagnetic Vibration Sensor. Sensors and Actuators: A. Physical, *Under review.*

1.6 Thesis Outline

This thesis is structured so that the first two chapters provide the background, outline and related literature. Chapters 3 to 6 offer details about various 3D printable sensors and the conventional sensors developed. Chapter 7 presents the slicing algorithm, which results in the optimal path planning for 3D printing. Chapter 8 describes the sensor placement algorithm for 3D printed sensors. Finally, Chapter 9 draws conclusions and suggests possible future work. The detailed outline of each chapter is as follows:

Chapter 2 presents the related work on AM in industrial applications and discusses sensors in 3D printed objects, 3D printed sensors used to measure various parameters,

flow measurements in partially filled pipes, slicing and path planning for 3D printing and optimal sensor placement.

Chapter 3 presents the design, development and testing of a wear sensor that can be used to measure the depth as well as the location of the wear. This sensor was printed using a conductive filament, and its accuracy can be changed according to the requirements. This work has been published in [4].

Chapter 4 presents a 3D printable strain sensor that can be embedded inside a 3D printed object. It provides details about a strain sensor that can measure tensile strain and about another design for a 3D printed strain sensor, which is temperature compensated. This work has been published in [5, 6].

Chapter 5 presents two sensors that enable the monitoring and measurement of acute damage-causing characteristics. These embedded sensors can help to identify potential problems that were not anticipated during design, or damage caused by incorrect operation of the GSS equipment. The first is a vibration sensor that uses the principle of electromagnetic induction and details of the design, printing and testing of an embedded 3D printed temperature sensor printed inside a Polylactic Acid Base (PLA) base. This vibration sensor consists of a conductive coil printed with copper filament and a permanent magnet. This work is under review in [7]. The second monitoring sensor is a 3D printed temperature sensor which was printed using a carbon-based conductive filament and tested in a temperature-controlled insulated box. This work has been published in [8]. This chapter presents details of the design and characterisation of both the sensors.

Chapter 6 presents details of an improved flow meter that can measure the flow rate in a partially filled pipe, such as those that transfer slurry into or out of a GSS. This sensor fuses ultrasonic velocity measurements and capacitance-based liquid level measurements to calculate an accurate flow rate. This work has been published in [9].

Chapter 7 presents a novel algorithm for slicing 3D objects in a radial direction as opposed to traditional slicing, which occurs in the vertical direction. This chapter introduces the idea of using manipulability distribution for 3D printing to measure the dexterity of robot-based 3D printers. Then it builds on the idea of manipulability to propose a path planning

algorithm for robot-based 3D printing to overcome print failures. The proposed method depends on print space sampling and a multi-objective cost function to determine the optimal path. This work has been published in [10, 11].

Chapter 8 presents a voxel-based sensor placement methodology considering the information gain and the ability for printing and excluding areas where sensors should not be placed. This method uses the printability defined in Chapter 7. This work is under review in [12].

Chapter 9 summarises the research work presented in this thesis and discusses the limitations of the presented work. Conclusions are drawn from the research and potential future work is outlined.

Chapter 2

Review of Related Work

Advanced manufacturing refers to the technologies, processes, and systems used to transform current manufacturing methods by adding more value to the entire supply chain [23]. AM, widely known as 3D printing, is the process of creating 3D geometries from successive material addition [24]. AM has been applied to advanced manufacturing applications to reduce the manufacturing costs and allow advanced business models, such as customer-led design and just-in-time production [23]. AM has already been transformed from a rapid prototyping technology to an end-product manufacturing method [15]. The Australian Commonwealth Scientific and Industrial Research Organisation (CSIRO) states that the cost of manufacturing can be reduced by up to 70% by eliminating the tooling requirement [23]. Therefore, various industries, such as aerospace [18, 25], medicine [17] and construction [16, 26], have already started to adopt AM technologies.

2.1 Additive Manufacturing in Industrial Applications

AM has evolved beyond its use as a technology for rapid prototyping, and many industries are following the early trends for its adoption. The construction industry is one such industry. Potential applications of AM in the construction industry are in topology optimisation, customised parts, in-situ repair and tolerance matching. However, many of these

applications are still in a state of infancy because of a lack of standard quality assurance and testing [16].

AM has many applications in the field of medicine, for example, in neurosurgery [27], orthopaedics [28] and oral and maxillofacial surgeries [29]. The capacity to change the design quickly and to test it again, along with the ability to make sophisticated and intricate designs, has made AM suitable for medical applications. Cheng et al. [17] describe possible ways to use AM in developing customised and personalised airway stents. They show how a 3D printer is able to print the stent directly or the 3D printed model can be transformed into silicone using injection moulding. Further, 3D printing can be used to print moulds for soft tissue prostheses parts in the human body, such as ears, eyes and noses. These moulds and medical-grade silicone can then be employed to create soft prostheses. This method is cheaper than traditional approaches, with ear prosthesis fabrication costing around $30 [30].

In the area of autonomous aerial vehicles, researchers can now use AM to print UAV structures. They have used AM to develop a double structure for an outer shell, making the unit more lightweight and allowing it to be manufactured without any seams. Moreover, they were able to create internal trusses to make it more robust. Ultimately, they improved the UAV's power-to-weight ratio and performance by employing AM techniques [18]. Similarly, the aerospace and automobile industries also leverage the advantages of AM. These industries use AM to print aircraft engine components and specific automobile engine components. General Electric used 3D printed fuel nozzles in its LEAP engine, with each engine containing 19 of the nozzles. Without 3D printing, it would be necessary to combine 20 components to build a single fuel nozzle. Using 3D printing in these industries has achieved a 43% cycle time reduction and a 48% saving in costs [25].

2.2 Internet of Things in Industrial Applications

Industrial automation and industrial process management face a tremendous transformation with the introduction of IoT and CPS. The application of these technologies into the manufacturing and automation domain has led to the emergence of the 4^{th} generation of

manufacturing: Industry 4.0. This 4^{th} industrial revolution, which originated in Germany, has made it possible to manufacture smart products, to undertake smart production and to produce intelligent services [31]. Industrial IoT sensors and inter-machine collaboration techniques, incorporated with many other data collection and analysis methods, have been used to provide optimised operations and better services. IoT-based applications have generally shown significant improvement over the past decade and there are around 6.4 billion IoT-enabled devices worldwide as of 2017, a number that is increasing significantly [19]. With such advancements in the field, many organisations have begun to consider IoT as a value addition to their business strategies by combining advanced data analytics with interconnected machines. Primarily, in the industrial domain, the IoT can be used for remote location machine monitoring and operation, which is the primary focus of this research. Device collaboration to exchange the data will lead to reduced costs in manual engineering labour in terms of configuring the equipment and swathes of collected data from different units may be used to develop smart applications [32].

2.3 Embedding Sensors into 3D Printed Objects

Since AM can be used to manufacture sophisticated and customised objects, it is valuable to integrate sensing and actuator capabilities to achieve a tailored experience. Research work by Ota et al. [33] describes how they were able to develop a form-fitting glove, embedded with a heater and a temperature sensor, as well as other required electronics. To connect the different electronics, they used liquid metal-filled microchannels. Moreover, they were able to create a 3D printed resistor and capacitor, which could be integrated with other electronics. The resistor was developed using silicone oil and 20% carbon black and a condenser was formed using a cylindrical structure, where the inner and the outer conductive areas were filled with Galinstan material. They also developed a Galinstan-based dipole antenna and demonstrated how this antenna could be used to transmit video content in real time. Additionally, they used AM to print an embedded photodetection platform, which resembled the Sather Tower of the University of California, consisting of a current sensing circuit and the processed output from an external phototransistor.

In metallic AM, fibre sensors can be used to measure the temperature and strain in 3D printed profiles. In [34], IVG fibre was coated with electroplated nickel to withstand higher temperatures of around 1,600 ℃. Sandblasting was performed to improve the bonding between the sensor fibre and the 3D printed object. To test the sensors, an Laser Engineered Net Shaping (LENS), which is a powder-based AM process, was used to deposit a 50 x 120 x 2 mm^3 IN718 metal layer on a component in which the fibre sensors were embedded. An optical backscattering reflectometer was used, which utilised Rayleigh backscattering in the frequency domain to determine the temperature and the stress accumulated in the 3D printed object. It was possible to measure these parameters in the spatial resolution of 5 mm [34]. Another way of creating a strain sensor is by using straightforward printing that leverages conductor relations related to mechanical loading, geometry changes and piezoresistive effects. However, when this type of strain sensor is considered alongside metallic strain sensors, it becomes apparent that these are subjected to hysteresis, creep and non-linear responses [35].

Currently available technologies for embedding and connecting sensors can be categorised into the following three main areas:

1. Hybrid approaches that combine 3D printed parts with non-3D printed components, such as printed circuit boards or complete sensors.
2. Conductor infusions, which use printed channels filled with conductive ink.
3. Multi-material printing, which uses both conductive and non-conductive materials mainly in Fused Deposition Modelling (FDM).

The first method provides straightforward connections to components, but the potential of AM is not fully realised. Method 2 is challenging because it is difficult to fill the channels in a homogeneous manner with conductive ink, especially those channels that start to diverge. The main ways to infuse conductive material are suspension, for which the carrier remains in the liquid state; carrier solidified after infusion; and carrier evaporation after injection. The advantage of Method 3 is that it uses direct integration. However, the main disadvantage would be the lack of suitable material combinations. In both Methods

2 and 3, there can be a significant deviation in contact resistance, predominantly caused by temperature, mechanical loading and humidity changes. A combination of AM with the electronic component assembly can have benefits since conductors can be developed with materials suitable for the application. An example would be copper wiring being used to minimise losses by resistive heating. The main disadvantage of this method would be that it requires complicated mechatronic devices that can combine wire routing with the AM. Moreover, it does not provide full freedom to place the conductors [35].

Directly embedding Direct Wire (DW) into 3D printed components, as mentioned above, has disadvantages: the thermal sintering process of conductive material can degrade the polymeric 3D printed components; ink can spread because of the capillary effect; and the pausing required for the DW process in printing can weaken the bondings between layers and may create structural weak points. However, the use of print-stick-peal does not require any fabrication on the 3D printed object. Therefore, this process does not affect the surface finish of the 3D printed object or the temperature of the sintering. In this process, conductive lines are printed on lower surface energy substrates, which have higher glass transition temperatures. After that, they are sintered to the required temperature to obtain the optimal conductivity before the printed conductor pattern is then transformed into an actual 3D printed object. Rather than directly applying the conductive liquid to the 3D printed surface, the thin structure of the metal is transferred. This process has been used to embed one 3D printed stain sensor within another 3D printed object. However, this method has drawbacks, for example, the non-linear resistance response of the strain sensor and the occurrence of microcracks during the stretching can lead to an increase in resistance [36].

Researchers have utilised fibre optic sensors based on Fibre Bragg Grating (FBG) technology, which can be used to measure temperature, stress and strain in complex 3D printed objects using the powder bed-based AM method [37]. They carried out conventional 3D printing to place the fibre sensor until the plane in which the sensor should be embedded had been reached. Then they opened the printing chamber and placed the fibre. To ensure the correct placement of the fibre sensor, they printed an additional placeholder to hold the sensor. After the completion of the printing, this placeholder was then carefully removed.

(a) (b)

FIGURE 2.1: A smart screw developed using a multi-layer printing process [1]: a) Flex screw with an integrated sensor foil element; b) Screw sheared off at the position of the sensor and strain sensing resistor is marked with a white circle.

However, this method of placing sensors has disadvantages, for example, when the chamber is open, the printing object tends to curl because of the temperature difference on the surface. Studies found that when the fibre does not have enough tension, interference can occur with subsequent powder deposition [37]. The same technology-based strain sensors were also used in an FDM-based 3D process. The advantages of using this kind of sensor include its integration into locations where other sensors are difficult to place or that are inaccessible. The FBG sensor can be placed using glue on a slot shaped according to the sensor. In this method, the base of the groove of the sensor is printed first and then the printing process is paused and the FBG sensor is placed inside the groove with epoxy. Then, the printing process continues until the printing is finalised [38].

2.4 Smart 3D Printed Industrial Components

Joining the industrial components developed using AM and the technologies related to embedding sensors into 3D printed components will enable smart industrial components that combine the advantages of both areas. It is possible to develop IoT-enabled 3D printed products that have extensive customisation capabilities and complexity.

To combine 3D printed objects and sensors, one method is to print the component and the sensors in a single process. Despite having many advantages, using a single process will create many limitations in terms of scope and the materials that are viable to produce a

single part. This kind of limitation will affect the performance of the product and may, therefore, be unsuitable for certain applications [39].

Small industrial components have been developed by combining AM and sensor technologies. A smart screw was developed using AM and integrated sensors using a multi-layer printing process [1] as shown in Fig. 2.1. By integrating a thin foil resistive strain gauge inside the head of the screw, it was possible to determine the torsional moment by measuring the change in resistance. The fabrication of this screw involved three steps: preparing the strain gauge, 3D printing the screw and combining the sensor and screw during the printing process. The strain gauge was developed using carbon-based ink and foil. These two materials were combined using silver ink printed tracks. The screw was printed using a micro stereolithography printer. To place the sensor foil, the printing process was stopped and the sensor was manually placed on top of the washer disk [1].

Robots play a vital role in modern industrial manufacturing and the integrated sensor applications applied in this area. 3D printed tactile sensors were developed to detect contact and slips in robot grippers [40]. These sensors were developed using a mould and a customised printing approach called a direct print process. The material used was carbon nanotube-polymer composite. The fabricated sensors were of the resistance type and were attached to the robot gripper fingers; the generated signals were processed by collecting the analogue signals and converting them to digital signals. These signals were amplified, cleaned to reduce the noise and used to control the robot grip [40].

The automobile industry has many applications for AM-based smart components. Researchers developed 3D printed model tires with embedded 3D printable pressure sensors [41]. The "sensor" is a piezoresistive pressure sensor, capable of measuring the location of a force and the amount of force applied to the tire. It was developed using screen printing and moulding. An array of sensors was embedded inside the inner lining of the 3D printed tire, which was developed using flexible as well as a rigid material. These smart tires are capable of monitoring tire health as well as road conditions in real time. It is possible to measure various parameters, such as pressure, load, speed and location, and the tires can be used in robots and self-driving vehicles [41].

2.5 3D Printed Wear Sensors

The in-situ measurement of wear in industrial equipment has many advantages, including facilitating the capacity to make educated decisions about the adaptive control of different speeds and feeds to achieve the maximum production rate [42]. Additionally, detection of sudden equipment failure and the scheduling of planned maintenance [42]. Different methodologies have been used to detect wear in industrial equipment, such as radioactive techniques, optical scanning, temperature measurement and mechanical vibrations/sound analysis [42].

The Acoustic Emission (AE) is elastic wave propagation in the frequency range of 0.1 - 1 MHz, which is generated as a result of friction [43]. The AE of a part will change depending on the corrosion. Thus, capture and analysis has been used to identify wear in tools [44]. An AE-based wear sensor was developed by Douglas et al. [43] for piston rings.

A vibration-based wear sensor that detects low-frequency range micro-mechanical resonant vibrations was developed by Fritsch et al. [45]. A micromachined silicon structure was used to develop this sensor, which was applied to the anti-friction bearings of calendar rolls to characterise the vibrations used in the textile industry.

Electrical-based methods have been used for wear measurement in industrial components. To measure wear in the cylinders of engines, a resistance-based wear sensor was developed by Bödecker et al. [46]. This sensor helps to inspect the engine wear in situ without decommissioning the engine or expending significant resources. A conductive layer composed of resistive loops between insulating layers was used to manufacture the sensor. The wear was ascertained by measuring the change in resistance in these loops as they were worn away. A vacuum deposited wear sensor was developed by Ruff and Kreider using thin films [47]. This sensor consists of two conductive layers that lie on a thermocouple, separated by insulating layers. The same sensor can also be used for temperature measurement. Holger et al. [48] used a thin coated film-based wear sensor developed for cutting tools to measure wear in real time. This sensor was also based on the parallel resistors. Dyck et al. [49] developed a wear sensor that can measure the coefficient of friction for various coated geometries.

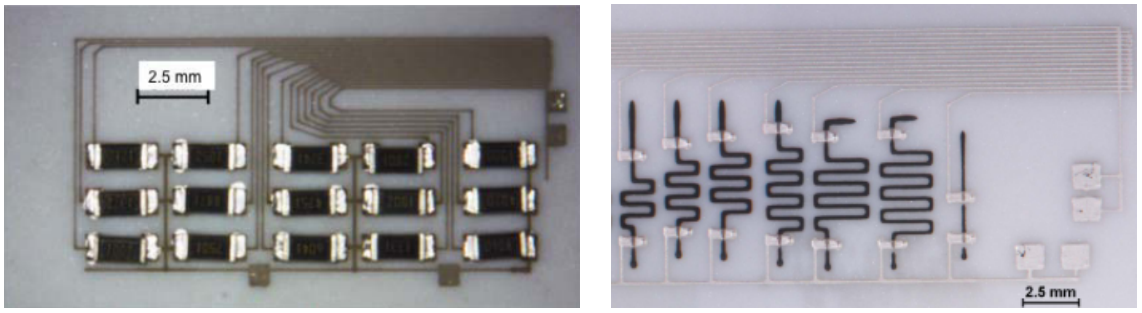

(a) (b)

FIGURE 2.2: Printed wear sensors developed by Dardona et al. [2]: a) Printed wear sensor with commercial resistors; b) Printed wear sensor with printed resistors.

A high-resolution wear sensor was developed by Shen et al. [50] based on silver traces. To achieve the full performance, the printing process required post-heat treatment. In this sensor, when the wear occurs, conductive traces, which are connected to resisters, are progressively removed, resulting in a change in the resistance. Therefore, the amount of wear can be identified by measuring the resistance. The same method has been used in both printed (Fig. 2.2b) and commercial resisters (Fig. 2.2a) by Dardona et al. [2]. The drawbacks inherent to these methods require additional post-treatment steps and can result in an inability to identify the wear location and the requirement to embed traditional resistors.

For different applications in AM, various allotropes of carbon have been used. The main advantage of carbon is that it is low cost and, therefore, suitable for large-volume applications [51]. For the printing of GSS, material use should be more economical than in traditional methods. Therefore, using expensive silver-based material, such as that employed by Dardona et al. [2] or Shen et al. [52], is not desirable. Carbon-based material has advantages over metal-based material, including ease of printing, thermal annealing and longer shelf life (years) [53].

2.6 3D Printed Strain Sensors

It is important to collect information about strain and the stresses associated with structural components to monitor their health and performance [54–56]. Various types of strain gauges have been developed with different characteristics for different applications, such

as assessing postures in textiles [57, 58], measuring elbow flexing [59], contact detection and measuring bending in soft actuators [60, 61].

Mainly, strain gauges are developed using conductive material encapsulated within the structural base material, which will deform under strain. The amount of deformation can be gauged using either resistance or capacitance measurements. The sensor's capacitance will change in response to the change in layer thickness based on the applied load [62]. A multicore-shell fibre printing-based wearable strain sensor, which depends on capacitance measurement, was developed by Frutiger et al. [63]. The capacitance value increases because of the reduction of internal layer distance in this sensor when strain is applied. Conversely, strain gauges that depend on resistance measure the resistance changes in response to the strain-induced geometry changes [64]. In this application of GSS, a design consideration is that the slurry will change the dielectric constants; therefore, resistance-based methods are more applicable.

Different 3D printing techniques have been used to develop strain gauges. Nag et al. [65] developed a 3D printed mould-based method to produce a strain sensor for low-force applications. In this mould-based method, a graphite powder cast was used to create strain sensor traces. The metallic paste extrusion 3D printing method and viscoelastic ink printing were also used to print the strain sensors [60, 66]. Michael et al. [54] used FDM-based printing to determine the relationship between resistance and strain for the Acrylonitrile Butadiene Styrene (ABS), which was filled with carbon black.

Since GSS operate in various parts of the world with significant temperature differences, research has focused on developing a temperature-compensated 3D printed strain sensor. An FBG technique was used in a different type of sensor development because of its advantages, including its smaller size, lower cost, simpler structure and lack of interference from electromagnetic waves [67]. A temperature-compensated strain gauge using this technology was developed by Tanaka et al. [68] using two fibre sensors, one of which measured temperature and the other, strain. A four-wave mixing-based high-resolution temperature-compensated strain sensor was developed by Ghosh et al. [69] and, in this method, two chirped FBGs were utilised, so that the effect of the second temperature FBG compensated for that of the first. In this developed sensor, one FBG was oriented in a

different direction to make it immune to the internal strain. The sensor, developed using a four-wave mixing method, has an operating temperature in the range of 25-100 ℃. A tunable FBG temperature-compensated strain sensor was developed by Yuan et al. [70] using a dual-FBG sensor in a poly (methyl methacrylate) single-mode microstructured polymer optical fibre.

A surface acoustic wave sensor, which was temperature compensated, was utilised as the basis for a passive wireless strain sensor [71]. Because of its temperature stability, quartz was used as the piezoelectric substrate. Gu et al. [72] used two cascading Sagnac interferometers to develop a temperature-compensated strain sensor. This method used maximum strain sensitivity and robustness for crosstalk and used solid hybrid photonic crystal fibre, including stress-induced birefringence. The experimental results showed that this developed sensor exhibited high sensitivity for strain and low sensitivity for temperature.

In civil engineering, thick-film resistor-based strain sensors are used mainly because of their low manufacturing cost, sensitivity, long service life and stability. Unfortunately, these strain sensors are sensitive to temperature changes and to solve this problem, Wen et al. [73] developed a method to manufacture a thick-film strain sensor with lower temperature sensitivity. In this method, researchers used resistance-temperature curves with different materials to identify the effects of the temperature.

Due to their tunable properties, carbon nanomaterials are widely used in sensing applications. However, this material is affected by temperature changes and, to overcome these issues, Ramalingame et al. [74] proposed a new hybrid sensor, based on two materials with positive (graphene) and negative (multi-walled carbon nanotubes) temperature coefficients. Using this method, the new hybrid material becomes insensitive to temperature variations but retains its strain-sensing abilities.

To monitor the structural health of bridges, Zymelka et al. [75] developed a printed low-cost strain sensor array, which helps to identify and localise cracks and damages in the structure in different seasons throughout the year. A screen-printing method was used to manufacture the sensor, which required post-curing in a heated chamber. Additionally, the sensors were printed in arrays of 16 and entailed a full Wheatstone-bridge setup. Graphite-based material was used to manufacture the sensor, meaning that the development process

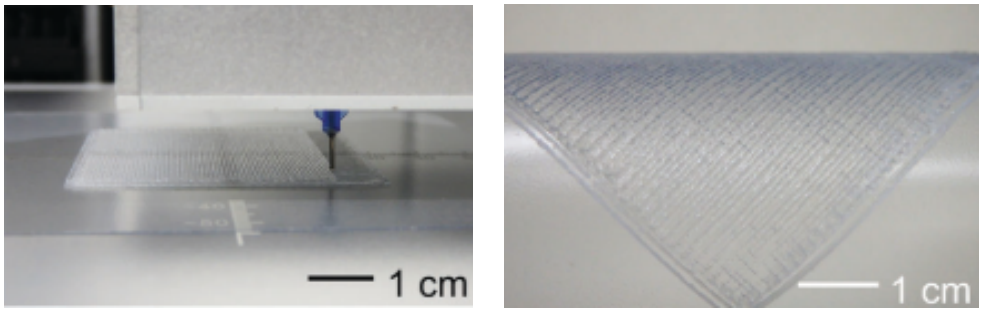

(a) (b)

FIGURE 2.3: Hydrogel-based sensors developed by Lei et al. [3]: a) A photo of the 3D printing process ; b) A photo of the printed flexible hydrogel film.

was low cost. Further, the size and shape of these arrays can be changed as required by each application.

Different materials have different thermal coefficients of resistance and, by using two materials, Daniel et al. [76] developed a temperature-compensated strain sensor. In this proposed method, they used platinum and titanium in a silicon substrate and arranged the sensors close to each other to subject them to the same temperature.

Different 3D printing methods have been used to manufacture strain sensors. The aerosol Jet® printing method was used to print strain sensors by Maiwald et al. [77]. A metal layer was printed on top of a polymer isolation layer, which was encapsulated to protect the sensor. This method helped to improve the density of the printed material and allowed it to achieve a high electrical conductivity. The aerosol printing method used by Thompson et al. [78] atomises a material solution into microscopic particles that are deposited onto the required surface. A water-based conductive polymer is used to print the strain gauge, which is then transferred onto a plastic base.

2.7 3D Printed Temperature Sensors

Embedded temperature sensors are widely used in various equipment. In Computer Numerical Control (CNC) machines, IoT-based temperature measuring systems have been embedded to monitor the manufacturing process [79]. Mohammad et al. [80] developed

fibre optic-based embedded temperature sensors for electrical coils to identify their operational integrity. To improve robustness and serviceability in turbine engine components, thermocouples have been directly fabricated into the components [81].

Lei et al. [3] developed a hydrogel-based temperature sensor in sub-millimetre resolution that is 3D printed and skin-like as shown in Fig. 2.3. This sensor works based on the difference in capacitance when hydrogel fibres are subjected to various temperatures. This sensor has a range of 25-50 ℃ and, additionally, the same sensor can be used to measure both touch and pressure. Uses for this type of sensor would be in personal healthcare applications, such as watches and wearable devices. Further, the same sensor can be used in soft robotics applications.

Micrometre-sized temperature sensors have been developed using 3D direct laser writing and these can be placed lithographically. Wickberg et al. [82] used this method to add temperature sensors to an electronic chip. During testing, in which the data recording frequency was 1 Hz, the sensor showed an accuracy of 0.5 K. This micrometre-sized sensor is valuable when quick, accurate local temperature measurements are required.

A 3D printed inverted-F antenna was developed using microfluidic and liquid metals to measure temperatures that depend on the resonant frequency [83]. Volume expansion occurs when the temperature and the antenna length change, altering the resonant frequency of the antenna. The resonant frequency decreases with the increased temperature and a near-linear relationship between these factors was observed [83]. A sensitivity of 2.54 MHz/℃ was evident during the simulated experiments. Another microfluidic and liquid metal-based wireless passive temperature sensor was developed by Traille et al. [84]. In this proposed method, several antennas are altered dynamically using liquid metal in a linear relationship along with the temperature. In the sensor, there are gaps filled by liquid metal and short circuits with temperature expansion, resulting in a change in the radar cross-section. The developed sensor is tunable to at least 20 K and has a resolution of 4 K.

A resistance-based temperature and humidity sensor was developed using the inkjet printing of silver nanoparticles by Courbat et al. [85]. Printed silver structures in the sensor are affected by the temperature, changing the humidity and electrical properties. The

tested temperature range of this printed sensor is -20-60 ℃ and a near-linear relationship between the resistance and the temperature was observed [85]. During the experiments, it was possible to observe a Temperature Coefficient of Resistance (TCR) of 0.0011 $℃^{-1}$. The humidity measurement depends on the capacitance change of the traces and was observed in an exponential relationship to the humidity level.

Temperature sensors have been developed from latex and exfoliated graphite-conductive paint to measure the temperature on a surface area [86]. A stencil was used and the paint was sprayed on to it in multiple layers. During the experiments in the temperature range of 20-60 ℃, a TCR of between -0.75×10^{-1} $℃^{-1}$ and -0.97×10^{-1} $℃^{-1}$ was observed.

Harada et al. [87] proposed using printable nanocomposite ink to print temperature sensors and strain sensors. These sensors were printed on a flexible substrate and were shaped like the whiskers of animals, mimicking the function of detecting obstacles and measuring temperature. This sensor was tested at between 25.8-53.2 ℃ and a sensitivity of 0.63% $℃^{-1}$ was evident. Further, mechanical and electrical reliabilities were characterised to ascertain whether the bending of the sensor had any effect. These sensors are used in robotics and artificial skins.

2.8 3D Printed Vibration Sensors

Monitoring vibrations is important in industrial applications. FBG sensors have been widely used to monitor vibrations [88, 89]. There are two different methods for developing FBG vibration sensors: including the FBG sensor inside the elastic material [90] and pasting the FBG sensor on the surface [91]. A miniaturised FBG vibration sensor was theoretically analysed by Wei et al. [92], and the simulation identified its structural parameters. The simulated sensor had a mass of 5 g and dimensions of 27 mm x 11 mm x 22 mm. The experimental results showed a range of 0-800 Hz and a sensitivity of 12 pm/g (picometre per gram), making it ideal for mid-high frequency range mechanical vibrations. A 3D printed optic vibration sensor, based on modulating light intensity using a blade attached to a flexible layer, was developed by Igrec et al. [93]. The sensor showed a linear relationship between bandwidths from 10-150 Hz.

Sinar et al. [94] developed a flexible piezoelectric vibration sensor, the flexibility of which is based on interdigitated electrodes printed on top of a paper, coated with a polymer. This sensor measures the impact force and prints using inkjet printing. During the experiments, an impact force of 6.3 N was applied at a frequency of 1-2.37 Hz and created up to 541 mV_{p-p}. Further, low-amplitude vibrations within the range of 50-2.5 kHz created an output from 25 mV_{p-p} to 452 mV_{p-p}.

The 3D printed smart eyeglasses developed by Zhang et al. [95] are embedded with a vibration sensor used to identify the signals from chewing various types of food to monitor dietary intake. The sensor integrated inside the 3D printed eyeglass frame is a commercial conventional sensor (Model 352C22, PCB Piezotronis, USA). The experimental results showed that the vibrations were immune to environmental noise.

Wu et al. [96] developed a skin-inspired tactile sensor designed for a prosthetic arm with giant magneto-impedance material inside, buffered by an air gap. The sensor showed a low detection limit of around 10 μN. This tactile sensor was integrated with an inductance-capacitance oscillation circuit that allowed the transduction of force to a digital frequency signal. This sensor can be used in smart prosthetics, enabling natural limbs to be replaced.

Godard et al. [97] developed a vibration energy harvester with an ability to generate around 1 mW from vibration using printed polymer. This sensor was printed with ten layers of piezoelectric polymer printed on a polymer substrate. The experiment results showed that the sensor could generate up to 0.97 mW at 33 Hz in an area of around 2.4 cm^2.

Yang et al. [98] proposed a permanent magnet energy-harvesting device based on electromagnetic energy. This sensor had resonant frequencies of 1,184 Hz, 938 Hz and 369 Hz. The observed power generation was 0.6 μW and 3.2 μW for an amplitude of 14 μm with a 0.4 mm gap for the first and second vibration modes.

Zhang et al. [99] developed a magnet array energy harvester that can produce a 0.25 W output in a submillimeter vibration amplitude. The same device was able to produce 263 mW of power when it was subjected to 65 Hz vibrations.

An inkjet 3D printed vibration energy microgenerator that can produce power in the mW range and has a resonant frequency of 250 Hz was developed by Kawa et al. [100]. The

device relies on the electromagnetic induction in a coil and a vibrating permanent magnet suspended on 3D printed micro springs. For this device, a pre-manufactured surface mount coil was used.

2.9 Partially-filled Pipe Flow Meters

To understand the condition of the GSS, it is important to measure the slurry flow rate in the spiral. The flow rate inside the pipe was observed to be partial. Therefore, the goal of this research is to develop a flow meter that can measure flow in partially filled pipes. In devices that have material flows, such as water desalination plants [101] and boilers [102], it is important to remotely measure the flow rate, especially when the devices operate in dangerous and remote locations. It is challenging to measure the flow rate in a partially filled pipe, so flow meters are generally calibrated by assuming that the pipe is full [103–105]. When this assumption becomes invalid, measurements become erroneous.

Flow meters can be categorised into two groups: non-intrusive flow meters, using externally mounted transducers without obstructing the flow; and intrusive flow meters, utilising inline transducers connected with the flow. Examples of non-intrusive flow meters include the optical flow meters, ultrasonic flow meters and electromagnetic flow meters, whereas paddle-wheel sensors and turbine flow meters are categorised as intrusive flow meters [106–109]. Different flow characteristics, such as pressure, conductivity, velocity and temperature determine the flow meter type that is most suitable for the specific application.

The electromagnetic principle has been used to develop industrial flow meters to measure partial flows in pipes using capacitance to determine the flow height. The induced current generated when the liquid flows through the magnetic field is used to determine the velocity of the flow. The TIDALFLUX 2000 flow meter [110] is an example of an electromagnetic partial flow meter. ABB Automation and Toshiba have also developed flow meters based on the same principle [111, 112]. The main issue with this type of flow meter is that the fluid running through the flow meter needs to be conductive [103, 110]; moreover, these flow meters are heavier and impractical to use as IoT sensors in every GSS.

The Doppler velocity method has been used to develop flow meters for partial filled pipes. In this setup, the ultrasonic wave is transmitted along with the flow and the reflection of the wave from the particles travelling in the liquid is used to measure the flow rate via the frequency difference. The MACE XCi device [113] is an example of this type of flow meter, in which it is necessary to have an intrusion type transducer, which is a disadvantage since it might clog the material deposition, requiring maintenance. Another partial flow meter developed based on the Doppler ultrasonic method is called the 2150 Area Velocity Flow Module and can measure the liquid level using a pressure transducer submerged under the liquid [114]. The FLO-DAR flow meter was developed based on Doppler radar velocity measurement and used to measure partial flow in open channels [115]. Additionally, LaserFlow is a subsurface laser Doppler flowmeter [116]. A summary of different partial flow measurement techniques and their limitations is provided in Table 2.1 [9].

Different liquid properties, such as buoyancy, electrical permittivity, pressure at a given depth and surface reflection of light or sound, have been used to measure liquid height. These properties have been utilised in different level sensors, including capacitive probes, displacers, floats and pressure sensors. These level sensors can be separated into two categories: the contact type and the non-contact type. Non-contact sensors normally have a longer life span because there is no chemical or physical reaction with the liquid [117].

Ultrasonic sensors are one of the common non-contact flow height measurement methods. The reason for this is that these sensors are easy to install, readily available and contactless. However, this method is affected by debris and air temperature fluctuations, floating foam and ripples [118]. Ultrasonic sensors mounted inside pipes that are vertically submerged in open water streams have been used to measure water levels [119]. Additionally, surface reflection-based methods use laser triangulation to measure the liquid height [120]. Radar-based level sensing can also be used to measure liquid height [121]. An acoustic sensor connected to a small diameter pipe is immersed in the liquid and used to measure height [122]. In this method, by analysing the frequency of the stationary waves created between the liquid level and the top of the pipe, the liquid level can be measured.

Image sensors have been used to measure liquid levels [123]. Water level measurement using edge detection was developed by Y. Jaehyoung et al. [124]. However, one limitation of this

sensing modality is that measurement accuracy might be affected by the environment's lighting.

The primary requirement for measuring slurry height is that the measurement method should be contactless. Capacitance has been used as a non-contact method for measuring liquid levels [125, 126]. A capacitance-based level sensing method proposed by Bera et al. [127] can be used to measure both non-conductive and conductive liquid levels in a non-metallic or metallic container. Capacitance-based level sensors for tanks have been used to measure liquid [128]. The advantage of this method is that it can be used without calibration.

In some cases, measuring a particular parameter using a single sensor is not enough to provide the required level of robustness or accuracy. One solution for this problem is to use sensor fusion, which employs multiple sensors to provide a more accurate and reliable estimate than would be possible with a single sensor [129, 130]. The sensor fusion approach has been used to combine information from multiple sensors to undertake remote health assessment/monitoring and fall identification [131]. The same approach has been applied to measure the accurate flow rate in a Venturi channel, combining three ultrasonic level sensors as well as other sensors [132].

Table 2.1: Comparative summary of partial flow measurement methods [9].

Technology	Examples	Accuracy (Error)	Limitations
Electromagnetic	TIDALFLUX 2000 [110] Toshiba LF502 [112] ABB FXP4000 [111]	1% full scale [110] 2% full scale [112] 3-5% of rate [111]	Only work with conductive liquids, Does not support small pipe diameters (70-100mm) required (⌀189mm [110], 150mm [112] and 212mm [111]), Heavy (40kg [110], 8kg [112] and 29kg [111])
Velocity (Doppler ultrasonic), Depth (Ultrasonic)	MACE XCi [113]	0.2-1% full scale	Heavy (5kg), Insertion type transducer will clog
Velocity (Doppler ultrasonic), Depth (Submerged pressure transducer)	Teledyne ISCO 2150 [114]	±2% of reading	Submerged transducer will clog
Velocity (Doppler radar), Depth (Ultrasonic)	FLO-DAR AV Sensor [115]	±5% of reading	Heavy (4.8kg), Only works for open channel
Velocity (Doppler laser), Depth (Ultrasonic)	LaserFlow [116]	±0.5% of reading	Heavy (8.7kg), Only works for open channel
Using U-shaped communication pipe [133]	No commercial product	2% of reading	The 2mm communication pipe will clog

2.10 Slicing for 3D Printing and Printability Analysis

GSS are helical-shaped objects and the printer under development can print radially around a central column. Conventional slicing occurs horizontally, which is not applicable for this bespoke printer. Therefore, research was conducted to develop a slicing algorithm for printing GSS with the bespoke printer.

Generally, there are two types of widely used slicing methods in AM: direct slicing and Standard Triangulation Language (STL) slicing. Different CAD software packages have a variety of data formats. The main advantage of direct slicing is that since it uses the original CAD model, it avoids any approximation that can affect the robustness [134]. A direct slicing method was suggested by Cao et al. [135], which slices solid models in AutoCAD. Another direct slicing method was developed by Chang [136] to slice models from the PowerSHAPE CAD application. The disadvantage of these direct slicing methods is that they can only be used with their specific CAD software or specific machines, so that it is not possible to guarantee its compatibility with multiple CAD software [137]. Hence, STL-based slicing is widely used in AM.

The first step in STL-based slicing is to use a CAD program to create a 3D model of the object and then export it to an STL file. Unlike direct slicing, in which slicing occurs in various CAD applications using their own data formats, in STL-based slicing, different CAD applications export models to a common STL format and a special program called a slicer slices the model. In the STL files, the surface of the object is approximated with small triangular facets, which is widely known as tessellation. The STL file format has been accepted as the de facto standard in the AM industry, mainly because the process is robust and simple. STL-based slicing makes slicing and AM processes independent from the CAD software. Therefore, STL files have been used in different 3D printing processes, including Selective Laser Sintering (SLS), Stereolithography Apparatus (SLA), Laminated Object Manufacturing (LOM) and FDM [138]. In STL-based slicing, the file is sliced, layer by layer; in general, the slicing intersects the STL file on horizontal planes and each plane provides the piecewise linear contours of a slice. Then, generated contours are filled with an appropriate infill and, as the last step, toolpaths are calculated to generate the printer machine instructions [139].

Different types of slicing methods have been used for slicing STL files. The uniform slicing method creates layers with a consistent thickness, whereas adaptive slicing will create slices of varying layer thickness [139, 140]. Kirschman et al. [141] developed a simple uniform parallel slicing method that will intersect triangles in the Z plane and connect segments of lines into closed polygons from the top to the bottom of each slice [140]. Conversely, adaptive slicing creates slices with varying spacing that can be programmatically changed based on parameters such as capacity and geometry. The main advantage of adaptive slicing is the build time reduction and the improved surface finish. Yang et al. [142] used this method to slice a point cloud. The proposed method was based on the moving of least squares surfaces. A combination of direct and adaptive slicing is called hybrid slicing [143]. The aforementioned methods rely on the plane-triangle intersection to generate contour geometries. However, these methods can cause issues such as singularity-case problems, including isolated points and dangling edges [144].

In order to develop a slicer for a robot, it is important to consider how the robot can move. Limitations in the movements that a robot can make will effect its ability to print, or printability [26]. A robotic manipulator's ability to perform different tasks depends on the location in physical space, the kinematic model and the environmental restrictions. To achieve the desired performance in a particular task, manipulability and reachability information can be used to design the process [145]. A capability map represents the workspace, showing the ability to move in the surrounding space of the robot manipulator. These capability maps can be used to identify the places that can easily be reached by the robot manipulator. Hence, objects can be moved to a place where more versatile manipulability is available or the manipulator can be reconfigured or repositioned to enable a higher degree of manipulation [146]. For assembly tasks that use planar robot arms and adaptively modify planar 3D printing, dexterity measures have been applied by researchers [147, 148].

The previously mentioned slicing methods are unsuitable for printing GSS since the printing operation occurs around a central column, oriented using robot arms. Gang et al. [149] developed a slicing method that is non-planar for stationery printing, which differs from normal horizontal plane slicing [150–152]. However, this non-planar slicing algorithm

was developed for smaller objects. Additionally, when printing the GSS, printing happens in a non-stationary manner around a rotating central column. A curved layer LOM method, which increases the speed and reduces the waste, was developed by Klosterman et al. [153]. However, this is a specific manufacturing method and is not suitable for other AM processes. A parametric, surface-based path generation method was developed by Chakraborty et al. [154], adapting curved layer accumulation for thin AM components.

2.11 Path Planning for 3D Printing

In this research, during the print simulation, it was observed that there were some print failures. Therefore, the research focused on developing an optimal print path planning algorithm.

The dexterity of a robot arm, which enables it to move easily, is referred to as manipulability [155]. A robot arm can easily perform more actions if it has greater dexterity, which enables added assembly or printing, resulting in better use of the robotic manipulator. As mentioned, it is desirable to the print embedded sensors inline while printing the GSS. Therefore, it is advantageous to retain high levels of manipulability throughout the print. The manipulability measure can be used to optimise the plans for 3D printing.

To improve the effectiveness of robots, the manipulability measure has been used by numerous researchers. Chiacchio et al. [156] showed that dynamic manipulability could be used to improve the results of redundant manipulators. For mobile manipulator path planning, Nagatani et al. [157] proposed a method to maintain the manipulability threshold. Manipulability area plots have been used as a tool by researchers to determine areas that have high levels of manipulability [157]. To assist humans in conducting operations remotely, Amir et al. [158] proposed a method that uses a cost function, considering task-oriented velocity manipulability. A cost function that includes a measure of distance from the limits of the joint and task-oriented manipulability has been used to determine the optimal grasping pose of the needle for suturing during surgery [159]. Tommaso et al. [160] utilised the optimal manipulability-based path planning for cutting in nuclear power plant

equipment decommissioning. In their research, to maximise the robot's manipulability, they used a multi-objective optimisation method while minimising the travel distance.

In robotics, cost-based path planning has had various applications, such as in underwater autonomous vehicles [161]. This method was shown to enable the underwater robot to avoid obstacles and to utilise current data to obtain greater speeds while minimising energy expenditure. Lin et al. [162] used both library-based planners and discrete planners for humanoid navigation in uneven terrain. In this case, a graph search method, based on cost, was used to determine the path for the torso pose.

For humanoid robots, quality distribution maps of the workspace have been used to determine the most suitable grasp depending on the current state [163]. The same method is useful for redundant manipulators, considering joint limits and self-distance. Probabilistic Road Maps (PRM) algorithms have been used to plan collision-free paths for robots. Manipulability has also been used as a sampling factor to generate PRM, taking fewer samples when manipulability is high and more samples where manipulability is low [164]. Menasri et al. [165] proposed a genetic, algorithm-based path planning method for redundant manipulators by maximising the manipulability. By utilising mechanical properties and avoiding singularities, this manipulability-based optimisation allowed the robot system to move with less effort.

2.12 Optimal Sensor Placement

This thesis focuses on developing various sensors that can be placed in the GSS. Additionally, determining a method for placing sensors in the optimal location is important. Developing methods to identify damage to various structures in mechanical, civil and aerospace applications is called Structural Health Monitoring (SHM) [166–168]. To ensure sustainability and serviceability, SHM plays a vital role in detecting damage in complex and large structures [166]. Therefore, it helps to identify the status of the structure so that information can be used to undertake planned maintenance without causing disruptions to the operations [169]. GSS operate continuously in various locations around the world

and determining maintenance issues early will facilitate this continuous operation. A critical aspect of SHM is the Optimal Sensor Placement (OSP), which directly influences the quality of the collected data [166]. Unnecessary closure for maintenance might be caused by a high risk of a false-positive, incurring operational costs without OSP [169]. Without OSP, arbitrary sensor placement might result in false damage detection [170]. More sensors placed in the structure will provide more data. However, this will cause the total cost of the set of sensors to increase and will inhibit data acquisition systems that limit using a large number of sensors [171]. Without compromising the quality of the data, OSP will reduce the cost of SHM systems [169]. Moreover, OSP can be used to identify the minimum number of sensors that will provide the required amount of information [171].

The optimal sensor array layout for SHM was developed by Robert et al. [172] and includes Finite Element Analysis (FEA) in the face of uncertainty. Robert et al. [172] included FEA, reliability-based optimisation and damage-detection concepts. An FEA-based sensor placement was used by Ting et al. [173] to place sensors in the Dalian World Trade Building using a simplified multi Degrees of Freedom (DOF) system since the DOF were high. For Large Space Structures (LSS) sensor placement, Kammer [174] used collected data from the sensors to validate LSS Finite Element Model (FEM). The modified FEM described the real structure more accurately. A methodology to identify the most relevant DOF monitored by sensors was proposed by Stephan [175]. This method depends on selecting the sensor set that will maximise the Fisher information matrix norm for a large FEA.

Using information gain for sensor placement has been investigated before. Information Entropy (IE) was used by Costas et al. [176] to measure the performance of the sensor setup. They have framed this as an optimisation problem that includes discrete-valued variables. This is solved by using a sequential sensor placement algorithm to identify the optimal sensor configuration. Optimal sensor configurations have been selected by choosing the sensor configuration that minimises the IE [177]. Paul et al. [178] characterised a multimodal sensor setup and used multi-location sensor placement, adopting information theory for the exploration and mapping of bridge structures. Meo et al. [179] employed an OSP method using energetic approaches and covariance matrix coefficients to maximise the information.

Different types of algorithms have been developed for sensor placement. These sensor placement algorithms that address problems such as observability, reliability, diagnosability and detectability are NP-complete and computationally expensive. Therefore, optimisation methods based on constraints have been used [171]. Traditional gradient-based optimisation methods have difficulty in determining the global minimum because of the multiple local optimums and, therefore, biological optimisation methods have been applied in recent years [171]. Gao et al. [180] used a biologically inspired method called Genetic Algorithms for OSP to determine the number of sensors as well as the damage misdetection rate. Ant colony and particle swarm optimisation is another similar method used for OSP [181, 182]. A further systematic and computationally efficient algorithm is sequential sensor placement, which is more efficient at determining sensor configurations [169]. However, this method does not guarantee the most optimal sensor configurations [183]. In the sequential sensor placement method, a given number of sensors are sequentially placed one at a time, which results in the greatest reduction of the objective function [171]. For structural damage identification, a damage-detection sensor placement method was developed by Lin et al. [184] considering the type of sensor, the number of sensors and the spatial locations.

Hwang et al. [185] developed a sensor placement method for 3D printed prosthetic hands that use tactile objects covered with ink to identify the areas in which sensors should be placed. In this experimental method, the objects were touched with ink-covered, gloved hands and the ink strains were identified by image processing and used to recommend sensor placement.

2.13 Conclusion

3D printing large scale industrial equipment and monitoring operating conditions are the main objectives of this research and development project. Using traditional sensors in cavities in 3D printed objects can compromise the structural integrity due to the different material properties. Generally, the 3D printed sensors found in the literature use printing techniques that require post-processing steps like sintering and require expensive material like silver. Table 2.2 shows a summary of the limitations if currently available sensors

were employed to measure the required parameters in the 3D printed GSS. Therefore, further research is needed to develop low-cost complementary sensors that can be easily 3D printed inline without post-processing, and that can be used in large scale manufacturing to address specific application requirements. Compared to existing 3D printers that have been reviewed, the bespoke 3D printer that is under development is novel in that it needs to print helical objects in vertical layer additions, which poses new challenges in slicing and robot path planning. This presents the need for an integrated radial slicer and robot path planning method. As well as a way to incorporate and optimise the placement of 3D printed sensors within 3D printed objects. This is a new aspect of research since it introduces new challenges and requirements compared to traditional sensor placement methodologies, including the need to simultaneously consider structural integrity, information gain, and the design and printability of the sensors.

Table 2.2: Comparative summary of sensor types and their limitations if employed for 3D printed GSS.

Sensor	Technologies	Limitations relating to printed GSS
Wear	Acoustic emission [43, 44], Micro-mechanical resonant vibrations [45], Electrical-based methods [46–49], Printed silver traces [2, 50]	For tools and piston rings only [43, 44], Require silicon structure [45], Require conductive layers and vacuum deposition [46, 47], Developed for cutting tools [48], Require connected resistors and post treatment [2, 50], Work with coated geometries [49]
Strain	Capacitance-based [63], Using 3D printed mould [65], Ink printing [60, 66], FDM-based [54], FBG techniques [68–70], Acoustic wave [71, 72], Thick-film resistor-based [73], Screen-printing [75], Aerosol jet printing [77, 78]	Flexible material and suitable for wearable [63], Requires creation of a mould [65], Used different type of printing methods [60, 66, 75, 77, 78], Used ABS material [54], Require placement of external sensors [68–72], For civil engineering structures [73]
Temperature	Fibre optic-based [80], Hydrogel-based [3], Direct laser writing [82], Microfluidic and liquid metals [83, 84], Inkjet printing [85], Conductive paint [86], Nanocomposite ink [87]	Require placement of external sensors [80], Require different type of material [3, 83, 84, 87], Suitable for electronic chips [82], Uses different type of printing [85], Paint can be removed from abrasion [86]
Vibration	FBG or optical sensors [90, 92, 93], Inkjet printing [94, 100], Magneto-impedance material [96], Piezoelectric polymer [97], Magnet-based energy harvesters [98, 99]	Require placement of external sensors [90, 92, 93, 98, 99], Uses different type of printing methods [94, 100], Require different type of material [96, 97]

Chapter 3

Direct-Write Fabrication of Wear Sensor

The in-situ measurement of wear in 3D-printed components has many advantages, such as the enabling of informed decisions, including a) the identification of equipment failure and planned maintenance and b) the changing of various feeds and speeds to achieve an optimal production rate [186]. Regarding GSS, the monitoring of wear in situ in real-time and remotely is important. Monitoring both the location and the extent of wear makes it possible to improve the future 3D printing of GSS by optimising printing properties or materials.

3.1 Methodology

3.1.1 Design of the Sensor

The design of the conductive traces is shown in Fig. 3.1a and is printed using carbon-based proto-pasta conductive PLA material [187]. The selected dimensions for the traces are 20 x 40 x 2 mm. The dimensions are chosen based upon the number of traces necessary for the target resolution, the thickness and resistivity of the conductive material, and the need to embed the printed traces in a package that fits within the spiral profile.

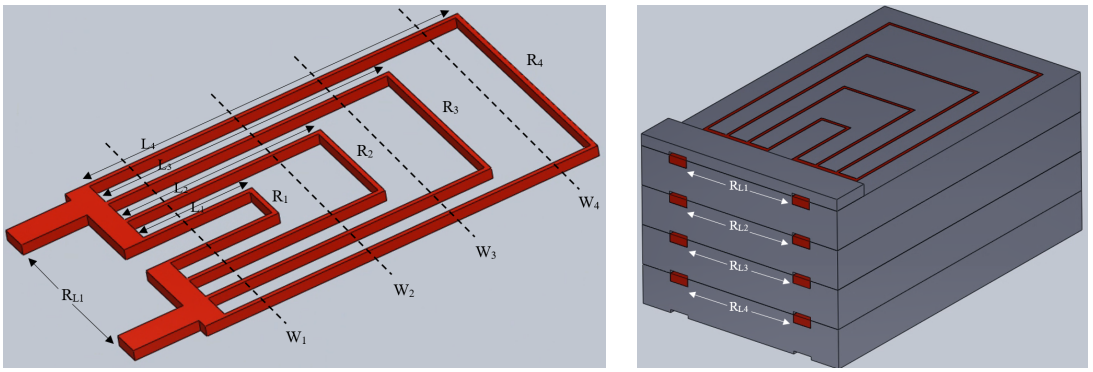

(a) (b)

FIGURE 3.1: Printed traces [4]: a) A single layer of traces; b) Multiple layers of traces embedded in the base material.

The required wear resolution is determined by the number of traces. The minimum and maximum number of traces for an optimum resolution depends on the nozzle dimensions and how accurate the printer is. The closer that the conductive traces can be printed without electrically connecting them, the higher the sensing resolution becomes. However, depending on the printer accuracy, in the real-world printing traces only a single layer apart may lead to them being electrically connected. Multiple conductive traces are printed vertically, as shown in Fig. 3.1b and those layers are separated using insulating PLA material. The number of layers can be adjusted according to the desired wear resolution. The resistance of each trace, R_X; the total individual resistance of each layer, R_{LX}; the length of each trace, L_X; and the different locations at which wear can occur are given by W_X where $X \in [1, 4]$. The resolution and coverage of the wear sensor can be configured to suit the application by increasing or decreasing the number of traces.

3.1.2 Measurement and Localisation of Wear

All the traces in one single layer are electrically parallel with the terminals, and (3.1) shows the total resistance of Layer 1. Similarly, the same equation, (3.1), is applied to each trace component in each layer.

$$\frac{1}{R_{L1}} = \frac{1}{R_1} + \frac{1}{R_2} + \frac{1}{R_3} + \frac{1}{R_4} \tag{3.1}$$

TABLE 3.1: Wear location and resistance in one layer [4].

Wear Line (W_X)	Total Resistance (R_{L1})	Wear Location (x)
W_1	∞	$x < L_1$
W_2	R_1	$L_1 < x < L_2$
W_3	$\frac{R_1 R_2}{R_1+R_2}$	$L_2 < x < L_3$
W_4	$\frac{R_1 R_2 R_3}{R_2 R_3+R_1 R_3+R_1 R_2}$	$L_3 < x < L_4$

The resistance of all four layers will be similar without any wear. Thus, we assume that the wear occurs along the line W_2 in the first layer and is only thick enough to cut Layer 1 without affecting the conductive traces in Layer 2. In this scenario, R_{L1} is equal to R_1. Since each trace has a known resistance, it is possible to predict that the location of the wear is greater than L_1 but less than L_2. In a scenario in which the wear occurs along the line W_3, the resistance of R_{L1} will be equal to the combined resistance of R_1 and R_2. Therefore, by measuring the resistance, it is possible to predict the location of the wear is greater than L_2 but less than L_3. Similarly, the location of the wear in each layer can be predicted by measuring the resistance. A summary of the wear location based on the resistance in one layer is shown in Table 3.1.

Each layer's resistance is measured independently. Hence, it is possible to ascertain the depth of the wear. Since the wear distance can be predicted using Table 3.1, the details of the wear profile can also be estimated.

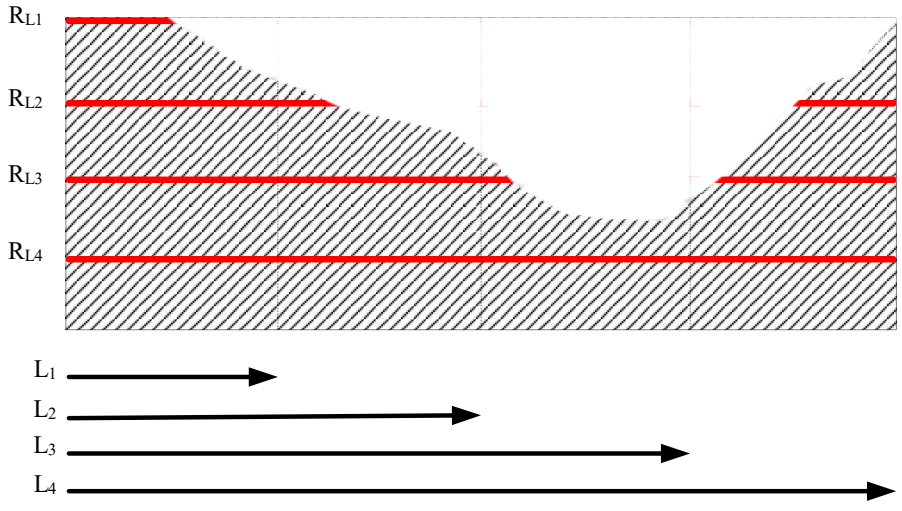

FIGURE 3.2: Cross-section of the sensor with an example wear profile [4].

A vertical cross-section of the sensor with an example wear profile is shown in Fig. 3.2. The possible resistance values for this specific wear profile and predicted wear location are shown in Table 3.2.

TABLE 3.2: Wear location according to the measured resistance in each layer [4].

Resistance (R_{LX})	Wear Location (x)
∞	$x < L_1$
R_1	$L_1 < x < L_2$
$\frac{R_1 R_2}{R_1+R_2}$	$L_2 < x < L_3$
$\frac{R_1 R_2 R_3}{R_1+R_2+R_3}$	$L_3 < x < L_4$
$\frac{R_1 R_2 R_3 R_4}{R_2 R_3 R_4+R_1 R_3 R_4+R_1 R_2 R_4}$	No Wear

3.2 Experimental Results

3.2.1 Printing the Sensor

There were multiple techniques to print the sensor using a extrusion printer and those are assembling separately printed components, pausing prints, printing using a multi-material printer, and embedding printed components into a print. Irrespective of the selected technique of printing, the functionality of the sensor is the same since the material, dimensions and the arrangement of the sensor is the same. Therefore, to reduce material waste and reduce print time, the sensor was printed and assembled separately. The reason for selecting this technique was to reduce the material waste from printing a purge tower (printed volume to clear the nozzle from previous material type) and to remove the requirement to pause the print to embed parts. The assembled wear sensor is shown in Fig. 3.3.

Twenty-five conductive tracers were printed, as shown in Fig. 3.4, to determine the variation of resistance across multiple conductive prints. According to the measurements taken, the standard deviation of the traces was 0.1005 kΩ, and the results are shown in Fig. 3.5. From these results, it can be concluded that the resistance is relatively consistent across multiple printed traces.

3.2.2 Resistance and Wear Location

As shown in column 2 of Table 3.1, the resistance values must be measured to determine the wear location. To simulate the wear, conductive traces were disconnected, as shown in Fig. 3.6, and the resistance values were measured. The results are summarised in Table 3.3 and the trend is depicted in Fig. 3.7. A very small crack across the traces might reduce the electrical conductivity, and thus more experiments are needed to identify the effects of cracks, as opposed to complete wear.

TABLE 3.3: Wear location and resistance in one layer [4].

Wear Line (W_X)	Total Resistance ($R_{L1}k\Omega$)	Wear Location (xmm)
No Wear	4.17	None
W_4	4.83	$25 < x < 33$
W_3	5.41	$17 < x < 25$
W_2	7.23	$9 < x < 17$
W_1	∞	$x < 9$

3.2.3 Wear Profiling

A summary of the test results conducted for various wear profiles and predicted and actual wear locations is provided in Table 3.4.

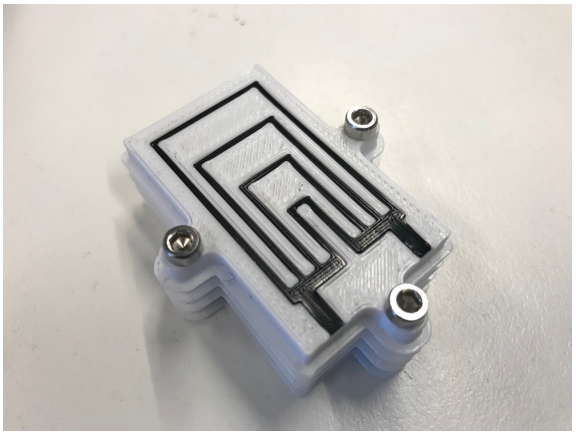

FIGURE 3.3: 3D printed and assembled wear sensor [4].

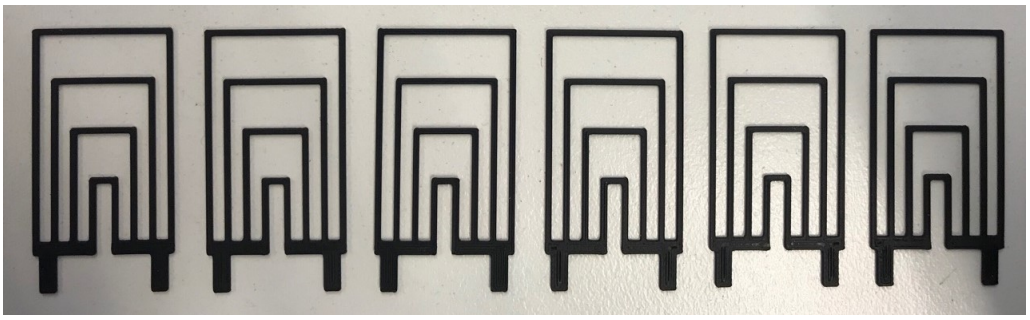

FIGURE 3.4: Multiple printed conductive traces [4].

The dashes in Table 3.4 indicate "no wear". There was no predicted or actual wear for Layer 4 and, therefore, it was excluded from the table. The various wear profiles that were tested are shown in Fig. 3.8. The location of the wear was predicted by comparing each layer's resistance values to Table 3.1 and choosing the closest location. The dash lines in Fig. 3.8 depict the length of the traces (L_X) that were measured from left to right and W_x

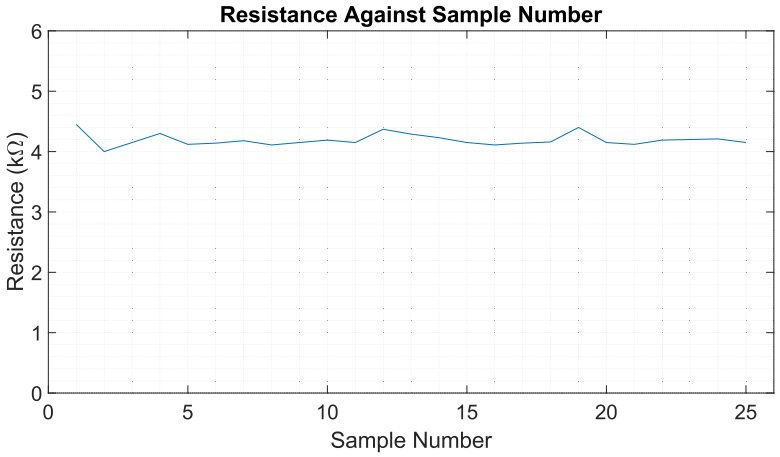

FIGURE 3.5: Total resistance against sample number [4].

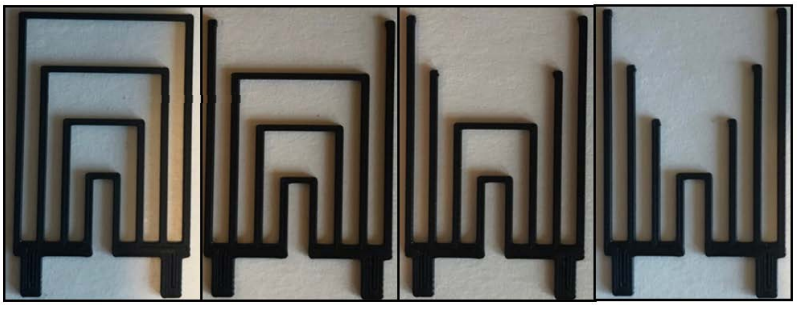

FIGURE 3.6: Samples prepared for the experiment relating resistance measurement to different wear lines [4].

reveals the wear line locations, as shown in Fig. 3.1a.

3.3 Discussion and Conclusions

This chapter presented a wear sensor that can be directly printed to a 3D printed object. Sensor was printed as multiple layers of conductive traces with carbon-based filament and resistance measurement used to determine the depth and the location of the wear. The proposed design enables the measurement of the distance to the location of the wear, relative to one axis and parallel to shown wear lines. Using these measurements, the wear profile can be determined relative to the datum axis. However, in the tested configuration, it is impossible to determine the wear profile from the opposing side. An arrangement with stacked sensors would be interesting to investigate. Rather than one datum axis, such a design contains two datum axes, facilitating the measurement of the wear location from

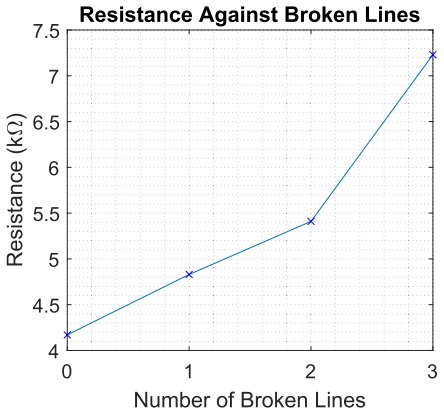

FIGURE 3.7: Resistance relative to broken wear lines [4].

TABLE 3.4: Predicted and actual wear locations according to the measured resistance in tested wear profiles [4].

Test	Resistance After Wear				Actual Wear Line			Predicted Wear Line		
	R_{L1}	R_{L2}	R_{L3}	R_{L4}	$Layer_1$	$Layer_2$	$Layer_3$	$Layer_1$	$Layer_2$	$Layer_3$
1	5.45	4.82	4.29	4.10	W_3	W_4	-	W_3	W_4	-
2	5.49	5.48	5.43	4.13	W_3	W_3	W_3	W_3	W_3	W_3
3	∞	∞	4.14	4.10	W_1	W_1	-	W_1	W_1	-
4	∞	∞	7.66	4.13	W_1	W_1	W_2	W_1	W_1	W_2
5	7.20	4.18	4.11	4.16	W_2	-	-	W_2	-	-
6	7.28	7.25	4.20	4.14	W_2	W_2	-	W_2	W_2	-

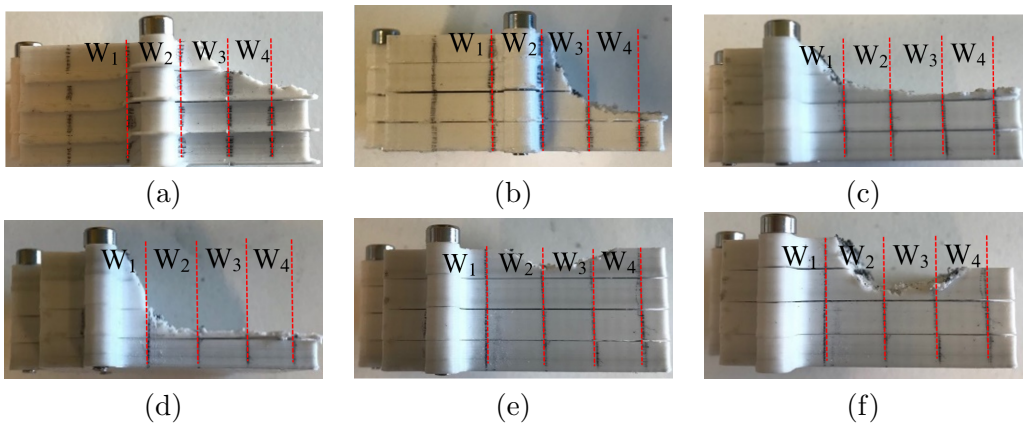

FIGURE 3.8: Wear profiles [4]: a) Test 1; b) Test 2; c) Test 3; d) Test 4; e) Test 5; f) Test 6.

either side. This new configuration would allow a complete 2D cross-sectional profile of the wear. The same configuration can be extended by stacking multiple sensors adjacent to each other, enabling a complete 3D map of the wear location.

Chapter 4

3D-Printed Strain Sensor with Temperature Compensation

For GSS, measuring strain has various advantages for several reasons. One is to monitor and confirm that the operators of the GSS follow the given guidelines and do not load the GSS unnecessarily. An excessive load might damage the GSS permanently by deforming it, which may result in it needing to be replaced. This replacement process costs both time and money. Integrating strain sensors to the GSS will help to identify these kinds of incidents and will allow for the alerting of operators to imminent issues, encouraging them to follow proper guidelines. Additionally, strain measurement will help in understanding the long-term creep of the GSS and predicting when replacement is necessary. The profile of the GSS determines the production output [22]. With time, the material will slowly deform (i.e., creep), and this change in the profile will affect the production output. It may be possible to redesign the GSS to reduce the observed creep behaviour in future by understanding this behaviour in the long term. It is imperative to develop a strain sensor that is temperature compensated because the GSS operates in locations where there are significant temperature variations throughout the year. This chapter presents the details of the developed strain sensor, which was printed using a carbon-based conductive material, mainly because of its corrosion resistance, low cost and widespread availability.

4.1 Methodology

4.1.1 Principle of Strain Gauges

Strain can be defined as the ratio between an initial length and an elongation of it resulting from an applied force. There are four types of strain: torsional, bending, shear and axial [188]. The gauge measures strain based on electrical resistance, which varies in proportion to the applied strain. The basic components of a strain gauge are shown in Fig. 4.1. Traditionally, strain gauges have wires or thin metallic foil in a grid pattern to maximise the amount of axial strain. 3D-printed conductive carbon-based traces have been used in this research to replace the wire or metallic foil. Since the traces are printed inside the base material, strain is transferred directly to the traces.

When the material is subjected to deformation, the material's resistance is given by Eq. (4.1), where the resistance is R, the resistivity is ρ, the length is l and the cross-sectional area is A. When the load is applied, it will increase the l and decrease the A, which will accelerate the resistance in the terminals A and B in Fig. 4.1. As shown in Eq. (4.2), the ratio of the fractional change in resistance, $\Delta R/R$, is proportional to the strain. The sensitivity of the gauge to the strain ε is called GF.

$$R = \rho l/A \tag{4.1}$$

$$\Delta R/R = GF \times \varepsilon \tag{4.2}$$

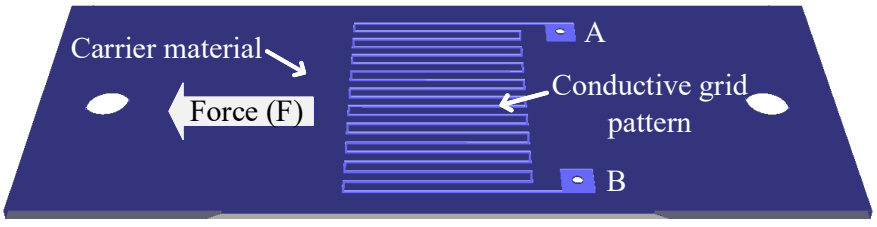

FIGURE 4.1: Components of a strain gauge [5].

4.1.2 Temperature Compensation

The Wheatstone bridge-based method has been used to measure minor changes in the resistance. The mechanism of the Wheatstone bridge can be explained as two voltage divider circuits arranged in parallel. One circuit contains R_1 and R_2 and the second circuit contains R_3 and R_4, as shown in Fig. 4.2a. Using the input voltage, V_E, the voltage of the bridge, V_0, can be calculated as shown in Eq. (4.3).

$$V_0 = \left[\frac{R_3}{R_3 + R_4} - \frac{R_2}{R_1 + R_2}\right] \cdot V_E \tag{4.3}$$

Different types of available arrangements for strain sensors are full-bridge, half-bridge and quarter-bridge. In the quarter-bridge setup, which has one single strain gauge, R_4 acts as the active strain gauge that measures bending strain or axial strain. However, this arrangement does not compensate for the temperature. There are two configurations for the half-bridge. For the bending strain measurement, the arrangement shown in Fig. 4.2b has been chosen. The active strain gauge in this arrangement is R_4 and measures tensile strain ($+\varepsilon$), while a compressive strain is measured by ($-\varepsilon$) [189]. For the temperature-compensated strain gauge in this chapter, half-bridge and quarter-bridge configurations were contrasted to understand the effectiveness of temperature compensation.

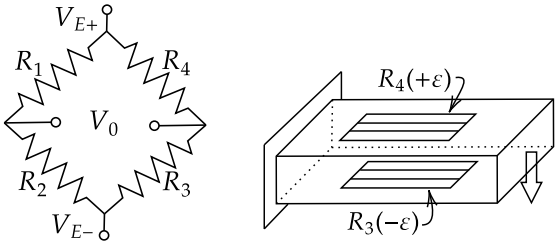

FIGURE 4.2: Proposed Wheatstone bridge configurations [6]: a) Full Wheatstone bridge; b) Half-bridge setup.

4.1.3 Sensor Calibration

The calibration of the strain gauges can be performed by applying a known load to the gauge and measuring the resistance. When the strain gauges are mounted to the equipment, the best calibration method is to load the equipment with a known load distribution and measure the output [190]. A tensile-testing machine that can apply a known strain value can be used to calibrate the printed strain gauges. By measuring the electrical resistance with that known strain, the gauge factor can be calculated. After determining the gauge factor, the sensor is considered calibrated, and future measurements of the resistance will be used to determine the strain.

4.2 Experimental Setup and Results

An Instron E10000 tensile-testing machine was used to test the 3D printed pure material as well as the printed strain gauge. This machine has up to ±10 kN dynamic load capacity and ±7 kN static capacity [191]. Standard dog bone-shaped test specimens were 3D-printed in different material and with various raster angles to identify the material's properties. The 3D-printed strain gauges were then tensile tested to investigate the relationship between strain and resistance. Since it is difficult to create a temperature-controlled area around the Instron machine, a new testing rig was developed by the author to overcome this limitation. This new rig is shown in Fig. 4.3b.

4.2.1 Materials and Printing Process

A proto-pasta conductive PLA has been chosen for conductive traces. This is a composite material based on conductive carbon black and Natureworks 4043D PLA. The resistivity of this material is rated at 15 Ω.cm before printing. After printing, along the X–Y plane, it is rated at 30 Ω.cm and, on the Z-axis, at 115 Ω.cm. First, samples were printed with a thermoplastic polyurethane base material. However, these samples had low layer adhesion, and traces become detached. Therefore, to improve the adhesion between conductive traces

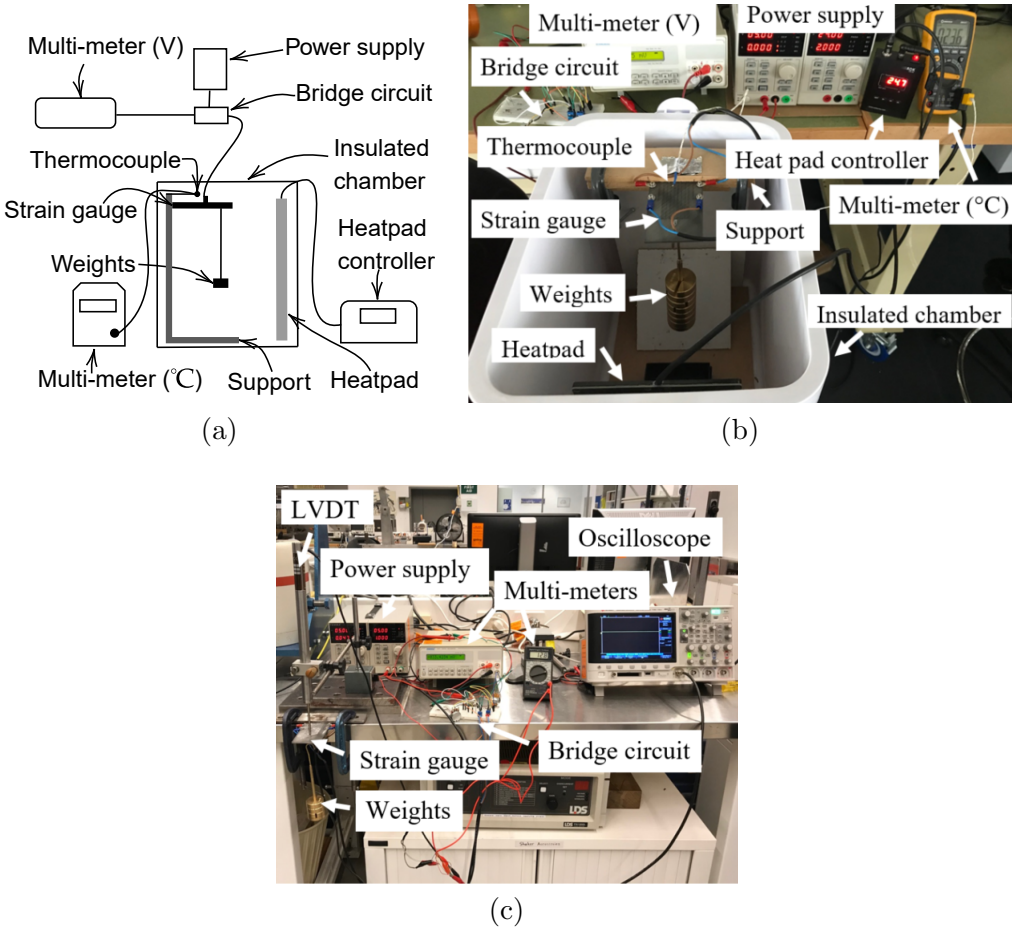

FIGURE 4.3: Experimental setups [6]: a) Components of the temperature testing rig; b) Temperature testing rig setup; c) Displacement testing rig setup.

and the base, non-conductive PLA was used as a comparable material with similar printing parameters.

To print the specimens, a Prusa i3 MK3 printer was used with the Multi-Material Unit 2.0 [192]. This is a popular and open source FDM printer that can print up to five filaments, having a build volume of 250 x 220 x 215 mm, print speed up to 60 mm/s and resolution of 0.02 mm. This printer was used because of the variety of low-cost material available. Table 4.1 shows the parameters for the printing specimens.

Specimens for tensile testing were printed with a layer height of 0.15 mm and a 100% infill. Two types of dog bone specimens were printed for each material with 45-degree raster angles and 100% infill. All printed strands were oriented parallel to the tensile load with 100% infill. The 45-degree raster specimen was offset from the tensile load by 45

TABLE 4.1: Print parameters for the sensors used in the experiment [6].

Print Parameter	**Value**
Nozzle diameter	0.4 mm
Bed temperature	65 °C
Nozzle temperature for PLA	210 °C
Nozzle temperature for conductive PLA	240 °C
Printing speed PLA	60 mm/s
Printing speed conductive PLA	25 mm/s
Purge volume	700 mm^3

degrees. In this sample, each alternating layer was oriented by -45 degrees. For the strain gauge tested for tensile strain, conductive traces were printed with a single strand in each layer, and the base was printed with a 45-degree raster angle.

To test the standard tensile properties of the material, the printed dog bone dimensions adhered to the ASTM D638 standard, which dictates the tensile-testing method for plastics [193]. Fig. 4.5a shows these printed dog bones. To improve the adhesion between traces and the base PLA, printing speed was reduced. The strain gauge printed using this method is shown in Fig. 4.5b. The dimensions of the specimens are shown in Table 4.2.

For the temperature-compensated strain gauge, the different sensors were printed, two of which were embedded inside the PLA base. A 3D model of the sensor is shown in Fig. 4.4a. The dimensions of the sensor were 150 mm x 60 mm x 3 mm for length, width and thickness, respectively. The trace width of the sensor was 1 mm. In this design, the half-bridge configuration was used with two sensors, as shown in Fig. 4.2b and Fig. 4.4a, which provide a closer view of the printed sensor. The same conductive filament and based material used to print the tensile strain gauge were used to print the temperature-compensated strain.

4.2.2 Standard ASTM Testing

To understand the difference between non-conductive and conductive PLA material, tensile testing of the 100% infill was conducted. These three specimens were tested with an elongation rate of 0.5 mm/min in the Instron E10000 tensile-testing machine until they

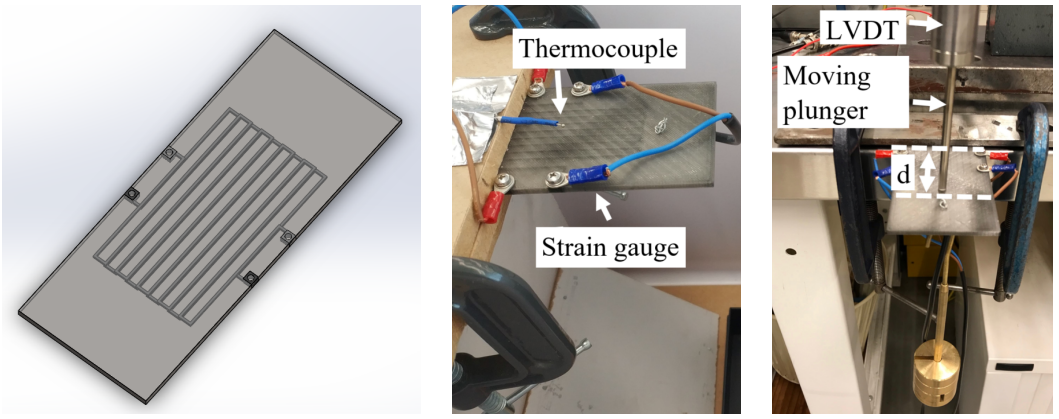

(a) (b) (c)

FIGURE 4.4: Sensor setups [6]: a) Temperature-compensated strain sensor design; b) Close-up view of the sensor; c) Close-up view of the arrangement of the LVDT sensor.

TABLE 4.2: Strain gauge dimensions [6].

Dimension	**Value (mm)**
PLA base depth	0.8
Trace depth	0.4
Trace width	0.4
Individual trace length	40
Total trace length	869
Trace offset distance	3
Length of strain surface	90
Width of strain surface	69.5
Tab thickness	2.4

broke. The 45-degree raster angle specimens were also tested using the same method to understand the raster angle's effects.

The results of the dog bone testing are shown in Fig. 4.6a. From the testing, it was observed that PLA has a higher ultimate tensile strength than conductive PLA. Conductive PLA has an ultimate tensile strength of 30.45 MPa, while PLA has a tensile strength of 53.69 MPa for 100% infill specimens. Unlike the 100% infill dog bones, the 45-degree raster angle dog bones showed lower strength with a reduction of 15.6% (4.75 MPa) for conductive PLA, while normal PLA showed a reduction of 19.11% (10.07 MPa).

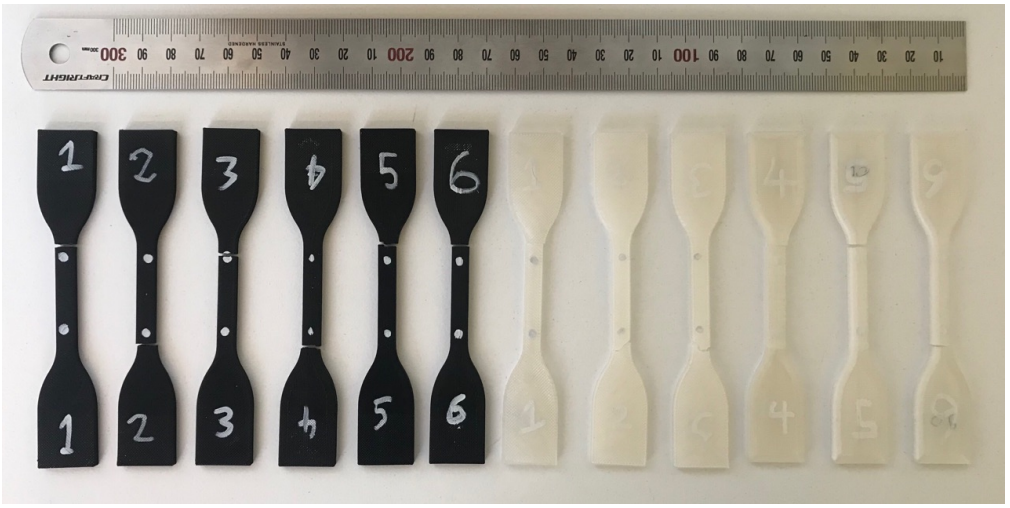

(a)

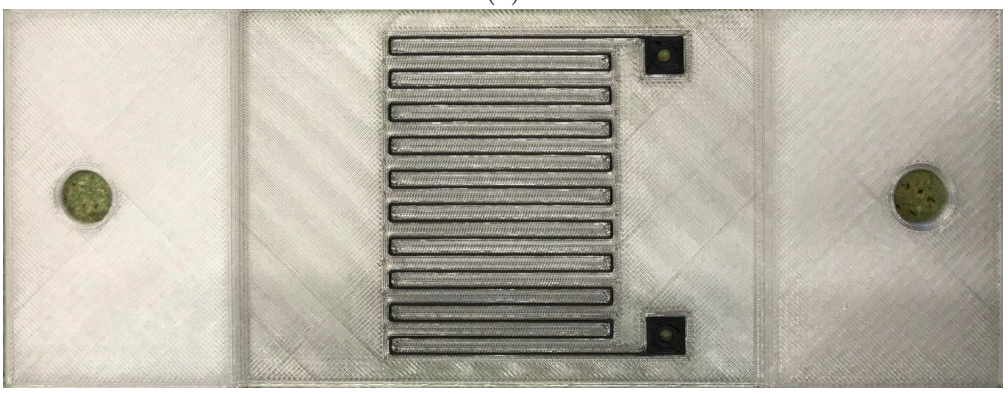

(b)

FIGURE 4.5: a) ASTM D638 standard dog bones [6]. b) 3D printed strain gauge [6].

4.2.3 Tensile Testing

Initially, destructive tensile tests were conducted to understand the load required to plastically deform the specimen. The strain gauges were subjected to the tensile-testing method with an elongation rate of 0.25 mm/min until breaking point. To identify the relationship between the strain and the resistance, the specimens were tested in the elastic region. The strain gauge was tested by staggered loading and unloading, with a constant load of 50 N held for 30 seconds while the resistance and strain were recorded. The load was held to establish whether any hysteresis effects were present as a result of creep or viscoelastic material effects.

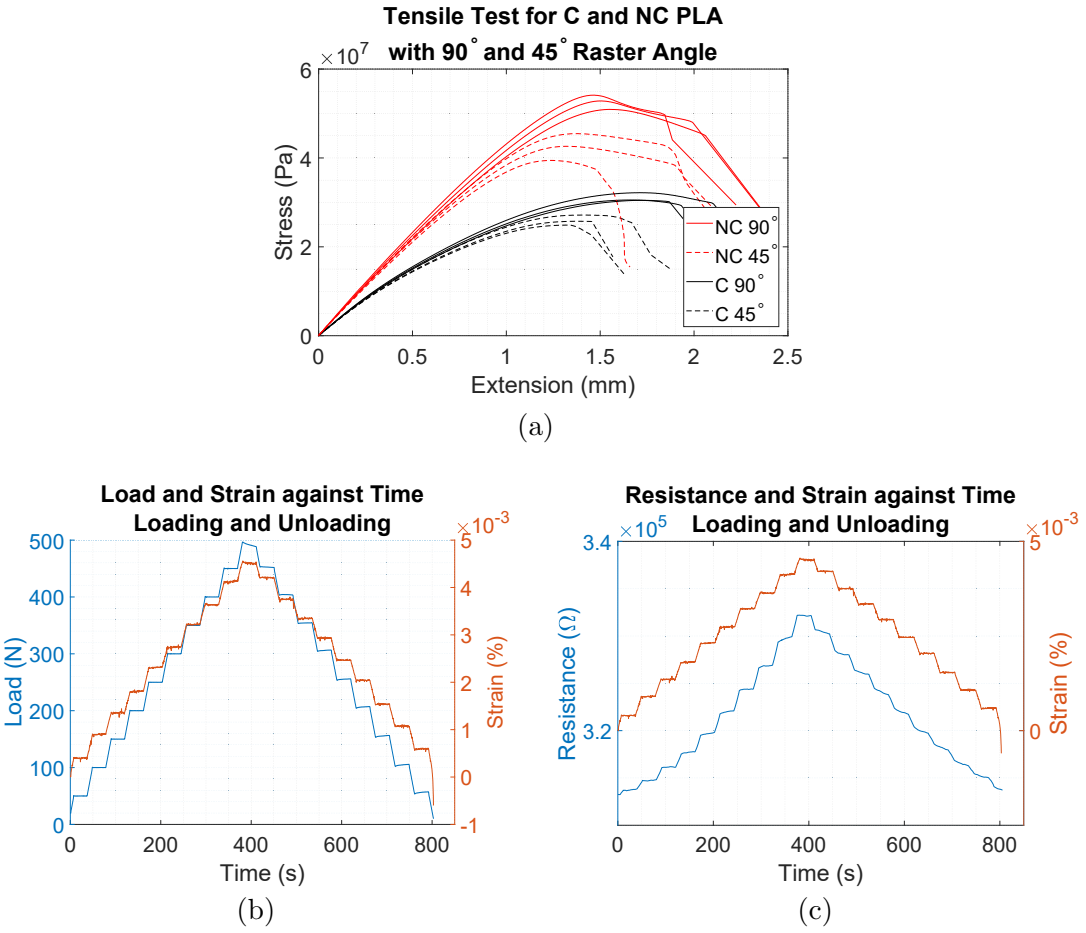

FIGURE 4.6: Experimental results [6]: (a) Standard tensile tests for conductive (C) and non-conductive (NC) PLA with 90° and 45° raster angles; (b) Load and strain data for loading and unloading tests; (c) Resistance and strain data for loading and unloading tests.

Testing was conducted until the strain gauge failed. This showed that plastic deformation occurred after 0.6 kN of applied load with an ultimate tensile strength of 1.3 kN. The test results with the load and strain plotted against the time are shown in Fig. 4.6b. No significant increase can be observed in the strain as a result of the plastic deformation. This shows that the applied 500 N is within the elastic range of the material.

A strain gauge was loaded and unloaded, and these test results are shown in Fig. 4.6c. From these results, a near-linear relationship can be observed between the elongation and the resistance. A minor hysteresis of 6.05% was present between the initial and the end resistance. Additionally, a resistance lag was evident in the strain measurement during the unloading. This behaviour is believed to be a result of the viscoelastic property of the

PLA, or since when the load is released, the specimen may take some time to settle back to its original length.

4.2.4 Microscopic Analysis

Cracks may appear in carbon when the pure material is subjected to a strain. Over time, resistance will be increased because of these cracks, which might affect the measurement of the strain. The material used to print strain gauges is PLA mixed with carbon black (in powder form), which reduces the chances of crack formation. Using a laser microscope (LEXT OLS5000), traces of the tensile-tested strain gauge were observed to verify this assumption. The tensile-tested strain gauge was used for microscopic analysis because traces are on the surface and possible to observe using the microscope. The results of this test are shown in Fig. 4.8. A strip of multiple traces is depicted in Fig. 4.8 and a close-up view of the conductive traces is shown in Fig. 4.8b. No cracks were observed during this experiment, therefore confirming that the traces can handle stress without fissure within the tested strain range, as seen in Fig. 4.6c.

4.2.5 Temperature Testing Setup

For temperature testing, two variables need to be varied: strain and temperature. An insulated box was used since it was necessary for the temperature to remain constant

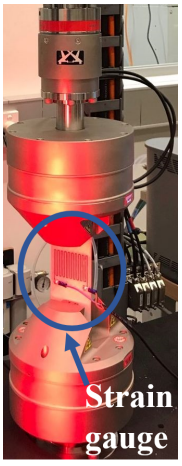

FIGURE 4.7: Testing strain gauge using Instron E10000 machine [5].

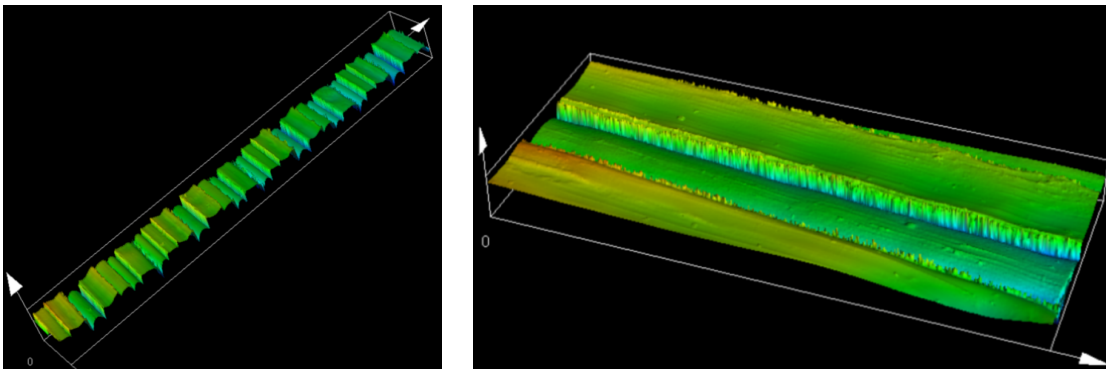

(a) (b)

FIGURE 4.8: Microscope images [6] of: a) Multiple traces; b) A single trace.

throughout the testing. A heating pad (RDK) with the ability to set the temperature was used to control the temperature inside the box. To measure the temperature inside the box, a thermocouple connected to a multi-meter was used. A set of weights (1 kg) was used to change the bending strain, adding 200 g at each step. To test the effectiveness of the temperature compensation, half-bridge and quarter-bridge configurations were tested. A constant voltage of 5 V was supplied to the bridge using a lab power supply and was measured using a $5\frac{1}{2}$-digit multi-meter (PREMA 5017). An overall view of the components used in the testing is provided in Fig 4.3a, and an image of the actual setup is presented in Fig 4.3b.

4.2.6 Temperature Controlled Test Results

During the testing, for each weight change, the temperature was changed from 25 ℃ to 40 ℃ in 5 ℃ increments using the digital heat pad controller, and the voltages were measured. In normal long-term operating conditions, the temperature of the slurry in GSS will generally be at or above normal room temperature, (25 ℃). Therefore, 25 ℃ was selected as the lower bound. The material would warp if the temperature exceeds 40 ℃ and therefore, that would be the maximum recommended operating temperature, which is why 40 ℃ was chosen as the upper bound. The box's temperature was held for 2 minutes to propagate the heat inside the specimen before taking a voltage measurement. To compare the temperature compensation, half- and quarter-bridge configurations were tested using the same method. Test results from the temperature-controlled test are

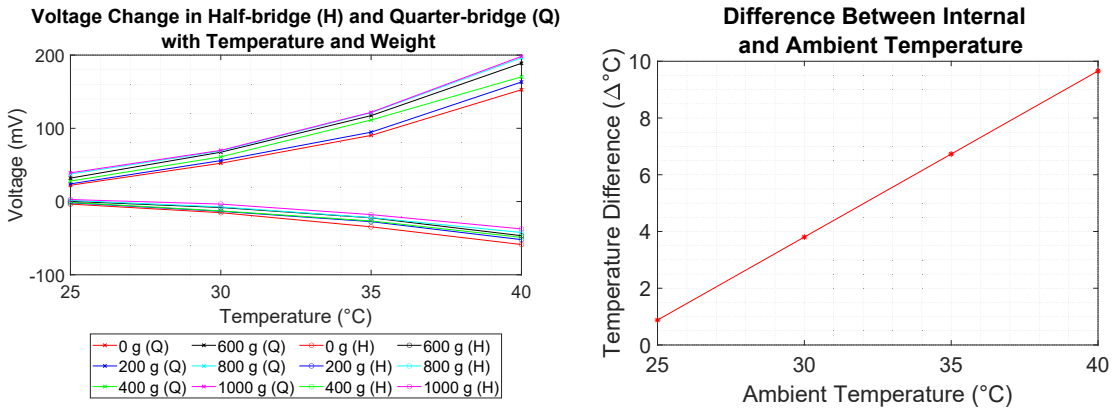

FIGURE 4.9: Experimental results of the sensor [6]: a) Voltage change in half-bridge and quarter-bridge arrangement for different weights and voltages; b) Difference in internal temperature and ambient temperature.

depicted in Fig. 4.9a. The graph shows that the quarter-bridge configuration has an absolute average temperature gradient of 9.85 mV/℃, while the half-bridge configuration has one of 3.16 mV/℃. The gradient represents an error; therefore, a higher gradient means a greater error. Conversely, a lower gradient implies that temperature has a comparatively lower impact on the strain measurement. The results indicate that the proposed half-bridge configuration reduced the gradient by 68% in contrast to the configuration of the quarter-bridge.

4.2.7 ANSYS Temperature Simulation Results

To measure the internal temperature of the traces, it is necessary to embed a temperature probe. Placing a temperature probe with different mechanical properties against the sensor will affect the structural integrity of the strain sensor and change its bending behaviour. The ambient temperature of the box was measured for this reason. It is important to note that, because of the temperature gradient in the material PLA, the actual temperature of the conductive traces in the strain gauges was different from the ambient temperature. An ANSYS simulation was conducted for each of the tested temperatures in the box to investigate this difference in temperature. The results of these simulations are shown in Fig. 4.9b. During the simulations, the sensor was subjected to the same temperatures as the actual sensor—from 25 ℃ to 40 ℃—and, after two minutes, the maximum internal

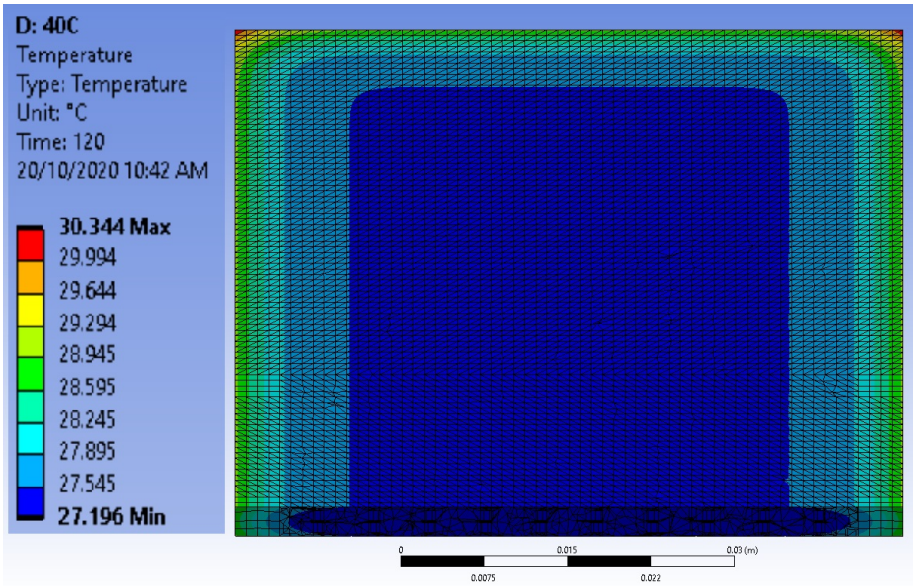

FIGURE 4.10: Simulation result of the internal temperature for the ambient temperature of 40 ℃ [6].

temperature was measured. The simulated temperature distribution for the 40 ℃ is shown in Fig. 4.10. The results show that the maximum temperature difference observable from the simulation was around 9.7 ℃.

4.2.8 Displacement Testing

It was not possible to measure the sensor's deflection when it was inside the box. Therefore, the weight and the resulting voltage change were measured during the temperature-controlled test. A separate rig was developed to overcome this limitation, as shown in Fig. 4.3c. In this setup, to measure the deflection, a Linear Variable Differential Transformer (LVDT) (RDC group LDC2000A) was used. This LVDT sensor was mounted over the strain gauge with a distance (d) of 85 mm from the lab bench, as depicted in Fig. 4.4b. When the weights were applied to the strain gauge, vertical displacement resulted, and the plunger in the LVDT sensor translated this displacement to a voltage change, measured using a multi-meter. The actual deflection can be calculated using the calibration results of the LVDT sensor.

There were two experiments carried out in this setup. The first was conducted to ascertain whether there was any considerable hysteresis in the sensor. From these results, shown in

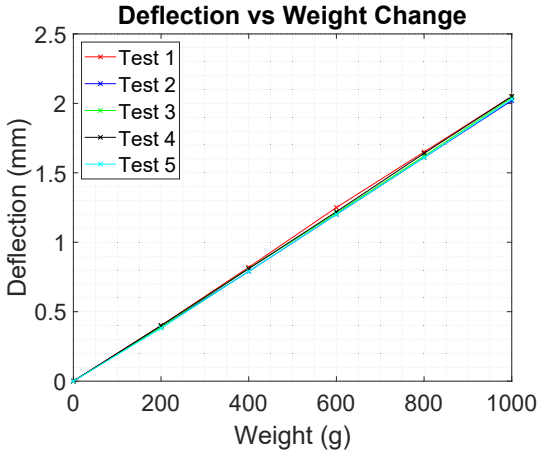

FIGURE 4.11: Deflection vs weight change [5].

Fig. 4.11, it is possible to conclude that there was no significant hysteresis in the sensor. The second test was conducted in the half-bridge setup by measuring the voltage and deflection, since the previous temperature-controlled testing revealed the half-bridge setup to be resilient to temperature variations. The results are given in Fig. 4.12 and demonstrate that the 3D-printed sensor reveals the near-linear relationship between voltage and strain.

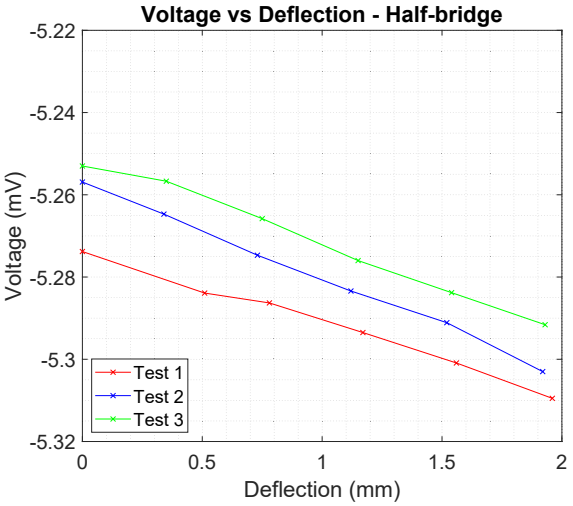

FIGURE 4.12: Deflection testing result for half-bridge [6].

4.3 Discussion and Conclusions

This chapter has presented the design and characterisation of a 3D-printable temperature-compensated strain gauge that can be embedded inside the 3D-printed GSS.

First, a 3D-printed strain gauge was designed to be printed with a combination of conductive and non-conductive PLA. The pure materials were separately 3D printed then tensile tested. The results indicated an increase of approximately 73% in ultimate tensile strength for the non-conductive filament. The raster angle effect was also tested and was demonstrated to be able to affect the tensile strength. This understanding of the material helps to improve the future design of the strain gauge and to predict its effect on the structural integrity of the GSS.

From the tensile testing conducted using the Instron machine, it was possible to understand the relationship between the electrical resistance and the mechanical strain. This relationship is near-linear, indicating that the 3D-printed strain gauge can be used to measure the strain. From the tensile testing, the viscoelastic behaviour of the PLA was observed, whereby the resistance in the gauge delayed the strain change. However, this lagging behaviour was not an issue for this application since this sensor's objective was to measure creep, which occurs over an extended period. Additionally, noticeable hysteresis was not recorded, which indicates no permanent damage to the conductive traces. Printed traces were also examined using a laser microscope to identify defects after subjecting the sensor to testing. However, it was not possible to identify any observable defects.

One limitation of this tensile strain gauge is that temperature changes can affect the strain measurement since printed carbon-based material increases its resistance in response to temperature. Therefore, this research was focused on designing a temperature-compensated strain sensor. The impact of the temperature on the strain measurement was tested using two configurations. One was half-bridge, which is resilient to temperature changes, and the other was quarter-bridge, which is not. The test results showed that the half-bridge configuration was around 68% less prone to temperature variations than the quarter-bridge configuration. Theoretically, the temperature should not affect the strain measurement in the half-bridge configuration. However, around 3.16 mV/°C

of gradient was evident during testing. The reason for this behaviour was that, despite the similarity of the two strain gauges in the half-bridge setup, at the printing stage, a difference of around 90 kΩ of resistance was present. This additional resistance created an unbalanced bridge as the temperature increased, resulting in the temperature gradient observed. When testing in a temperature-controlled environment, it is impossible to measure the sensor's internal temperature, as doing so would require compromising the structural integrity of the sensor. Therefore, an ANSYS simulation has been created to identify the difference between the internal and ambient temperatures. The simulation results revealed the maximum temperature difference to be around 9.7 ℃.

Initially, the strain gauge was tested using the Instron machine for tensile strain. However, the GSS is subject to bending strain. Therefore, a separate test was conducted to measure the deflection with the same weight range used to test the temperature changes. An LVDT sensor was used to measure the deflection, and five bend-and-release cycles were used to determine the hysteresis. The test results showed that the hysteresis was insignificant. Finally, the half-bridge setup was tested by measuring the voltage and deflection and this revealed a near-linear relationship between voltage and bending strain. Therefore, from these results, it is possible to conclude that the proposed temperature-compensated, 3D-printed strain gauge is resilient to temperature variations.

Chapter 5

3D-Printable Sensors to Monitor Acute Damage-causing Characteristics

Monitoring of industrial equipment, such as the GSS, forms an important part of the general inspection and audit process of a work site. Monitoring can help to identify potential problems that were not anticipated during design or task analysis, and damage caused by incorrect operation or incorrect use of the equipment. Two important characteristics have been identified as having the potential to cause acute damage to the GSS: vibration and heat. In line with the motivation of creating an IoT-enabled GSS that can monitor its own state, it is advantageous to incorporate the measurement of these vibration and temperature parameters directly into the structure of the 3D printed object.

Vibration is an important parameter that is valuable to monitor since an excessive amount of vibration can be damaging to the equipment. Therefore, research was conducted to investigate and develop a printable vibration sensor. This proposed sensor is based on electromagnetic induction, a printed conductive filament and a permanent magnet. The initial plan was to print a thin coil to act as an electromagnet. However, the higher resistance and the inability to print coils on top of each other made a permanent magnet the better option.

GSS operate in remote parts of the world that have significant temperature variations. End-users have occasionally been found to misuse the equipment by feeding high-temperature slurry or cleaning solutions into the GSS. For the 3D printing of GSS, new materials are utilised that are different from those previously used. In the case of material failure, it is important to monitor and record the temperatures to which the GSS is subjected. Therefore, this research has focused on developing a 3D printable temperature sensor. During the strain gauge testing, it was observed that the carbon-based conductive filament had a resistance response to the temperature. As it was deemed interesting to investigate this property more, to test the ability to develop a temperature sensor, further research was conducted.

5.1 Methodology

5.1.1 Theory of Electromagnetic Induction

According to Faraday's law of motional emf, for a rigid coil moving at velocity, $\mathbf{v}$, within a stationary magnetic flux density vector field, $\mathbf{B}$, the voltage (or emf), ε, sensed by the coil is given by the line integral along the coil path of the electric field, $\mathbf{E}'$, in the moving coordinate system of the coil, as shown in Eqs. (5.1)-(5.2).

$$\varepsilon = \int \mathbf{E}' \cdot d\mathbf{l} \tag{5.1}$$

$$\varepsilon = \int (\mathbf{v} \times \mathbf{B}) \cdot d\mathbf{l} \tag{5.2}$$

$$x_h = A\cos(\omega t) \tag{5.3}$$

$$\mathbf{v} = v\hat{\mathbf{x}} = (\dot{x}_h - \dot{x}_m)\hat{\mathbf{x}} \tag{5.4}$$

The vibration sensor body is cylindrical and the sensor is attached to a piece of heavy industrial equipment that is monitored, in which the housing is made to oscillate sinusoidally along its cylindrical axis with amplitude, A, and angular frequency, ω, as in Eq. (5.3).

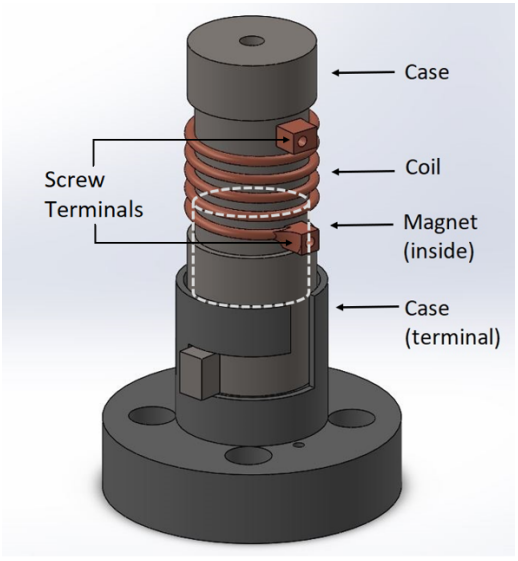

FIGURE 5.1: 3D model of the sensor [7].

The permanent magnet located inside the housing will then acquire an axial displacement, x_m, through friction with the housing. The relative motion of the coil in the axial direction, $\hat{x}$, can be represented by Eq. (5.4).

For the coaxial, cylindrical, axially magnetised magnet in this application, the flux density in the cylindrical coordinates (ρ, φ, x) is $\mathbf{B} = (B_\rho, 0, B_x)$ and $\mathbf{v} \times \mathbf{B} = (0, vB_\rho, 0)$.

5.1.2 Design of the Vibration Sensor

The sensor was printed with two filaments and may be divided into several parts. Those parts are the neodymium magnet (N40), located inside the sensor housing, and the coil, which has been printed using carbon-based PLA with screw terminals to connect wires. This design is shown in Fig. 5.1. The entire casing was printed using PLA and was designed so that the case can be slotted into the base, which for the sake of experiments is then screwed to the vibration exciter.

5.1.3 Principle of Temperature Sensors

Various physical attributes that change with the temperature, such as volume, resistance and electrical resistance, are used to measure temperature. This relationship between the

property R, the temperature coefficient α and the temperature difference dT is shown in (5.5). For the 3D-printed strain gauge, R is the electrical resistance. A linear approximation can be used to calculate the value of R_T for a given temperature T, as well as the reference value of a property R_0 at a reference temperature T_0, assuming α does not change considerably with the temperature. This relationship is shown in Eq. (5.6). However, this equation is valid under the assumption that the R varies linearly according to the temperature. During the experiment for the conductive filament, it was observed that the relationship between R and T is not purely linear. Hence, a non-linear approximation of the polynomial of degree two has been used, as shown in Eq. (5.7), for the temperature range, where A, B and C are constants that are only valid for the temperature range tested.

$$dR/R = \alpha \cdot dT \tag{5.5}$$

$$R_T = R_{T_0}(1 + \alpha(T - T_0)) \tag{5.6}$$

$$R = AT^2 + BT + C \tag{5.7}$$

5.1.4 Accurate Measurement of Resistance

When the temperature changes, it modifies the resistance of the 3D-printed traces. Therefore, it is important to measure the resistance accurately to obtain a correct temperature measurement. To achieve this, a Wheatstone bridge was used. Using this method, it was possible to measure the sensor's resistance by recording ΔV -a voltage relative to the resistance. A Data Acquisition Device (DAQ) was used to measure the voltage accurately. Fig. 5.2a shows this arrangement with different components, including sensor resistance (R_T), input voltage (E), measured voltage (ΔV; calculated as in Eq. (5.8)) and other bridge resistance values (R_1, R_2, R_3).

$$\Delta V = (E^+ - E^-) \cdot \left(\frac{R_2}{R_2 + R_3} - \frac{R_T}{R_1 + R_T} \right) \tag{5.8}$$

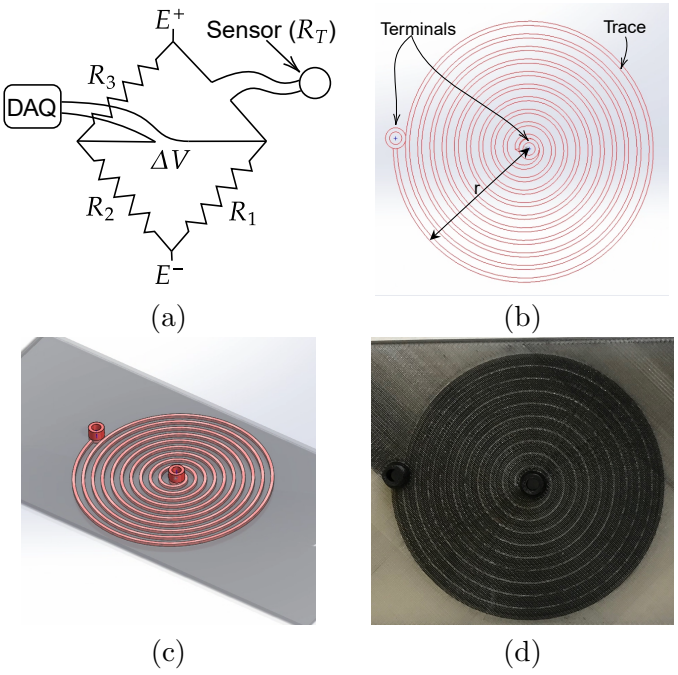

FIGURE 5.2: Sensor designs [8]: a) Wheatstone bridge setup; b) Wire-frame view of the sensor; c) 3D view of the sensor; d) Printed sensor.

TABLE 5.1: Temperature sensor dimensions [8].

Dimension	Value (mm)
Trace width	1.00
Trace height	1.00
Trace length	1041.14
Terminal inner diameter	3.00
Terminal outer diameter	5.00
Terminal height	4.50
Total radious (r)	30.60

5.1.5 Design of the Temperature Sensor

The shape of the sensor is circular, and some traces start from the middle of the sensor, which runs outwards in a concentric spiral pattern. As shown in Fig. 5.2b, there are two terminals - one at the outside and one in the middle. Fig. 5.2c and Fig. 5.2d show a 3D design of the sensor and the printed sensor, respectively. Table 5.1 shows the dimensions of the sensor.

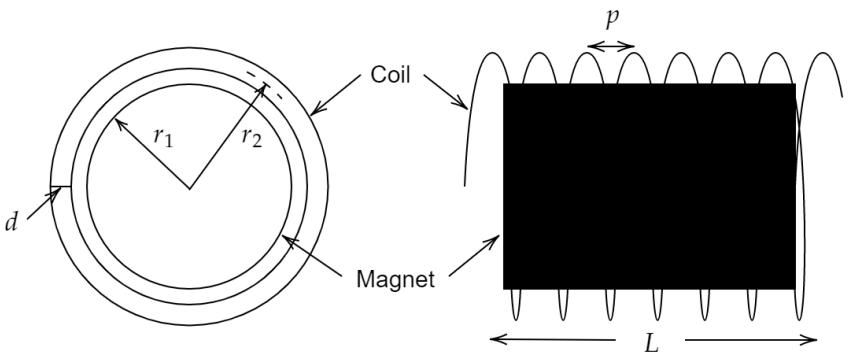

FIGURE 5.3: Simplified diagram of the electromagnetic components in the sensor [7].

5.2 Experimental Setup and Results

5.2.1 ANSYS Simulation Setup of the Vibration Sensor

Initial simulation was conducted to identify the behaviour of the sensor. ANSYS Maxwell from the ANSYS Electromagnetics Desktop Suite 2019 was employed for the simulation. A simplified model was used for the simulation that comprised the actual physical dimensions of the sensor, as shown in Fig. 5.3. Fig. 5.4 reveals that the magnet is coaxial with the coil, and a linear motion along the x-axis was the chosen path for the magnet. The endpoints of the coil were extended outwards and were connected to the ends of a set "region", encapsulating the entire setup in the shape of a rectangular prism with dimensions 80 mm x 80 mm x 130 mm. This boundary region is depicted in Fig. 5.4 and was identified as air with dimensions four times larger than the magnet diameter. As per the requirement of ANSYS, the coil endpoints need to touch the end of the region to assign a current. Therefore, the coil endpoints were extended by 40 mm along the positive and negative sides of the z-axis. During the transient simulation, data were recorded every 0.01 seconds.

Two independent parameters were changed within the simulation model: the velocity of the magnet and the number of coil turns. For the first test, two different velocities, which can be achieved in practice, were simulated: 250 mm/s and 500 mm/s. The second test was conducted at 500 mm/s in all its increments, increasing the number of coil turns by two from one to seven turns. Simulation parameters are shown in Table 5.2.

5.2.2 Simulation Results of the Vibration Sensor

Fig. 5.5 and Fig. 5.6 show the results of the simulation. The voltage induced against the time for five turns for the aforementioned two speeds is shown in Fig. 5.5. The highest voltage value recorded was around 22 mV for 500 mm/s and 11 mV for 250 mm/s. As visible in Fig. 5.5, the induced voltage is proportional to the velocity with an inversely corresponding time scale. The voltage can be generated from the time derivative of the linked flux versus the magnet position $\psi(x)$.

Fig. 5.6 shows the results for the number of turn simulations. According to the results, it is evident that the maximum voltage exhibited by the five-turn coil was 23 mV and the

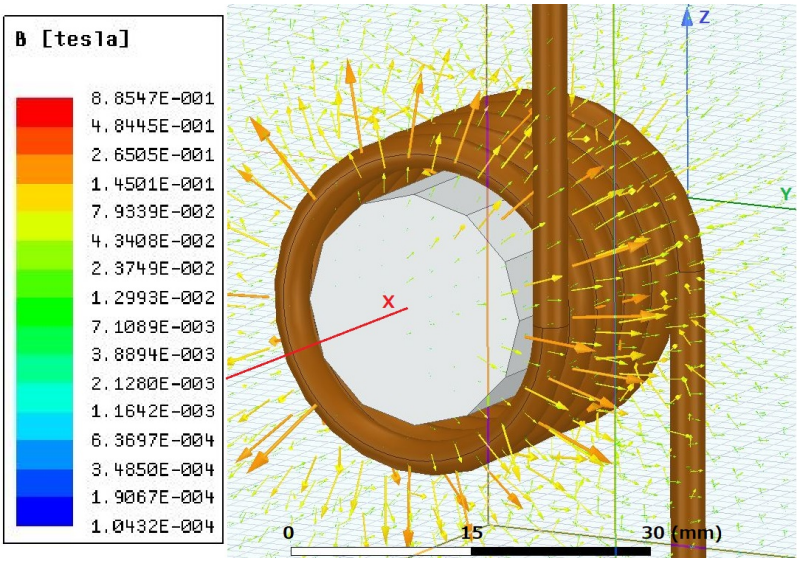

FIGURE 5.4: Simulated magnetic field (5-turn coil) [7].

TABLE 5.2: Simulation parameters [7].

Parameter	Value
Magnet type	Neodymium (N35)
Relative permeability	1.045
Bulk Conductivity	625000 S/m
Magnet diameter ($2r_1$)	20 mm
Magnet axial length (l)	20 mm
Conductor diameter (d)	3 mm
Coil mid diameter ($2r_2$)	26 mm
Coil pitch (p)	5 mm

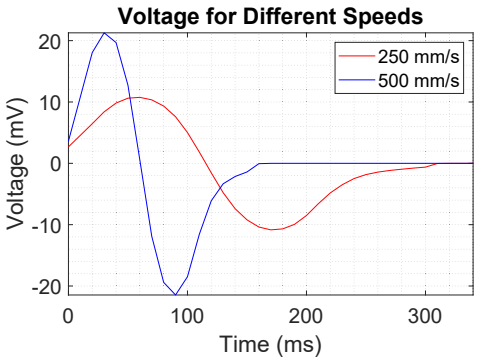

FIGURE 5.5: Voltage vs time for 5 turns at different speeds [7].

lowest voltage from the single-turn coil was about 9 mV. It is clear that the induced voltage increased with the number of turns; however, the voltage per turn reduced in response to the spatial extent of the coil, with only turns near the magnet end face experiencing the peak B_ρ.

5.2.3 Printing the Vibration Sensor Coil

The printer used to print the sensor was a Makerbot Replicator 5^{th} Generation, a single filament commercial 3D printer. Breakaway supports were used to print the coil vertically, as shown in Fig. 5.8. After the printing, trimming and cleaning were required. The casing also required further trimming and cleaning. However, the amount of printed support material was minimal. Table 5.3 shows the print settings used.

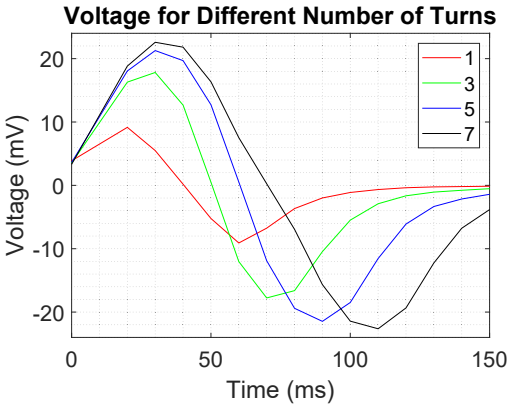

FIGURE 5.6: Simulated voltage vs time for 500 mm/s and different number of turns [7].

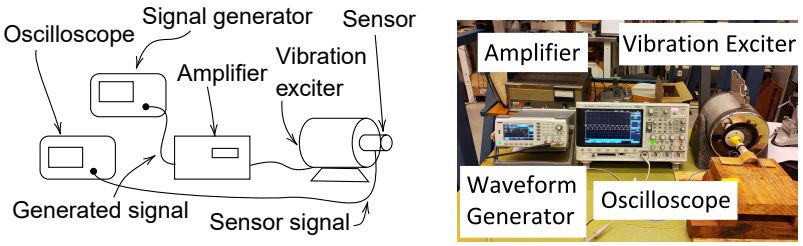

(a) (b)

FIGURE 5.7: Experimental setup [7]: a) Block diagram of components; b) Laboratory setup.

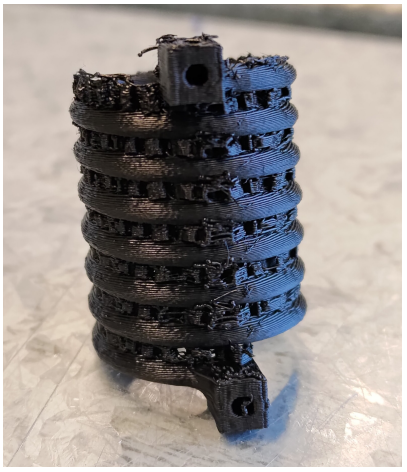

FIGURE 5.8: Printed coil with supports [7].

5.2.4 Experimental Setup of the Vibration Sensor

There were five components in the test construction: the amplifier, the waveform generator, the oscilloscope, the vibration exciter and the sensor, as shown in Figs 5.7a and b. The waveform generator was connected to the amplifier, which supplied the voltage required

TABLE 5.3: Print parameters used for the sensor coil [7].

Parameter	Value
Nozzle diameter	0.4 mm
Bed temperature	60 °C
Nozzle temperature for PLA	215 °C
Nozzle temperature for conductive PLA	215 °C
Printing speed PLA	90 mm/s
Printing speed conductive PLA	20 mm/s

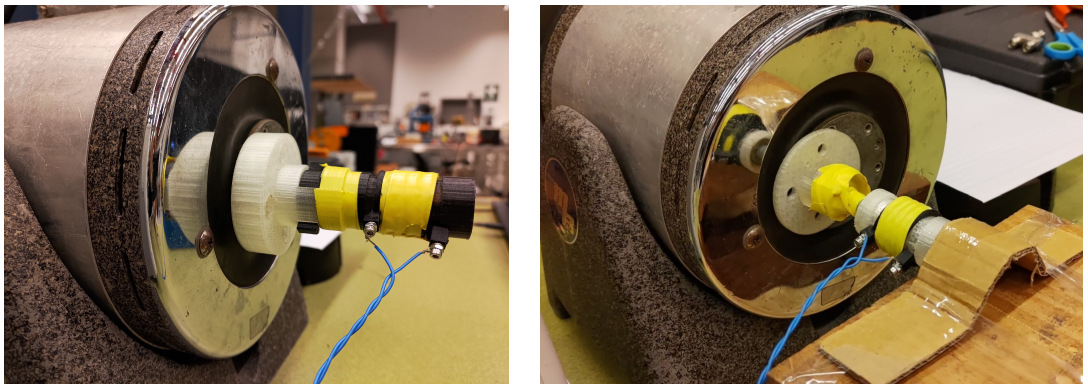

(a) (b)

FIGURE 5.9: a) Moving coil with magnet setup [7]. b) Stationary coil setup [7].

to run the vibration exciter. The waveform generator was used to control the exciter's frequency and amplitude, whereas the oscilloscope measured the sensor's signal. As shown in Fig. 5.9, a sensor was mounted on the vibration exciter horizontally, with terminals connected to the oscilloscope for voltage measurements. Table 5.4 shows the specimen parameters. The vibration exciter used for the experiment was the MB Electronics Model PM50, with the amplifier MB Electronics Model 2250. The Tenma 72-3555 Function/Arbitrary Waveform Generator [194] was the waveform generator employed. DSO-X 2004A [195], by Keysight Technologies, was the oscilloscope used. There were two different experimental configurations, as described in the next two sections.

TABLE 5.4: Experiment parameters [7].

Parameter	Value
Conductor diameter (d)	3 mm
Coil mid diameter ($2r_2$)	26 mm
Coil pitch (p)	5 mm
Number of turns (N)	5
Magnet type	Neodymium (N40)
Magnet diameter ($2r_1$)	20 mm
Magnet axial length (l)	20 mm

5.2.4.1 Moving Coil with the Magnet

In this arrangement, as shown in Fig. 5.9, the initial tests were conducted using the entire specimen, with a magnet contained inside, mounted on the vibration exciter. The casing vibrated along with the exciter because of its rigid attachment by bolts. The magnet moved inside the cavity freely but with a limited range and, for certain amplitudes and frequencies, the magnet rebounded against the "walls" at the ends of the casing. There was a 30 mm maximum distance of travel.

5.2.4.2 Stationary Coil and Moving Magnet

The second type of tester was a moving magnet with an open-ended stationary coil fixed in space, as shown in Fig. 5.9b. A non-magnetic clamp was holding the coil, and the magnet was mounted to the exciter. The reason for conducting the second test was that an occasional irregular shaking of the magnet inside the closed space was observed in the first test, which may have interfered with the maximum travel of the magnet. The open-ended coil allowed for the unobstructed vibration of the magnet, enabling comparisons with the first test, to ascertain the effects of the magnet "rebound" and comparisons with the simulation results. This second test was also conducted with the same vibration exciter, under the same conditions as the first test, to remove the magnet's motion uncertainty.

5.2.5 Material and Printing Process of the Temperature Sensor

Proto-pasta PLA material was used for the conductive traces, which contained carbon black and PLA. Before printing, the resistivity of this material was rated at 15 Ω.cm and, after printing, this increased to 115 Ω.cm along the Z-axis and 30 Ω.cm along the X–Y plane. To print the sensor, a material extrusion printer [24] — Prusa i3 MK3 with the Multi-Material Unit 2.0 attachment — was used. This printer has the ability to print using five filaments with a single nozzle. During the printing process, the nozzle temperature was set to 240 ℃ for the conductive filament and to 210 ℃ for PLA.

5.2.6 Experiment Environment Setup of the Temperature Sensor

During the experiment, the DAQ (PicoLog 1000 series data logger) was used to supply a constant voltage (5 V) to the bridge circuit and to measure and log data into a computer. As shown in Fig. 5.10a, a variable resistor was used to balance the bridge and set the resistance equal to the sensor. The sensor was placed inside a box, as shown in Fig. 5.10b, to maintain a constant temperature without significant impact from the outside environment. A thermocouple, connected to a data-logging multimeter, which was wirelessly tethered to a computer, was used to log the data. Fig. 5.11 shows this wireless connection as an unbroken line to illustrate the connection. The thermocouple was placed on the sensor and connected to it using a metallic tape. Then, the sensor was placed on top of a temperature-controllable heat pad (RDK). This heat pad had a button that could be used to set the temperature, and a display to show the current temperature. Further,

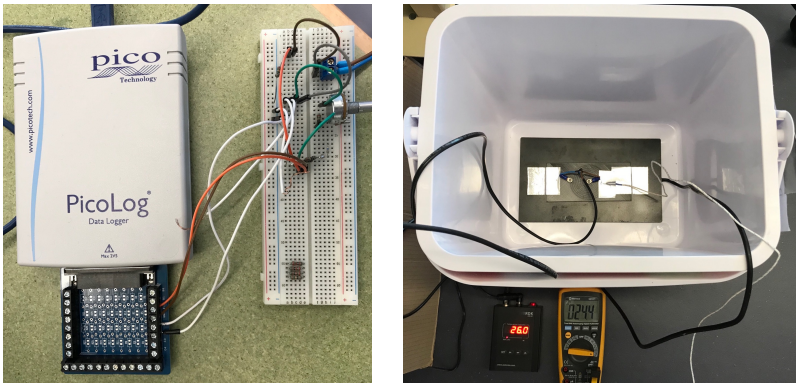

(a) (b)

FIGURE 5.10: Real-world experimental setup [8]: a) DAQ and the bridge circuit; b) Sensor with a data logging multimeter.

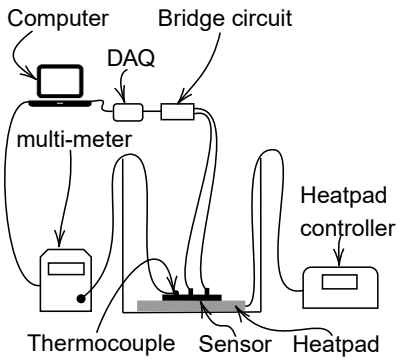

FIGURE 5.11: Data logging setup for the experiment [8].

to create a strong thermal contact, the sensor was attached with metallic tape to the heat pad. The setup of the experiment is shown in Fig. 5.11.

5.2.7 Results

5.2.7.1 Moving Coil Along With the Magnet

Two variables were tested in the first experiments, namely, frequency and amplifier input amplitude. The RMS voltage generated was measured for varying amplifier input amplitudes and frequencies adjusted by the waveform generator. The amplifier's amplitude gain was set to be 5x, and this amplification was kept constant throughout the tests. As the peak-to-peak voltage can potentially fluctuate in response to extreme values, the maximum and minimum RMS voltages were instead measured to increase reliability. This was achieved by allowing the specimen to oscillate for 20 seconds and recording the highest and lowest RMS voltages over 2 second intervals within the 20 second duration. The amplitude was raised from 2 Volts peak-to-peak (V_{pp}) in increments of 1 V_{pp} to 5 V_{pp}. At each of the amplitude steps, the frequency was varied; it was initially set at 4 Hz and was raised in increments of 2 Hz to 10 Hz. The results of the tests can be seen in Fig. 5.12a and b.

Only measurements up to the 4 V_{pp} range will be considered since the 5 V_{pp} range caused the amplifier to "overcurrent". The highest frequency (10 Hz) and amplitude (4 V_{pp}) gave the greatest generated voltage at a maximum of 22.1 mV Root Mean Square (RMS) (Fig. 5.12b) and a minimum of 5.4 mV RMS (Fig.5.12a). Comparing the maximum and minimum graphs shows the erratic behaviour of the magnet. For example, as previously stated, at 10 Hz 4 V_{pp}, the maximum induced voltage recorded was 22 mV RMS, while the minimum was 5 mV RMS—a difference of 17 mV. At this frequency and amplitude, the magnet rebounding off the casing walls introduces harmonics that cause short bursts of oscillation at a higher or lower frequency, providing a large variation between the minimum and maximum induced voltage in an inconsistent voltage induction.

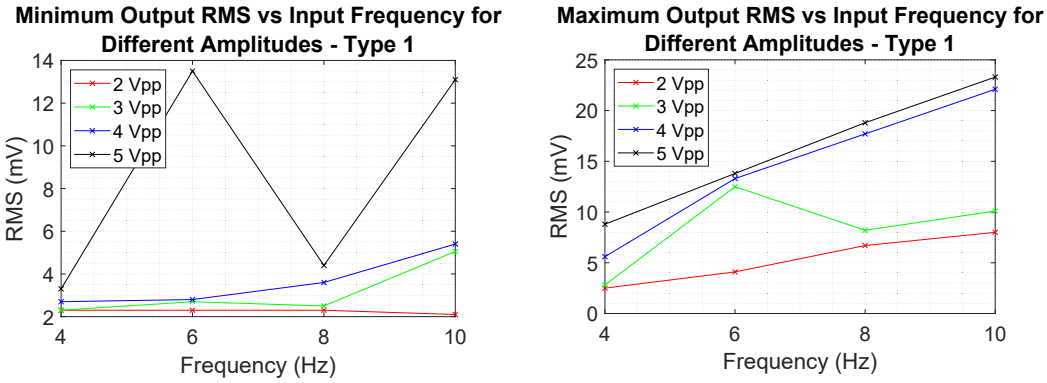

(a) (b)

FIGURE 5.12: Moving coil (Type 1) results for the magnet's maximum internal travel of 30 mm [7]: a) Minimum RMS; b) Maximum RMS.

5.2.7.2 Moving Magnet With Stationary Coil

As stated earlier, the second experiment was conducted for the same device components but with the magnet fixed to the vibration exciter and moving within an open-ended case for unobstructed oscillation. There were three variables tested: frequency, amplifier input amplitude, and the number of coil turns. The initial amplitude was the same as in the first arrangement: 2 V_{pp}, increasing in increments of 1 V_{pp} to 5 V_{pp}, with the frequencies increasing from 4 Hz to 10 Hz in 2 Hz increments. The amplifier "Amplitude" dial was set to five out of ten. As the readings were consistent and not fluctuating, there was no need to measure for a minimum or maximum induced voltage.

As a result of the amplitude being measured in peak-to-peak voltage, a test was also conducted to translate the relationship between the amplitude and the travel—that is, the moving distance—of the vibration exciter. This was achieved by setting up a slow-motion camera (240 fps) on a tripod facing the side of the vibration exciter, with a non-steel ruler placed alongside the housing. The inferred travels, tolerance $\pm$ 1 mm, are shown for 10 Hz in Fig. 5.14. In the graph, a near-linear dependence on the travel by the amplifier input amplitude can be discerned.

A comparison of the videos for 5 Hz and 10 Hz indicated that the travel was approximately independent (within tolerance) of the frequency for a given V_{pp}. Fig. 5.13a and Fig. 5.13b plot the position and inferred velocity versus the time for the moving magnet (Type 2)

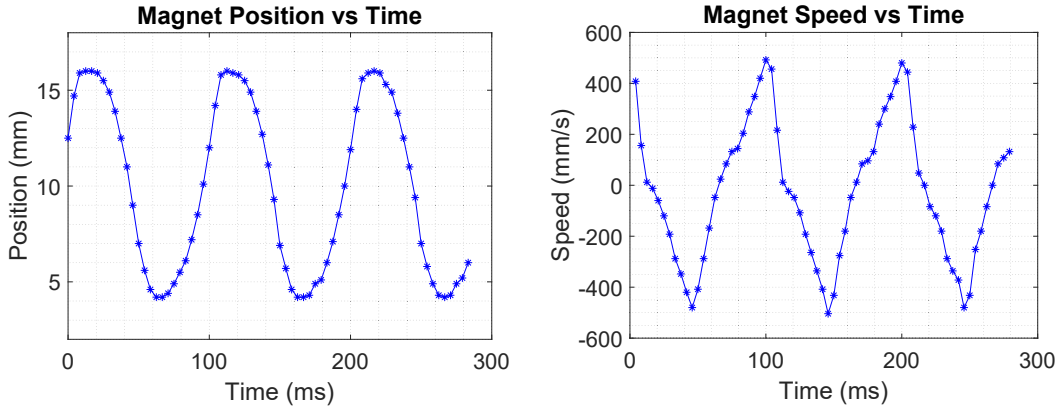

(a) (b)

FIGURE 5.13: Moving magnet tests (Type 2) [7]: a) exciter position versus time for 4 V_{pp} with 10 Hz excitation and travel 12 mm; b) speed vs time of the exciter.

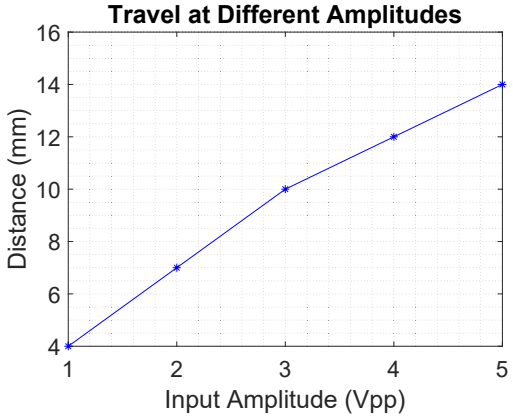

FIGURE 5.14: Moving magnet tests (Type 2) travel of the vibration exciter vs input amplitude for 10 Hz [7].

4 V_{pp} and 10 Hz test—with travel distance of approximately 12 mm—indicating that the exciter motion deviates from the sinusoidal.

The sample coil voltage waveform (Fig. 5.16) exhibits features similar to the velocity waveform (Fig. 5.13b), indicating that the non-sinusoidal exciter velocity profile has contributed to harmonics in the voltage waveform.

In Fig. 5.15a, we can see that the highest voltage (RMS) recorded was 10.66 mV, from an amplitude of 4 V_{pp} at a frequency of 10 Hz, with the lowest at 2 V_{pp} at a frequency of 4 Hz, generating 3.19 mV.

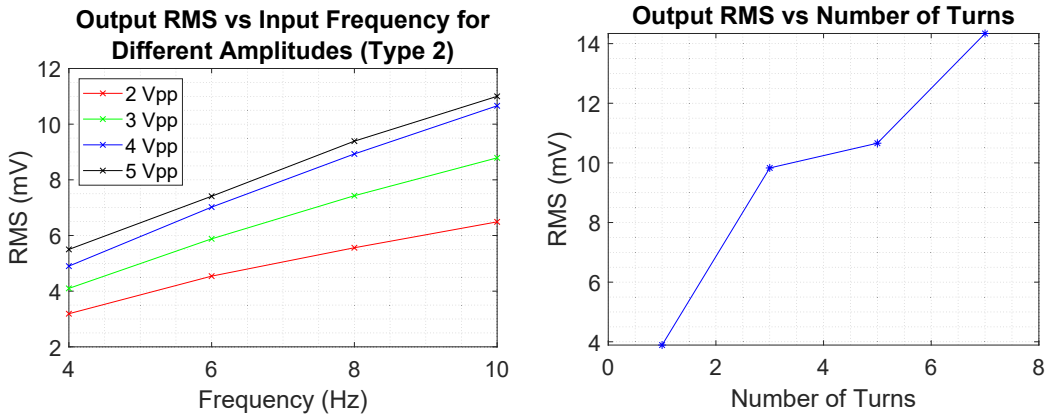

(a) (b)

FIGURE 5.15: Moving magnet (Type 2) results [7]: a) output signal RMS for different input frequencies for 5 turns; b) output signal RMS for different number of turns at 10 Hz and 4 V_{pp}.

The coil turn test was conducted at an amplitude of 4 V_{pp} at 10 Hz for one, three, five and seven coil turns. The results are shown in Fig. 5.15b, for which an increase in the number of turns led to an increase in the voltage induced. One coil turn generated 3.89 mV (RMS), increasing to 9.83, 10.66 and 14.34 mV for three, five and seven coil turns, respectively.

TABLE 5.5: Comparison of ANSYS simulation and experimental results (mV RMS) for 4 Vpp input amplitude [7].

Predicted (mV)	Measured (mV)	Pred./Meas.
4.69	4.9	0.96
7.04	7.02	1.00
9.38	8.93	1.05
11.73	10.66	1.10

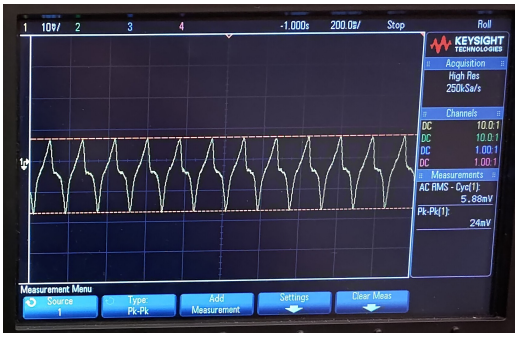

FIGURE 5.16: Sample signal received from the sensor in oscilloscope at 6 Hz and 3 V_{pp} [7].

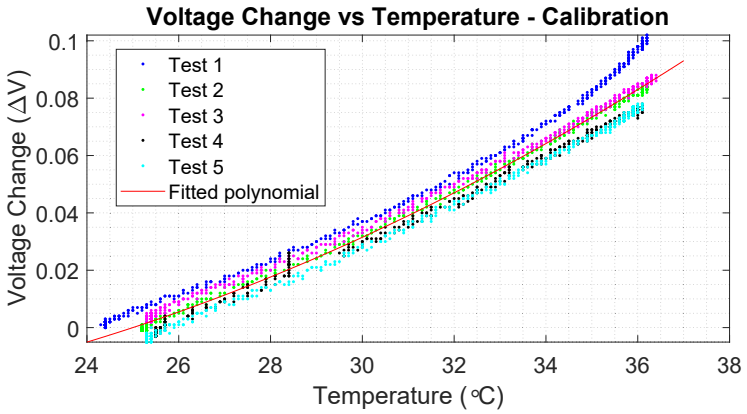

FIGURE 5.17: Calibration test results for a fitted polynomial to predict the voltage change at a given temperature [8].

5.2.7.3 Calibration and Testing of the Temperature Sensor

Five tests were conducted to calibrate the sensor and the temperature and the voltage change ΔV were recorded. Initially, the heat pad was at room temperature (24–26 ℃), then its temperature was set to a constant temperature (38 ℃). The upper limit of this temperature was chosen because PLA starts to deform at around 42 ℃. Therefore, the maximum temperature was selected at slightly below 42 ℃. At the beginning of the test, the heat pad was turned on and the voltage and the temperature values were periodically logged at the same time until the heat pad had reached the set temperature. This was considered a single testing cycle and, afterwards, the whole system was set to cool to room temperature. After plotting the ΔV against the temperature, it was observed that a polynomial of degree two was the best fit for the measured relationship. By fitting a polynomial of degree two, the constant values of $A = 0.0002, B = -0.0051 and C = -0.0016$ were obtained, as per Eq. (5.7). Fig. 5.17 shows the calibration test results.

After its characterisation in the calibration step, the sensor was tested by measuring the voltage required to predict the temperature using the previously fitted polynomial. This testing was conducted in the same way as before, using the heat pad and measuring the voltage and the temperature. Fig. 5.18 shows the various test cases and predicted temperatures using the fitted polynomial. Additionally, Fig. 5.19 shows the absolute error for each test; from this graph, it is possible to observe that the maximum absolute error was less than ±2 ℃ within the temperature range of interest (24–26 ℃).

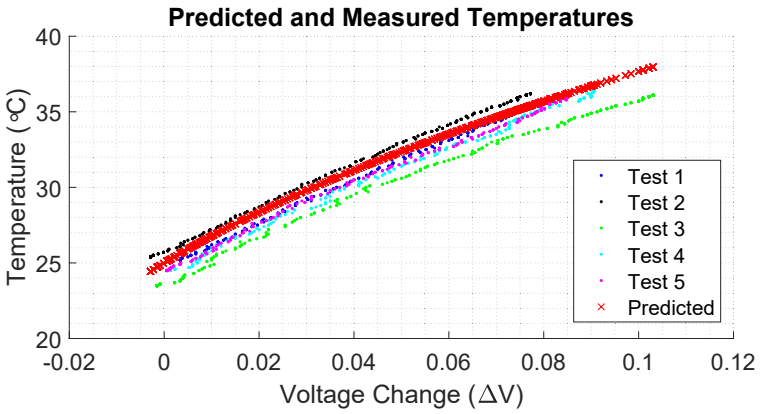

FIGURE 5.18: Temperature prediction test results [8].

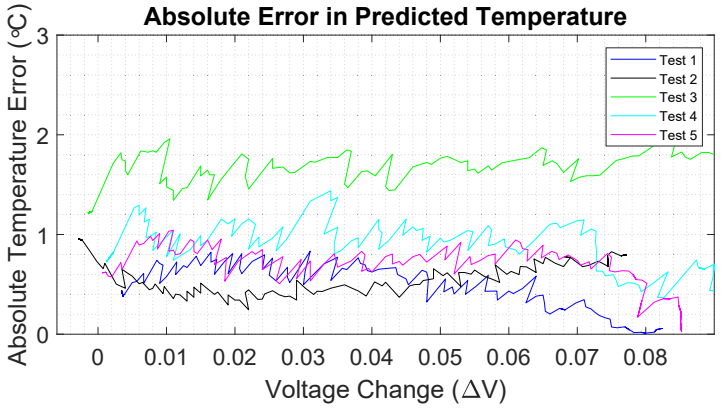

FIGURE 5.19: Absolute error in the temperature as the voltage changes for the 5 tests [8].

5.3 Discussion and Conclusions

This chapter has presented two embedded 3D printed sensor designs that can enable GSS to monitor characteristics that can cause acute damage to the equipment, either due to unexpected use or misuse. To this end, this chapter works to understand the electromagnetic induction properties in 3D printed material to develop a prototype vibration sensor, and to extend extrusion printing techniques for carbon-based filament to 3D print a novel temperature sensor.

The developed prototype vibration sensor allowed for the analysis of electromagnetic induction in commercially available conductive filament. Initially, an ANSYS simulation was conducted to understand the general design parameters, including velocity and number of turns.

The two experiment models generated for the vibration sensor gave significantly different results. The first model proved capable of voltage induction (RMS); however, it displayed results that were inconsistent as a result of the frequent "irregular shaking" experienced by the magnet inside the specimen. This result is attributed to the components gaining higher frequency motion by "rebounding" off the ends. The second test with the magnet moving within a stationary coil involved no such rebounding. With a 12 mm magnet travel, the second test was capable of an induced voltage of up to 10.66 mV (for a five-turn coil, oscillating at 4 V_{pp}, at 10 Hz). In all experiments, as the number of turns increased, the amount of induced voltage also increased.

When comparing the maximum induced voltage between the two experiment types, we can see that the first setup exhibited an overall higher voltage induction. However, a more important concern when implementing this model is its reliability. The need to measure both minimum and maximum RMS voltages means that the induction is unreliable and that receiving a concrete reading would pose a challenge. Examining the graph in Fig. 5.12a, the minimum RMS voltage can be as low as 2 mV. Matching each amplitude and frequency of this graph to the maximum induced voltage in Fig. 5.12b, the jump can be as large as 17 mV in response to the same conditions. Further, as this occurs in short bursts, simply averaging the results between the minimum and maximum would be inaccurate. Another concern is the robustness of and the wear on the specimen. Continuous impact against the magnet ends can cause failure as a result of fatigue and tensile stress. During the testing of the first configuration, the end of the specimen actually broke off. The minimum RMS voltage for 10 Hz and 4 V_{pp} was 5.4 mV RMS for the moving coil test (Type 1), half that of the 10.66 mV RMS for the moving magnet test (Type 2). The voltage was lower in the moving coil tests with no magnet rebounding because the motion of the magnet induced by friction reduced the relative motion of the coil and magnet, $\mathbf{v}$ in Eq. (5.4).

FEA can be used to predict the RMS voltage of the Type 2 experiments as follows. Approximating the motion as sinusoidal, for the maximum travel of 12 mm at 10 Hz for 4 V_{pp}, $A = 6\ mm$ and $\omega = 62.83\ rad/s$ in Eq. (5.3) and the maximum magnet velocity would be $\omega A = 377\ mm/s$. From Fig. 5.6, the predicted amplitude of the sinusoidal voltage for a five-turn coil, if positioned to obtain the maximum voltage, would be $(377/500) \times 22\ mV = 16.59\ mV$. The ϵ waveform is not sinusoidal, even for sinusoidal

motion, because the ϵ for a given speed falls away from the peak (Fig. 5.5). Thus the RMS would be somewhat lower than $1/\sqrt{2}$ times the amplitude of 11.73 mV. From Fig. 5.15a, the measured RMS voltage in the moving magnet test (Type 2) was about 10.66 mV, which was 10% lower than the prediction. Using this method, with the same travel distance of 12 mm applied at other frequencies, the voltages at 4, 6 and 8 Hz at 4 V_{pp} were also predicted and are shown in Table 5.5, where we can see that the results accord with the analysis.

Measuring vibration is an important factor in equipment monitoring since excessive vibration can cause permanent damage. Therefore, this research was conducted to design and develop a printable vibration sensor. The proposed sensor was designed and developed with conductive filament and a permanent magnet. Then simulations and experiments have been used to show how a vibration sensor was created and modelled through an understanding of the behaviour of electromagnetic induction in a 3D printed material created from a commercially available conductive filament.

From the temperature sensor test results, it can be observed that the developed 3D-printed temperature sensor and the Wheatstone bridge-based voltage measurement method can measure temperature with an error margin of ±2 ℃, which is less than the acceptable error margin of ±5 ℃. The testing results show that the resistance and temperature have a relatively linear relationship. However, to ensure greater accuracy, a polynomial of degree two was used. The proposed sensor was developed and printed using inexpensive carbon-based conductive material embedded in a PLA base. This sensor could be embedded inside any 3D-printed object with similar material composition to measure its temperature. The significant advantage of using a printed sensor over the traditional temperature probe inside a 3D-printed object is the ability to print the sensor in line with the object, eliminating any post-processing involved. Otherwise, it is necessary to provide space for conventional sensors in the object and, since conventional sensors are made with different material, they might affect the structural integrity of the object. This becomes a crucial issue if the sensor needs to be embedded deep inside the material. Conversely, an advantage of traditional sensors would be that they do not require calibration since they are already calibrated when they are manufactured.

Chapter 6

Partially-filled Pipe Flow Meter

During normal operating conditions, the slurry is continuously pumped into the top of each GSS via partially filled pipes. The flow rate of the slurry is important since it affects the mineral separation process. Although it is important to measure the flow rate, the challenge is that a normal flow meter becomes erroneous when measuring the flow in this sort of partially filled pipe. Therefore, research was conducted to develop a non-intrusive flow meter to measure pipes with a partial flow.

In this research, an ultrasonic flow meter has been used to develop a flow meter for partial filled pipes. The main reason is that this type of flow meter is non-intrusive and can be mounted on different pipes of different diameter. Two measurements are required to determine the flow rate inside a pipe: the cross-sectional area of the pipe and the flow velocity. The temporal difference between and against the flow of ultrasonic signals is used in transit time flow meters to calculate the fluid flow [196]. In a pipe that has a uniform diameter, the cross-sectional area can be assumed to be constant. In full pipes, the propagation path of the sound depends on the mounting method (i.e. the "W-", "Z-", "V-", "N-" methods) of the transducers [197]. With knowledge of the time measurement, it is possible to calculate the flow rate. However, in a pipe that is partially filled, the propagation path and the cross-sectional area are unknown. Therefore, accurately measuring the flow rate using only the ultrasonic sensor is not possible.

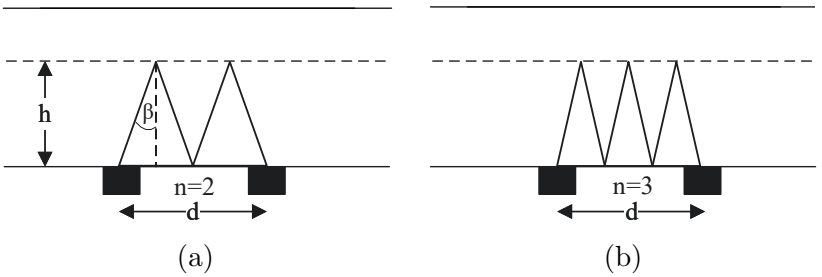

FIGURE 6.1: Possible propagation patterns from the V-method in a partially filled pipe [9]: a) When number of peeks are two; b) When number of peeks are three.

6.1 Methodology

6.1.1 Principle of Transit Time Flow Meters

Ultrasonic flow meters do not have any parts that are moving nor do they undergo any pressure drop. This is one of the main advantages of this type of flow meter, in contrast to the orifice, vortex or turbine flow meters [198].

Piezoelectric transducers have been used in ultrasonic flow meters to receive and transmit acoustic pulses. These transducers can be mounted on to the pipe in different ways, for example, the N-method, the Z-method, the W-method and the V-method [197]. In this research, transducers are attached on the same side of the pipe, which is the V-method. The reason for using this method is that transducers can identify sound waves bounced back from the liquid's surface, as shown in Fig. 6.1. Further, this V-method is applicable to the pipes used in GSS in which the diameter ranges from 15 mm to 200 mm [197].

In Fig. 6.2, the pipe's inner diameter is D, the velocity of the flow is V, the total travel distance is L, the angle between flow velocity and the sound wave is α and A and B are the transducers. The upstream sound propagation time is t_{up} and the downstream sound

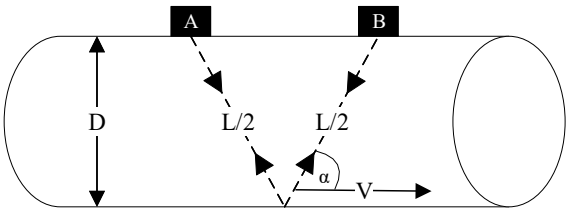

FIGURE 6.2: V-method sound propagation pattern in a full pipe [9].

propagation time is t_{down}. When there is no flow in the pipe, the difference between these two values is zero and the travel time of the sound waves is affected when there is a flow. The speed of the sound waves in the liquid is C; hence, the transit times can be calculated as:

$$t_{up} = L \;/\; (C - V\cos(\alpha)) \tag{6.1}$$

$$t_{down} = L \;/\; (C + V\cos(\alpha)) \tag{6.2}$$

$$V = \frac{L}{2\cos(\alpha)}\left(\frac{1}{t_{down}} - \frac{1}{t_{up}}\right) \tag{6.3}$$

$$\dot{Q} = AV \tag{6.4}$$

For a given liquid at a given temperature, C is a constant. Therefore, Eq. (6.1) and Eq. (6.2) can be combined and, from this, it is possible to derive Eq. (6.3) [199]. If the cross-sectional area, A, represents a full pipe, the flow rate can be calculated using Eq. (6.4). Additionally, in commercial flow meters, the thickness of the pipe and the material of the pipe is also considered when calculating the propagation time.

6.1.2 Determining Sound Propagation Path

The distance over which the ultrasonic waves travel, L, is required to calculate the flow velocity, as shown in Eq. (6.3). This distance is measurable when the pipe is full. When commercial flow meters are initially set up, the pipe material, pipe diameter, pipe thickness and the liquid type allow for the calculation of the distance between the transducers. Then, the transducers are mounted onto the pipe according to this recommendation. When the pipe is not filled, the reflection pattern is unknown and various propagation patterns might occur, as shown in Fig. 6.1, where the number of peaks that can occur is n, the distance between transducers is d, the set of positive integers is n ($n \in \mathbb{Z}^+$) and the horizontal dashed line is the liquid level.

The propagation path can be computed numerically for the partial filled pipe. The goal is to find a pattern that contains an incidence angle close to that when the pipe is full. By

calculating the incidence angle, β, and then the travel time, t, the L can be calculated for different n values.

$$\beta = tan^{-1}(d \ / \ 2nh) \tag{6.5}$$

$$L = 2nh \ / \ \cos(\beta) \tag{6.6}$$

$$t = L \ / \ c \tag{6.7}$$

The following steps can be used to identify the propagation pattern:

1. Calculate β for a full pipe using (6.5), where $n = 1$ and h is equal to the inner diameter of the pipe.
2. For different liquid heights, h, change n and calculate β.
3. For each liquid height, determine the n that offers the least deviation for a calculated β and a full pipe β.
4. Use n to give the propagation pattern for that specific flow height.
5. Then use n to calculate the travel distance with (6.6) and the liquid velocity using (6.3).

6.1.3 Measuring Height of the Liquid

If the liquid height is known, the propagation path can be determined and, eventually, the velocity of the flow can be calculated. To calculate the flow rate, it is necessary to have a cross-sectional area, as per Eq. (6.4). For GSS, the properties of the flow, such as density, can change over time and, therefore, capacitance-based height measurement has been used. However, environmental changes, such as humidity, can affect the capacitance measurement; thus, using a single sensor might require calibration. Therefore, to make the measurement independent of the liquid, air and dielectric constants of the container, a three-electrode design has been used. This arrangement of the three electrodes—the level electrode, liquid electrode and environmental electrode—is shown in Fig. 6.3.

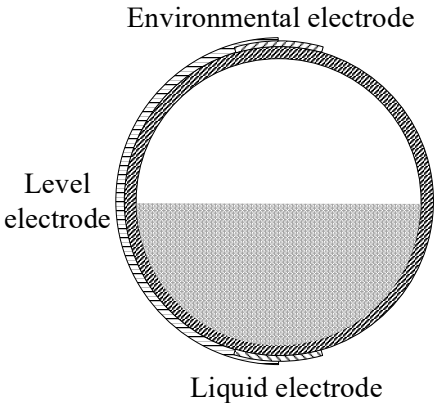

FIGURE 6.3: Electrode placement around the pipe [9].

The liquid height can be determined as follows [200]:

$$Level = h_{ref} \frac{C_{Lev} - C_{Lev}(0)}{C_{RL} - C_{RE}} \tag{6.8}$$

Here, h_{ref} is the height in the desired units of the pipe, C_{Lev} is the current capacitance in the level electrode, $C_{Lev}(0)$ is the capacitance of the level electrode when empty, C_{RL} is the capacitance of the liquid electrode, and C_{RE} is the capacitance of the environmental electrode.

This method has been used to measure the liquid height in this research; then, using the liquid height, the propagation path can be determined and, using Eq (6.9), the cross-sectional area can be calculated.

$$A = \frac{D^2}{4} \cos^{-1}\left(\frac{D-2h}{D}\right) - \left(\frac{D-2h}{2}\right)\sqrt{Dh - h^2} \tag{6.9}$$

Here, the cross-sectional area of the liquid is A, the inner diameter of the pipe is D and the liquid height is h.

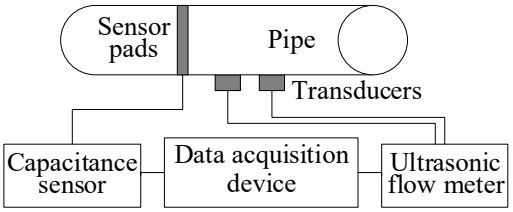

FIGURE 6.4: Proposed sensor fusion concept [9].

6.1.4 Determining Accurate Flow Rate

Using the capacitance-based method, the liquid height can be determined, which indirectly helps to determine the correct flow rate, allowing the cross-sectional area to be calculated. This arrangement is shown in Fig. 6.4, and the process is depicted in Fig. 6.5.

6.2 Experiment and Results

6.2.1 Experiment Rig Setup

A test rig was developed with a 4 m long pipe and a pump to pump the water into the pipe, as shown in Fig. 6.7a. The TUF-2000M ultrasonic flow meter had two transducers connected to the pipe and is shown in Fig. 6.7b. The Modbus protocol can be used to communicate with the flow meter [197] and a python program was written to read the data in real time. Fig. 6.8 shows the dimensions and setup of the rig. The flexible PCB was mounted onto the pipe using tape and transducers were mounted using cable ties. The

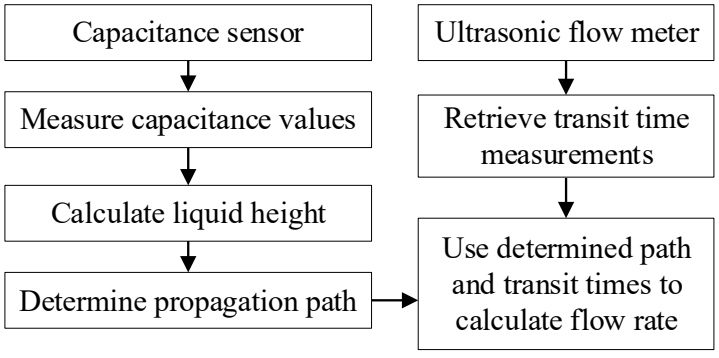

FIGURE 6.5: Steps to determine the correct flow rate [9].

(a) (b) (c)

FIGURE 6.6: Capacitance sensor [9]: a) Multiple layers of flexible PCB; b) Flexible PCB after manufacturing; c) Capacitance sensor testing with water level.

transducers were positioned according to the manufacturer's specifications considering the liquid inlet and outlet locations. The transducer distance (d_1) was determined by the flow meter according to the pipe's diameter, material and thickness; the liquid type; and the transducer mounting method (the V-method). The capacitance electrodes (d_2) were in a convenient location near the transducers.

6.2.2 Determining Ultrasonic Propagation Pattern

This experiment's flow meter comprised TUF-2000M and an acrylic pipe with a 100 mm outer diameter and a 3 mm thickness. As mentioned earlier, the first step in identifying

(a) (b)

FIGURE 6.7: a) Flow rate testing [9]. b) Ultrasonic flow meter [9].

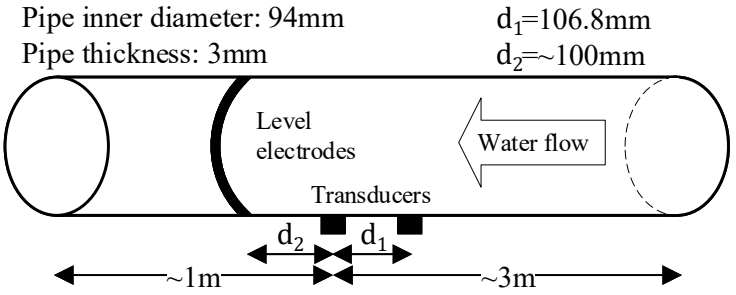

FIGURE 6.8: Flow meter experimental rig setup [9]: a pipe-mounted flexible capacitance-measuring PCB and strategically-positioned ultrasonic transducers.

the propagation path was to calculate the β for a full pipe according to Eq. (6.5), so that $\beta_{rad} = 0.51$ ($d = 106.8mm,\ n = 1,\ h = 94mm$).

The distance between the transducers does not change with the liquid level, and the transducers will always transmit sound at this angle. Hence, the propagation patterns that occur in the pipe at different liquid levels will have the same β as the full pipe. Additionally, a different $\Delta\beta$ value can be calculated for each of the various propagation patterns, and it is possible to predict the actual propagation pattern at that height. This results in the correct flow rate calculation.

The difference between the angles, according to step 2, is shown in Table 6.1, which explains how the propagation path is identified. The highlighted bold text shows the lowest deviation. The propagation pattern is $n = 2$ for these water levels, according to the calculated result. To verify this result using Eq. (6.7), the travel time was calculated (see Table 6.2) and this was contrasted to the travel time measured for the different water heights using the flow meter.

TABLE 6.1: $\Delta\beta$ values for different n and h [9].

Propagation Pattern	**Water Height (mm)**					
	40	***45***	***50***	***55***	***60***	***65***
1	0.420	0.362	0.310	0.263	0.219	0.180
2	**0.080**	**0.027**	**-0.017**	**-0.055**	**-0.088**	**-0.117**
3	-0.088	-0.130	-0.165	-0.194	-0.219	-0.240
4	-0.185	-0.219	-0.246	-0.269	-0.288	-0.305

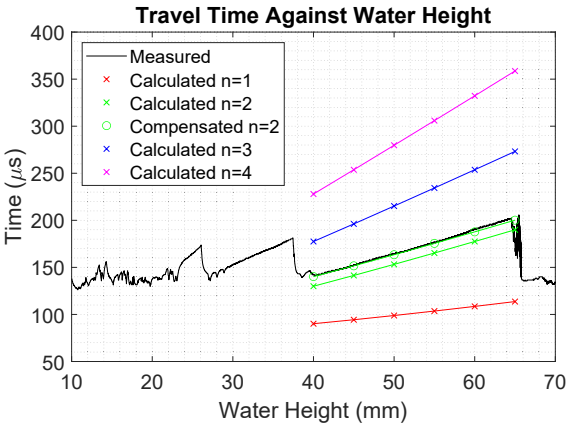

FIGURE 6.9: Measured and calculated times for values of n and h [9].

The computed travel time, according to Eq. (6.7), is shown in Table 6.2; the measured results from the flow meter and the calculated results are shown in Fig. 6.9. According to Fig. 6.9, the measured travel time is slightly higher than the determined reflection pattern, which is $n = 2$. The reason for this difference is the thickness of the transducers (18.9 mm) and the thickness of the pipe (3 mm). The extra time for these distances is 10.245 µs. In Fig. 6.9, this transducer and pipe thickness travel time has been compensated by adding extra time (i.e. +10.245 µs) to the predicted travel time, meaning that the measured travel time matches the predicted pattern.

6.2.3 Liquid Level Measurement using Capacitance

A capacitance sensor with three channels is required to determine the liquid level connected to the environmental, level and liquid electrodes. The capacitance sensor, the Texas Instruments FDC1004 four-channel sensor was used, which has a full range of ±15pF

TABLE 6.2: Calculated travel time (µs) for different n and h [9].

Propagation Pattern	**Water Height (mm)**					
	40	***45***	***50***	***55***	***60***	***65***
1	90.1	94.3	98.8	103.5	108.5	113.6
2	129.9	141.4	153.1	165.2	177.4	189.9
3	177.4	196.1	215.1	234.3	253.7	273.2
4	227.9	253.7	279.7	305.9	332.2	358.6

and high-resolution. An offset capacitance of up to 100pF can be handled by this sensor [200].

In the real world, when measuring capacitance, there can be significant interference from the environment. Hence, electrodes should be properly shielded. A flexible PCB was developed with four layers wrapped around the pipe. To mitigate the parasitic capacitance, the Out-of-Phase method was used. The liquid's potential value was kept at a constant in the excitation phase by using a differential capacitive measurement [201]. There were two shield terminals and three channels used in this method, as shown in Fig. 6.10.

The designed PCB was flexible and had insulation layers. Additionally, it had soldering pads. The middle layers contained the electrodes, as shown in Fig. 6.6a. The same figure shows that the middle Layer 1 held the channels and Shield 1, while the middle Layer 2 contained Shield 2.

The top and bottom sides of the manufactured PCB are shown in Fig. 6.6b. The left side of the PCB (i.e. the top side) shows the three electrodes in the mid-layers. Shorter electrodes are used as liquid and environmental electrodes. The left side of the PCB (i.e. the bottom side) shows the shielding in the mid-layer.

The level testing rig is shown in Fig. 6.6c. The pipe was filled with water and the PCB was wrapped around the pipe. The capacitance values and water height were continually measured. The raw capacitance values are shown in Fig. 6.11. The level and liquid electrodes measured a sudden jump around the sample number of 1,100 when the water filling begins. The jump was caused by the sudden replacement of air with water, which changes the capacitance significantly. The level electrode capacitance value kept increasing since the air inside the pipe is continually replaced with water. This changes the capacitance while the air electrode capacitance values stay nearly constant after the filling begins.

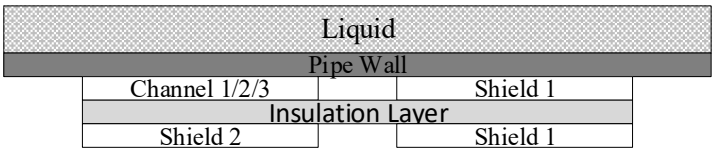

FIGURE 6.10: Sensor layout: Out-of-Phase technique [9].

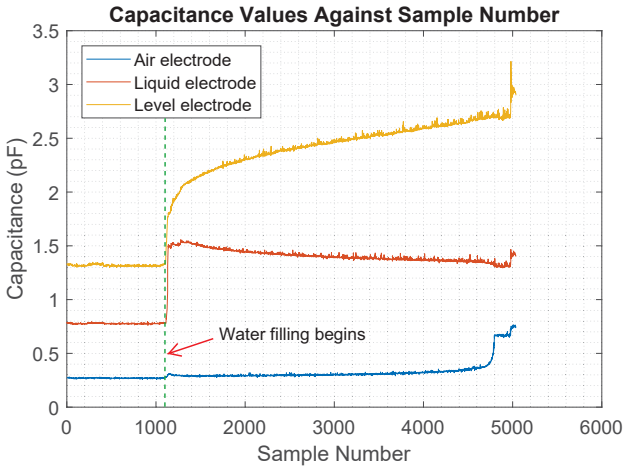

FIGURE 6.11: Raw capacitance values of the three electrodes and the green dashed line shows when water filling begins.

There is a small decrease in the capacitance value measured by the liquid electrode compared to other capacitance changes in the level electrode, although the the cause of this is not fully understood. Similarly to the spike when water filling begins, at around the sample number of 5,000, there was a spike when the pipe became full.

Using Eq. (6.8) and the raw capacitance values, it is possible to calculate the liquid height. The computed liquid height in reference to the ground truth is shown in Fig. 6.14. A window size with a moving average of 100 was used to reduce the outliers and noise. The ratio values from Eq. (6.8) were normalised to be between 0 and 1 (i.e. empty and

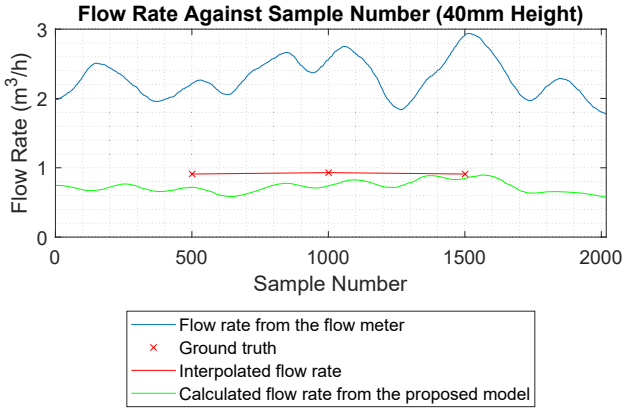

FIGURE 6.12: Flow rates at 40mm water height [9].

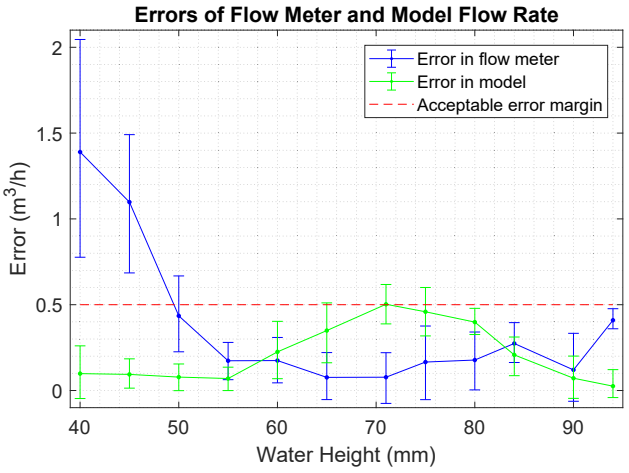

FIGURE 6.13: Errors in both the flow meter readings and the calculated model [9].

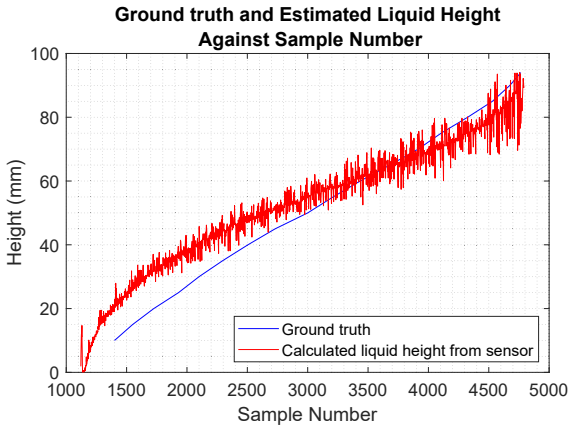

FIGURE 6.14: Estimated liquid height and ground truth [9].

full). The test results showed that the proposed method can measure liquid height with a maximum error of around 10 mm.

6.2.4 Calculate Accurate Flow Rate

Since the liquid height can be determined robustly, as mentioned in the previous section, the propagation pattern can also be identified using the liquid height. The propagation patterns for a given pipe can thus be calculated for different water heights and a mapping can be created between the liquid and propagation patterns.

Testing was conducted at various water levels and, for each water level, a direct reading from the flow meter was taken, as shown by the blue line in Fig. 6.12). The flow rate

from the proposed method (the green line in Fig. 6.12) was also calculated and contrasted to the actual flow meter reading. The ground truth of the flow rate was measured by collecting water and weighing it for a certain amount of time. This weighing of collected water was conducted several times during a test (as indicated by each red "x" in Fig. 6.12) and interpolation was done to obtain the intermediate values (red line in Fig. 6.12).

A summary of the different test results for various liquid levels is provided in Fig. 6.13. The graph shows the error compared with the ground truth and the top and bottom whiskers represent $q_3 + w \times (q_3 - q_1)$ and $q_1 - w \times (q_3 - q_1)$, where q_1 and q_3 are the 25^{th} and 75^{th} percentiles and $w = 1$. The mean error value is shown by the middle value in the whiskers. According to the error bars, the flow meter performs poorly when the flow is low. Additionally, there is a wide distribution in the flow meter errors when the flow is low, unlike in the model. The acceptable error margin for this application is less than 0.5 m^3/h. The flow meter error is around 1.4 m^3/h when the liquid level is at 40 mm, while the proposed model produced an error of less than 0.1 m^3/h, indicating an error reduction of around 92%. Due to the pump's practical limitations, it was not feasible to create a flow with a height of less than 40 mm.

From the test results, it is possible to observe that the flow meter performs poorly when the liquid level is low. Conversely, when the flow is low, the suggested model performs within the required error margin. The proposed model showed a slightly higher error rate of between 60 mm and 80 mm. However, the model's mean value was within the acceptable maximum error (0.5 m^3/h). It is possible to further reduce the error to under to 0.2 m^3/h for all water levels by switching between the model-based flow measurement and the flow meter-based measurement when the water level is within certain predefined liquid height ranges.

6.3 Conclusions

This chapter presented an easily extensible sensor fusion approach to improving a transit time flow meter's accuracy for the partial flows common to the feed pipes for GSS. Flow rate measurement in a partially filled pipe is challenging. Common transit time ultrasonic

flow meters perform poorly when a pipe is partially filled and the error increases when the water level decreases. The novel method in this chapter extends transit time ultrasonic flowmeters by measuring the liquid level using an inexpensive capacitance-based level sensor. It proposed a methodology to identify the different propagation patterns in various liquid levels and has proven its accuracy in several different scenarios. It accurately calculated the flow rate using determined reflection patterns as proposed equations when the pipe was filled partially. The experiments conducted showed that the method reduces the error from 1.4 m^3/h to 0.5 m^3/h in low water levels, and that the model performs within the required error margin for all water levels.

Chapter 7

Radial Slicing and Path Planning for 3D Printing

Printing the GSS using the developed bespoke printer occurs around a rotating column using robot arms. In contrast, printing the GSS using the traditional horizontal printing method would require an unreasonable amount of support material. Additionally, it would introduce stepwise bumps on the spiral surface, which are undesirable since they would change the surface roughness, affecting the slurry's separation. Therefore, printing should be conducted perpendicular to the axis of the GSS. However, unlike in horizontal algorithms, there is no single vertical or horizontal plane on which slicing can occur. Hence, printing should occur parallel to the GSS central axis on concentric cylindrical surfaces. Ideally, this printing should incorporate the limitations of the robot. The first section of this chapter presents a radial slicing algorithm that can be used to achieve this goal and introduces manipulability as a "printability" measure.

Using the developed slicing algorithm, it was possible to generate trajectories on which GSS could be printed by moving the extrusion head in a spiral shape. However, there are multiple possible options for progressing the print head towards the outer edge of the GSS. Therefore, after trajectory generation an optimal path planning method was proposed to move the extrusion head outwards using a combined cost function to print the spiral, which will improve the overall robot manipulability.

7.1 Methodology

An overview of the approach is shown in Fig. 7.1. Firstly, the 3D model is sliced using the proposed slicing algorithm and tool trajectories are generated. Secondly, the radial path planning for a robot is optimised by means of print space sampling. Finally, using the trajectories generated, the object is 3D printed.

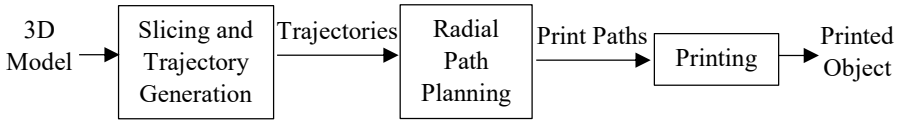

FIGURE 7.1: Overview of the proposed radial slicing and robot path planning approach for 3D printing.

7.1.1 Radial Slicing and Trajectory Generation

7.1.1.1 STL Files

STL files are composed of a list of triangle facet data that describes the surface of the object. Three vertices and a unit normal are used to uniquely identify a facet. Three coordinates in $\mathbb{R}^3$ have been used to identify each vertex and each facet identifies the boundary between the interior of the object and the exterior [139]. The triangles in the STL files satisfy the following conditions: (i) every edge is common to at least two triangles; (ii) any number of triangles can share a vertex; (iii) every triangle has at least a single point in common with another triangle; (iv) if there is a common vertex with the second triangle, it is also a vertex of the second triangle; (v) triangles do not intersect with the interior of any other triangles [202].

7.1.1.2 Ray Line Generation

A top-down view of the spiral is shown in Fig 7.2. Using Eq. (7.1), the number of cylinders, N, can be calculated with user-defined parameters, such as minimum radius, r_s, and maximum radius, r_e, to ascertain where the slicing should occur. Additionally, the

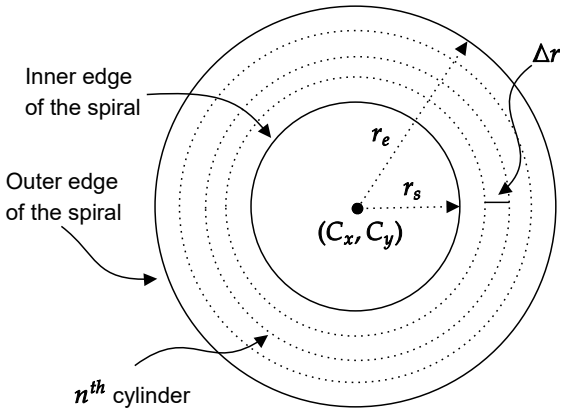

FIGURE 7.2: Generated cylinders where slicing occurs [10].

gap between concentric cylinders, Δr, is also user-defined and the centre of the spiral is $(C_x,\ C_y)$.

$$N\ =\ (r_e\ -\ r_s)/\Delta r \tag{7.1}$$

The length along the circumference of the cylinder, ΔC, is a user-defined value. A point in the n^{th} cylinder, (x_0, y_0, z), is defined in Eq. (7.2) and Eq. (7.3), where z is an arbitrary constant value. The total number of points around the circumference, K, that are equally spaced by ΔC, is calculated using Eq. (7.5). For each cylinder, a set of vertical lines, $L_{n,k}$, parallel to the axis of the spiral going through the point, (x_k, y_k), is calculated as per Eq. (7.9) for the n^{th} cylinder using the parameters defined in Eq. (7.7) and Eq. (7.8). These are shown in Fig. 7.3, in which $n = 1 \ldots N$, and for the k^{th} point, where $k = 1 \ldots K$

$$x_0 = C_x + r_s + n \cdot \Delta r \tag{7.2}$$

$$y_0 = C_y \tag{7.3}$$

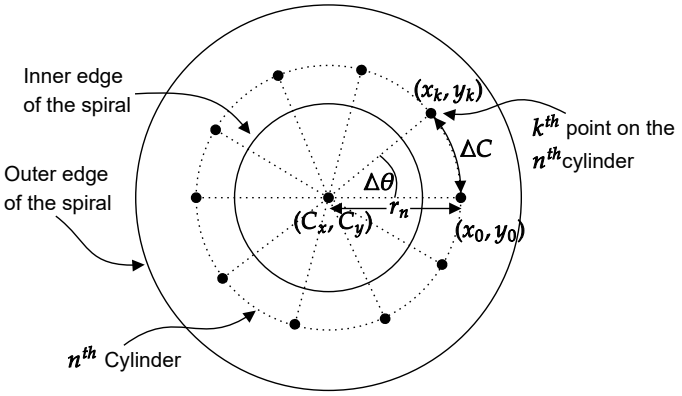

FIGURE 7.3: Generated points for ray lines [10].

$$r_n = |x_0 - C_x| \tag{7.4}$$

$$K = \lfloor 2 \cdot \pi \cdot r_n / \Delta C \rfloor \tag{7.5}$$

$$\Delta\theta = k \cdot \Delta C / r_n \tag{7.6}$$

$$x_k = (x_0 - C_x) \cdot \cos(\Delta\theta) + (y_0 - C_y) \cdot \sin(\Delta\theta) + C_x \tag{7.7}$$

$$y_k = -(x_0 - C_x) \cdot \sin(\Delta\theta) + (y_0 - C_y) \cdot \cos(\Delta\theta) + C_y \tag{7.8}$$

$$L_{n,k} =< x_k, y_k, z > +t < 0, 0, 1 > where\ t \in \mathbb{R} \tag{7.9}$$

7.1.1.3 Calculation of Intersections Between Rays and Model

The intersection points between the STL model and each ray line, $L_{n,k}$, was calculated. The model was composed of triangles and calculating the intersection points between the line and the triangles gave the intersection locations between the model and a line. A heuristic method was used to improve efficiency. User-defined thresholds, (T_x and T_y), were used to define a bounding box, as shown in Eq. (7.10) to Eq. (7.13). When calculating the line–model intersection, the search was limited to only this bounding box.

$$x^{+} = x_k + T_x \tag{7.10}$$

$$x^{-} = x_k - T_x \tag{7.11}$$

$$y^{+} = y_k + T_y \tag{7.12}$$

$$y^{-} = y_k - T_y \tag{7.13}$$

7.1.1.4 Generation of Intermediate Points

After identifying the intersection points between the mode and the lines, the points were sorted by the Z-height (i.e. along the Z-axis). This step employed the user-defined layer height, Δh, to create a set of intermediate points. There were many intersection points since the model was closed and the ray lines penetrated the triangles. Hence, a point with the lowest Z value would be on the bottom surface and the next point would be at the top surface. During the printing, this intermediate space would be filled (i.e. the infill). For mechanical design reasons, a solid infill is desirable. Under this assumption, the intermediate points are computed as follows. The bottom and top points' X-, Y- and Z-coordinates are connoted by (X_b, Y_b, Z_b) and (X_t, Y_t, Z_t), respectively. The number of intermediate points is m and depends on the thickness of the trough. Let the i^{th} intermediate point, P_i, and the X, Y and Z values of that intermediate point be $(P_{i,x}, P_{i,y}, P_{i,z})$, as calculated in Eq. (7.15) to Eq. (7.17). The X and Y values in the intermediate points are equal to the X and Y values in the bottom and top points, as shown in Eq. (7.15) and Eq. (7.16).

$$m = \lfloor (Z_t - Z_b)/\Delta h \rfloor \tag{7.14}$$

$$P_{i,x} = X_b = X_t \tag{7.15}$$

$$P_{i,y} = Y_b = Y_t \tag{7.16}$$

$$P_{i,z} = Z_b + i \cdot \Delta h \; where \; i = 1 \ldots m \tag{7.17}$$

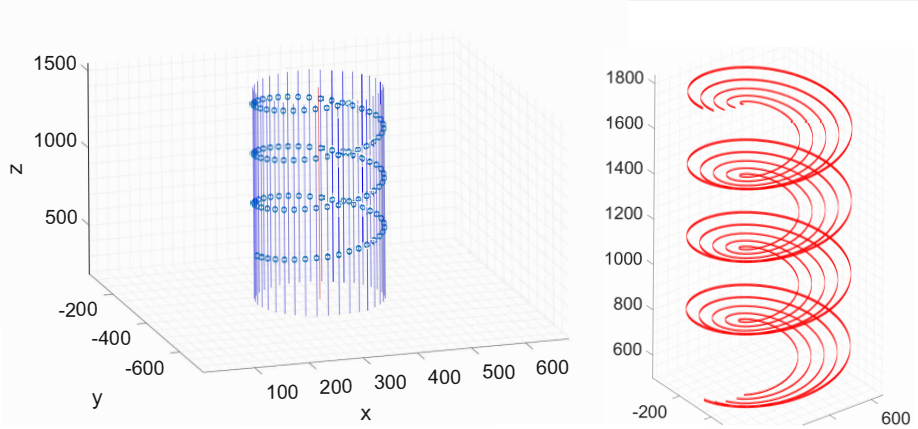

(a) (b)

FIGURE 7.4: a) Lines and intermediate points in a single cylinder [10]. b) Closer view of the intermediate points [10].

These intermediate points are shown in Fig 7.4a in the overall view of a single cylinder; a closer view of the same data is provided in Fig. 7.4b, such that the individual points are clear. These calculations were applied to all cylinders and the results are shown in Fig 7.5.

7.1.1.5 Trajectory Creation

After generating the set of points, S, that included both the top and bottom points, as well as the intermediate points for the complete cylinder, it was necessary to generate a tooltip trajectory, which would map the points followed by the robot tooltip. Using the points that were created for each cylinder, a set of trajectories were produced. To achieve

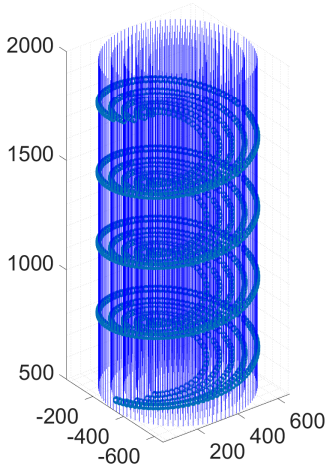

FIGURE 7.5: Lines and intermediate points of all cylindrical slices [10].

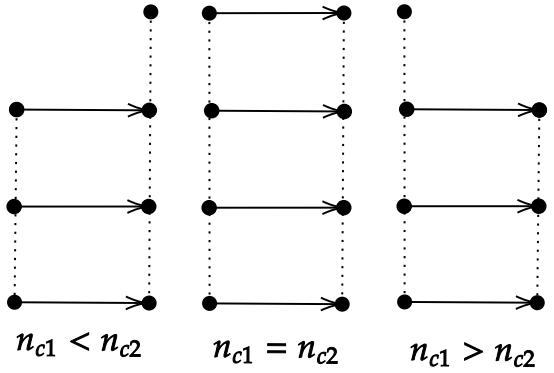

FIGURE 7.6: Different methods of connecting clusters [10].

this, the lowest cluster of points were first identified for each cylinder. The point with the lowest Z value, M, was selected. Consider X and Y values of M are M_x and M_y. The set of points, N that has the same X and Y values (i.e. they are vertically above M as calculated in (7.18)), are then sorted according to their Z values. Consider a point p_i that has a lower Z value, z_i to p_{i+1}. The lowest cluster of points, L_1, which lie within the model are identified with (7.19).

$$N = \{p \mid x = M_x, y = M_y, p \in S\} \tag{7.18}$$

$$L_1 = \{p \mid (z_{i+1} - z_i) < \Delta h\} \tag{7.19}$$

$$N = N - L_1 \tag{7.20}$$

The difference between the Z values of p_{i+1} and p_i is compared with Δh to create the set L_1. It is added to the set if it is less than Δh. The cluster is removed from the set N, as shown in Eq. (7.20), once the condition is no longer satisfied. The next cluster is created by applying the same method to the remaining points. This process continues until no points remain, $N = \emptyset$.

The way connections were made between the points in each cluster or how the sequences were created depending on the number of points in each cluster is shown in Fig. 7.6. An arrow shows the tooltip travel direction and n_{c1} and n_{c2} represent the number of points in each cluster. After connecting this cluster, the same process was continued for the clusters

in sequence—$(L_1, L_2, L_3, \cdots)$—until $N = \emptyset$. The trajectories generated for a single spiral are shown in Fig 7.7a and those generated for multiple cylinders are shown in Fig 7.7b.

7.1.1.6 Simulation of Printing Process

Fig 7.8a shows the developed simulation environment in Matlab, adhering to the real physical dimensions of the printer. Denavit–Hartenberg (DH) parameters were used to represent the industrial robot's dimensions (ABB IRB 120). The robotics toolbox developed by Peter Corke was used to simulate the robot [203].

7.1.1.7 Robot Inverse Kinematics and Manipulability

The robot tooltip should track and follow the waypoints according to the generated Cartesian trajectories. To achieve this, it was necessary to determine the joint configurations or each of the end-effector poses along the different trajectories. This process is known as Inverse Kinematics (IK). The solution to the IK problem can be obtained numerically or analytically.

A model of the robot can be created, which defines the relationship between the various joints, and then this can be used to solve for the joint variables. However, when there is a

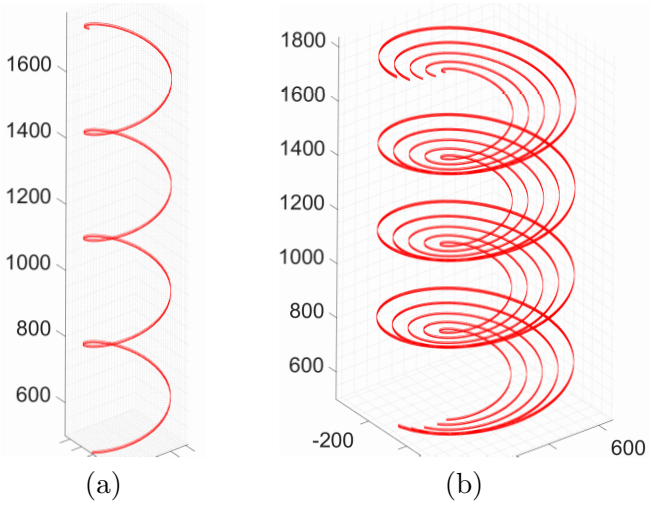

FIGURE 7.7: The calculated tool trajectories [10]: a) One trajectory from in a single cylindrical range; b) Trajectories in multiple cylinders.

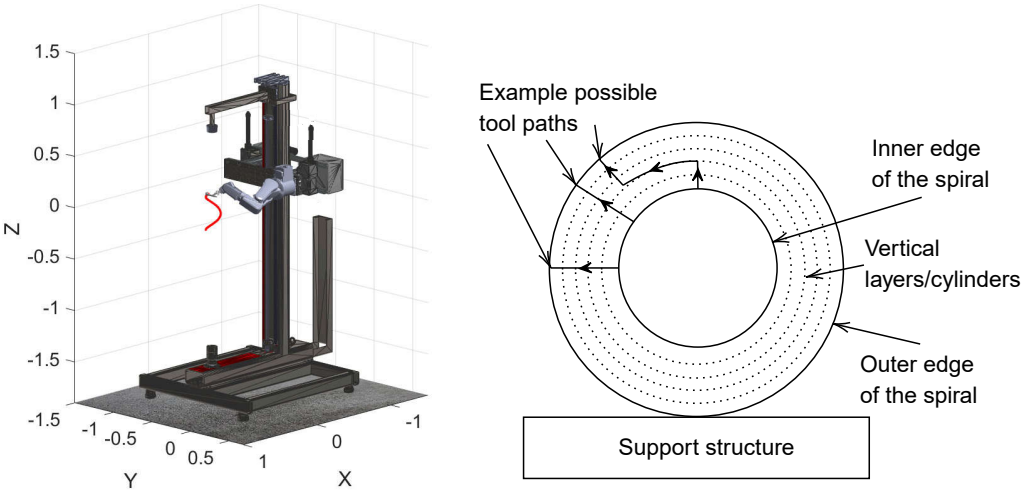

(a) (b)

FIGURE 7.8: a) Simulation environment and robot model [10]. b) Three examples of printhead movement paths [11].

high degree of freedom in a robot system, obtaining an analytical solution is exceedingly difficult or sometimes impossible [204, 205]. There are six joints in each of the industrial robots that are independently mounted on vertical linear rails for this application, and so, predictably, it was difficult to find an analytical solution [206]. Hence, a numerical solution was employed. For the numerical solution, Forward Kinematics (FK) was first used to determine the end-effector location. FK mapped each joint configuration to an end-effector Cartesian pose (i.e. a 3D point and orientation) [207]. It was possible to determine the end-effector pose using FK, $K(q)$. Then, given the desired pose, ξ^*, which is a waypoint in a printing trajectory, the general problem (7.21) could be formulated as an optimisation problem, and the error between the end-effector pose and desired pose could be minimised, as shown in (7.22).

$$q = K^{-1}(\xi^*) \tag{7.21}$$

$$q^* = \underset{q}{\operatorname{argmin}} \, \| K(q) \ominus \xi^* \| \tag{7.22}$$

A robot arm's ability to move easily in any direction or its dexterity of a robot arm is referred to as its manipulability [155]. Manipulability is a scalar measure on which the

higher the score, the better. For each location along the tool path, this value can be calculated. For a given location and a manipulator, this chapter evaluates how to use this measure to calculate the ease with which a given tool path may be executed for 3D printing. The manipulability measure depends on the Jacobian matrix of the manipulator. The Jacobian matrix maps joint velocities, $\dot{q}$, to end-effector Cartesian velocity, v, as shown in Eq (7.23), wherein q is the joint angles [155]. For this research, Yoshikawa's manipulability measure [208] was used, as demonstrated in Eq. (7.24).

$$\dot{q} = J(q)^{-1}v \tag{7.23}$$

$$m = \sqrt{det\,(JJ^T)} \tag{7.24}$$

7.1.2 Radial Path Planning

The previously developed slicing algorithm created trajectories for printing GSS by moving a printhead in the shape of the spiral. However, it is necessary to identify the optimal path on which to move the extrusion head radially outwards by considering a combined cost function to achieve a successful print and improve the overall manipulability.

In the printing process, the printhead starts to deposit the first layer of melted extruded material onto the rotating column and then progressively adds layer upon layer, expanding the printing process radially outwards. The printing commences at the bottom and ends at the top and, in each layer, there are multiple trajectories. The robot arm moves along a rail from the bottom to the top in a vertical line and the column at the centre rotates to achieve the helical shape. A top-down view of the printer is shown in Fig. 7.8b and the dashed lines depict these concentric vertical layers or cylinders. This section of the chapter addresses the path that should be used when moving outwards from the central column. To cover a large volume of the print space using relatively small industrial robot arms, the robot arm's base location changes and, along with it, the dexterity value of the robot arm constantly changes as well. This has a major impact on print quality and can cause print failures. A few examples of printhead paths are shown in Fig. 7.8b and, although,

theoretically, there is a large number of possible paths that can be generated, some of them are infeasible and this research addresses the problem of identifying the optimal path.

7.1.2.1 Proposed Cost Function

The objective of this research is to identify the best path along which to move the printhead from the closest to the central column, $i = 1$, and then to the last cylinder, $i = n$, where n is the total number of cylinders. A cost function was proposed for path planning, which was a weighted combination of three cost values: inverse manipulability, $C_m(p)$; Euclidean distance error, $C_d(p)$; and roll-pitch-yaw rotation error, $C_r(p)$, where p is a provided sample location and p_c is the true location in which the printhead ends up when the printer attempts to move it to p. To represent p, the coordinates can be used as (i, k), where i is the cylinder number and k is the k^{th} location in that cylinder. The weight of the distance error, w_d, the manipulability, w_m, and the rotation error, w_r, are used in the cost function, as shown in Eq. (7.28).

$$C_m(p) = 1 - m(p) \tag{7.25}$$

$$C_d(p) = d(p_c, p) \tag{7.26}$$

$$C_r(p) = d_{roll}(p_c, p) + d_{pitch}(p_c, p) + d_{yaw}(p_c, p) \tag{7.27}$$

$$C(p) \;=\; w_m \cdot C_m(p) + w_d \cdot C_d(p) + w_r \cdot C_r(p) \tag{7.28}$$

The manipulability value was between 0 and 1 (where a higher value is better) and this value was converted to a cost, as shown in Eq. (7.25). The Euclidean distance between p and p_c is calculated by the function $d(p_c, p)$ in Eq. (7.26). The absolute values of roll, pitch and yaw angle difference between the p and p_c were calculated by the functions $d_{roll}(p_c, p)$, $d_{pitch}(p_c, p)$ and $d_{yaw}(p_c, p)$, respectively. Improving the rotation error and distance error will improve the print accuracy of the spiral's original shape. Improving the manipulability and the dexterity to avoid singularities while printing will help future research to print sensors inline. Depending on the task objectives, such as the need to

balance the manipulability versus the accuracy, it is possible to tune the weight values to appropriately bias the cost function.

7.1.2.2 Sampling the Print Space

It was necessary to sample the print space to calculate the cost values before path planning. Fig. 7.9a shows an example of a sampled area in which the robot arm can move easily without getting into any poses that hinder its ability to reach. The number of samples and the granularity of the samples depend on the requirements of the user. These generated sample locations are shown in Fig. 7.9b and the user-defined parameters used to create these sample locations are shown in Fig. 7.9a. The distance between two consecutive sample locations in a single layer is Δc and the distance between consecutive layers is Δr. Since it was assumed that the printhead was extruding material in the column's direction, the printhead orientation was set as constant throughout all locations. The robot arm was moved to each of these sample locations using the IK solver and the different cost values mentioned earlier were calculated after creating the sample locations.

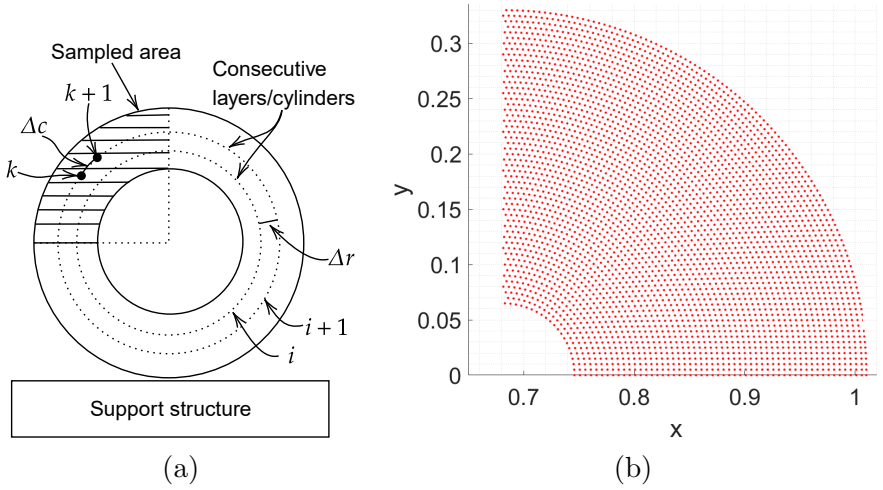

(a) (b)

FIGURE 7.9: Sampling print space [11]: a) Sampled area; b) Generated sampling points.

7.1.2.3 Path Planning

A path should be determined to navigate from one cylinder to another after computing the cost values for each sample point. The minimum cost sample point, $p_{min,i}$, was selected by Eq. (7.29) for each of the cylinders, i:

$$p_{min,i} = \underset{k}{\operatorname{argmin}}\ C(i,k) \tag{7.29}$$

$$P = [p_{min,1}, p_{min,2}, \ldots, p_{min,n}] \tag{7.30}$$

The sequence of these points from $p_{min,1}$ to $p_{min,n}$ gives the optimal path, as shown in Eq. (7.30). This path was followed during the full spiral printing.

7.2 Experimental Results

7.2.1 Cylindrical Slicing Results

Fine-grained parameters were selected for the simulation and those were $\Delta r = 5\ mm$, $\Delta C = 5\ mm$, $\Delta h = 2\ mm$, $r_{end} = 65\ mm$, $r_{start} = 330\ mm$ and the full height of the spiral was $1.3\ m$. All points were saved in the Polygon File Format (PLY) file format after slicing to visualise and the trajectories were saved as Matlab data files for simulation purposes. There were around 250,000 vertices in the final sliced output. All the waypoints in the trajectories were also saved in the PLY file. The waypoints in the printing trajectories are shown in Fig 7.10a, while Fig. 7.10b depicts these points overlaid with the STL model of the spiral. The figure shows that the trajectories generated preserve the original contour and shape of the spiral. Several other helical-shaped objects (other than a GSS) have been sliced to test the presented method; examples include a uniform solid coil representing a suspension spring used in large machinery (shown in Fig. 7.11a), and an arbitrary wavy cross-section (shown in Fig. 7.11c). The slicing results are shown in Fig. 7.11b and Fig. 7.11d. The STL model overlaid with the slicing output, indicate an accurate shape approximation, as depicted in Fig 7.11a. The trajectories generated for the robot arm to

follow are provided in Fig. 7.11b. Only every 5^{th} slicing cylinder and every 5^{th} trajectory in a given cylinder (i.e. 4% of all trajectories) are shown since a plot of all trajectories would result in the lines being too close for visualisation. These trajectories also conformed to the original shape of the object. An arbitrary cross-sectional helical shape is shown in Fig 7.11c, which is significantly different from a GSS. A closer view of the intersection points is given in Fig 7.12a and Fig. 7.11d shows the sampled trajectories.

The GSS was sliced using the conventional Z-direction slicing and the difference between the two slicing methods was noted. A large number of support structures were required, as shown in Fig. 7.12b, because of the print direction. The brown indicates the spiral that is to be printed and the green structures show the additional support material. Hence, if the traditional Z-directional slicing and printing were used, all those printed green colour support structures would need to be removed to obtain the final shape. Printing these support structures (the green structures) alone takes significant time in contrast to printing the required shape (the brown areas). Additionally, removing the support structures is a difficult process after printing and it can reduce the smoothness of the surface, which will adversely impact the spiral's performance. Further, it may increase the cost of printing due to the additional material required. The proposed radial slicing and printing eliminates this problem because the printing process occurs perpendicular to the Z-axis.

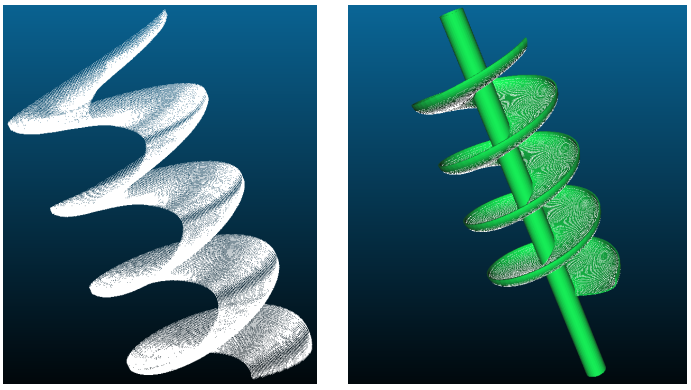

(a) (b)

FIGURE 7.10: Visualisation of exported PLY files [10]: a) Exported PLY file from the slicing algorithm. b) Exported PLY file (white) overlaid with original STL file (green).

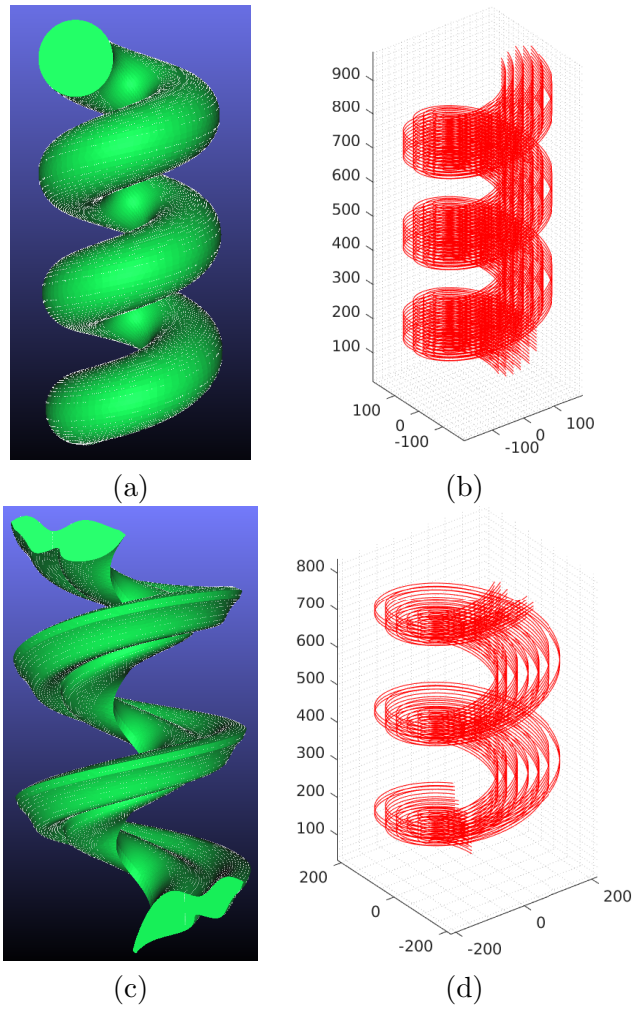

FIGURE 7.11: Slicing outputs [10]: a) Solid coil (green) overlaid with the slicing output (white); b) Generated trajectories showing only every 5^{th} slicing cylinder and every 5^{th} trajectory in a cylinder (i.e. 4% of all trajectories); c) Helical spiral with an arbitrary cross-section (green) overlaid with intersection points (white); d) Generated trajectories showing only every 5^{th} slicing cylinder and every 5^{th} trajectory in a cylinder (i.e. 4% of all trajectories).

7.2.2 Manipulability Simulation for Robot Printing

The previously mentioned simulation environment has been used to simulate the printing according to the created tool paths. The printing of the first trajectory is shown in Fig 7.8a. The manipulability measure was calculated for each location through which the print head moved during the printing process. These manipulability values were saved to a file and analysed using CloudCompare software [209]. This allowed for the identification

of potential print faults and for the manipulability to be visualised at the various locations on the spiral, as shown in Fig. 7.13.

A manipulability map will enable the better planning of robot arm motions to increase their ability and the likelihood that the sensors will be printed accurately and easily. The robot arm can have many poses and locations during the execution of a printing trajectory. Because of its limited manipulability and depending on the desired tool pose, the output of the print might change significantly or only vary slightly. To print each cylinder, transitioning from one cylinder to the next adjacent cylindrical layer (i.e. a one "layer height" radius increase) can be achieved in various ways. Two such methods are shown in Fig 7.14. In Case 1, the extrusion head moves from the innermost to the outermost cylinder at an angle of 45°. Conversely, in Case 2, few inner cylinders (indexes 1-11) were printed in the $-X$ direction. To print the rest of the cylinders, the extrusion head was rotated 45°, as illustrated in Fig. 7.14b.

The results of these two cases are shown in Fig 7.13. The Case 1 results are shown in Fig 7.13a and the Case 2 results are given in Fig. 7.13b; the histograms are provided in Fig. 7.15b and Fig. 7.15a reveals the manipulability values. The intensity of the colours in the aforementioned figures represent the manipulability values. Fig 7.13a shows the Case 1 results, revealing that the robotic arm was not able to print 3% of the 52 tool paths in the middle because of an inability to find joint trajectories for the arm that would place the end-effector at the required points along the trajectory. Fig. 7.13c and Fig. 7.13d show

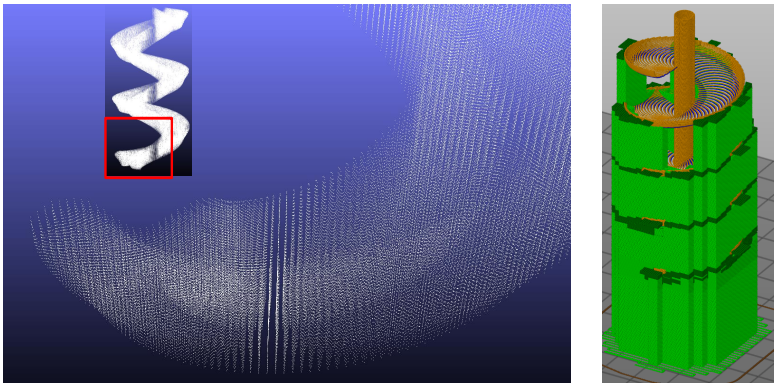

(a) (b)

FIGURE 7.12: a) Close-up view of the intersection points at the bottom of the spiral (inset image: macro view) [10]. b) Result from conventional Z-direction slicing showing the support material (green) [10].

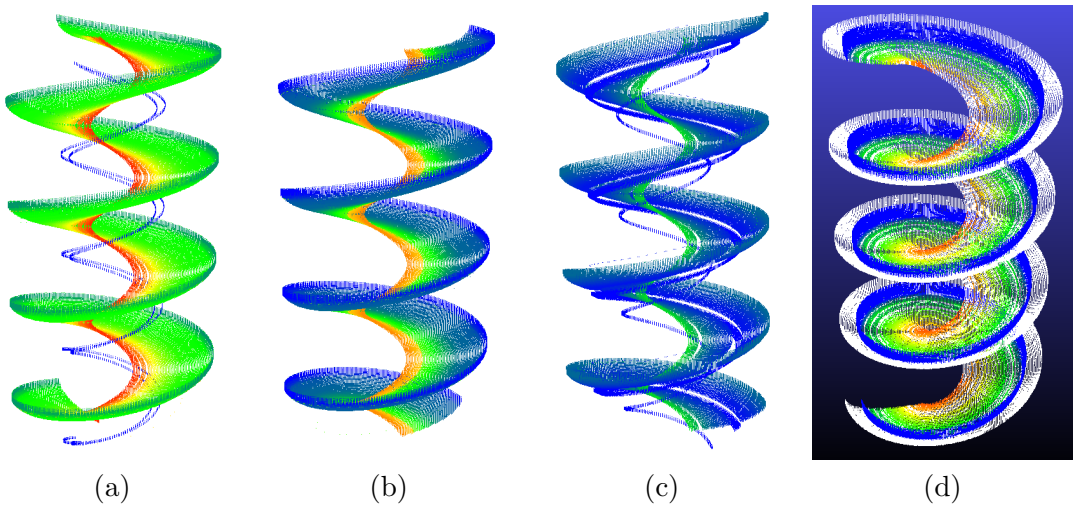

(a) (b) (c) (d)

FIGURE 7.13: Examples of successful and failed prints [10]: a) Failed print - case 1; b) Successful print - case 2; c) Failed 90° angle print; d) Failed 0° angle print (coloured points) overlaid with trajectory waypoints (white points) showing a malformed failed print; The colours represent the amount of manipulability where red, yellow, green and blue shows the transition from high to low manipulability values.

a few failed print scenarios for different cases. A malformed print is shown in Fig 7.13d, wherein the white dots represent the waypoints of the tool path the printer should follow, and the coloured points represent the printed spiral. The reason for this failure is that the robot arm was not able to move to the furthest layers. Conversely, a successful print from Case 2 is shown in Fig. 7.13b, wherein the overlay of the trajectory output from the slicer appears to be accurate. Case 2 was determined by the heuristic analysis of observations from other prints with similar shapes. When the manipulability value reached near-zero (depicted by the blue colour in the histogram), the arm's dexterity or the ability to print with the robotic arm was low. Therefore, this figure's depiction of manipulability is useful for identifying and predicting the possible print output (i.e. how likely it is to succeed) and the dexterity of the robotic manipulator as it moves through the tool path . This is important for future research, in which sensor placement will need to be simultaneously considered along with the printing process.

The radial manipulability values were plotted to understand the relationship between print success and robot manipulability, as shown in Fig. 7.13 and Fig. 7.16. There were two sudden drops observable in manipulability along the radius, that correlate with the two failed areas in Fig. 7.13a. For the successful print case in Fig. 7.13b, there was no

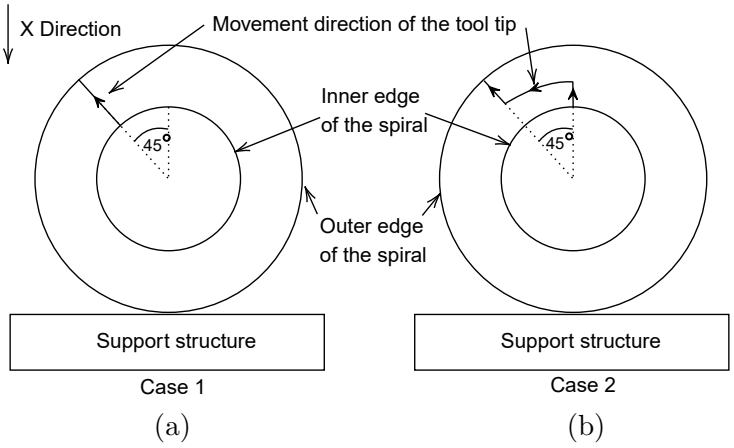

FIGURE 7.14: Two examples of print head movements [10]: a) Moving printhead directly at a 45° angle; b) Moving printhead partially at a 0° angle and then 45° angle.

sudden change in manipulability, apart from a change in the print direction, as mentioned earlier and revealed by Case 2 in Fig. 7.14. Like in Case (a), there were two sudden drops in manipulability value in Case (c). However, the severity of the second drop in manipulability value (down to almost zero) effectively removed the robot arm's ability to move within a single degree of freedom. For Case (d), in Fig. 7.16, it can be seen that manipulability reached zero towards the outer cylindrical layers, indicating that the robot arm had lost a degree of freedom and resulting in the misshapen print depicted in Fig. 7.13d.

To consider manipulability as a printability measure, the likelihood of the success of the

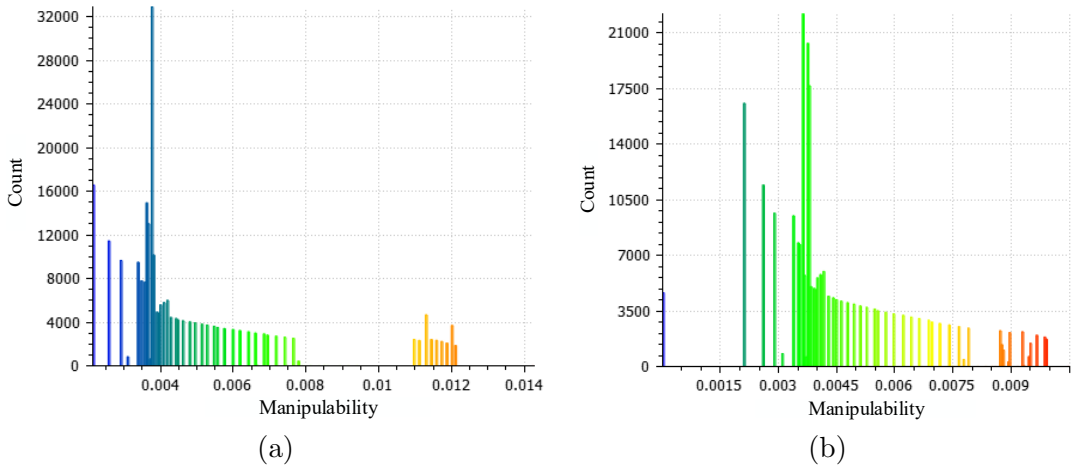

FIGURE 7.15: a) Manipulability histogram of successful print [10]. b) Manipulability histogram of failed print [10].

print should be determined using the local manipulability rather than the overall average manipulability during the printing. Even though the robot arm exhibits high manipulability throughout most of the trajectory, if a situation arises in which the robot arm reaches near-zero manipulability, it will cause the print to fail. This is because, with a near-zero manipulability measure, the robot arm is near a singularity and is incapable of moving in one or more directions (X, Y or Z) or orientations (roll, pitch or yaw). Fig. 7.16 shows Case (d), which highlights this effect whereby the arm becomes unable to move outwards, resulting in a malformed and failed print. Table 7.1 shows this more clearly, including the average cross-section of manipulability value for each print. With the second-highest average manipulability, Case (b) was the most successful print. Even though Case (d) had a higher average manipulability than Case (b), towards the end of the print trajectory, it had a near-singular configuration that caused its failure, reinforcing the need to use a localised rather than global average manipulability measure.

7.2.3 Radial Path Planning Results

The same simulation environment shown in Fig 7.8a was used to test this path planning method. The outputs of the printing simulation were saved as a point cloud in which each

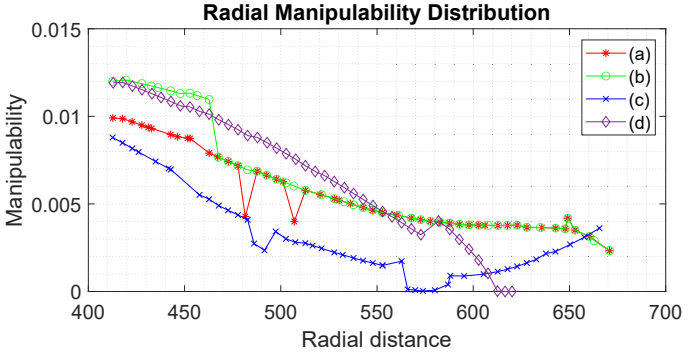

FIGURE 7.16: Radial manipulability distribution in different spiral prints [10].

TABLE 7.1: Average cross-section manipulability in spiral prints [10].

Case	Average Manipulability
(a)	0.0057
(b)	0.0061
(c)	0.0031
(d)	0.0068

location had a manipulability value to assist in visualising the print easily. The sampling was conducted for all the experiments using the parameter values of $\Delta c = 5mm$ and $\Delta r = 5mm$.

7.2.3.1 Results Without Path Planning

This section shows the different failed prints that occurred without optimal path planning. The colour of the print shows the manipulability value and the blue shades represent the problematic values near zero. The next increments are shaded green, yellow and, finally, red, as the values increase away from zero. Since higher values of manipulability are more desirable, green, yellow, red indicate values that change from satisfactory to optimal. The simulated printing results are shown in Fig. 7.17. There were minor failures in a few trajectories, such as in Fig. 7.17c, and there were major failures, such as in Fig. 7.17b. This latter figure shows a trend relating the level of failure to the low level of manipulability values experienced by the robot arm. The use of a trial-and-error approach may uncover a path that is capable of printing without failures, but this is a non-systematic and time-consuming approach.

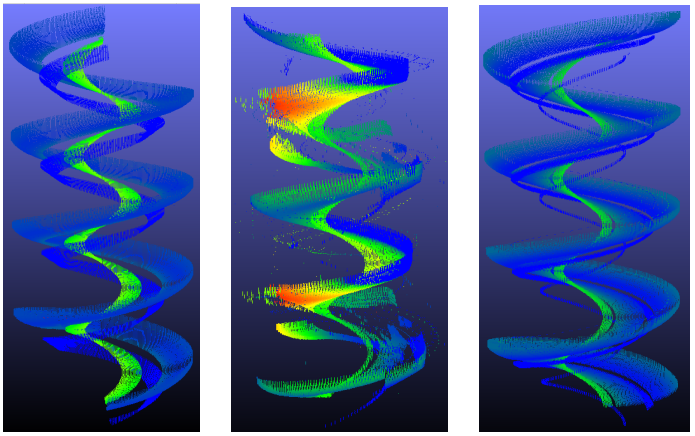

(a) (b) (c)

FIGURE 7.17: Example of failed prints from a naïve trial-and-error approach that did not use path planning [11]. The colours represent the amount of manipulability where red, yellow, green and blue shows the transition from high to low manipulability values.

7.2.3.2 Results With Path Planning

The mesh plots of the various cost values are shown in Fig. 7.18. The manipulability values were converted to cost values as per Eq. (7.25). The weight values of $w_m = w_d = 1$ and $w_r = 0.01$ were selected for the combined cost function in Eq. (7.28). The sampled locations that formed an arc are shown in Fig. 7.9b. A scattered interpolation method was used to calculate unknown values using a 400-by-400 square grid and to generate the mesh plots. A contour plot with the same mesh plot shown in 7.18d and with a generated path is depicted in Fig. 7.18e. A path deviation analysis was conducted three times to choose the weights (w_m, w_d and w_r). In each test, only one weight was changed at a time from 0 to 1 in 0.125 increments, as in Fig. 7.19. Three outcomes were considered when choosing the weights: path deviation, length of the path and back-and-forth rotations since these would reduce the print times. Low weights were selected for the rotation error because higher weights caused a greater path deviation according to the sensitivity analysis. Similarly, a high weight value was selected for manipulability to reduce the path deviation. There was an unexpected observation that, according to Fig. 7.19, when the distance weight changes, the rotation angle difference seems low and nearly consistent. The reason for this was that the peak values in Fig. 7.18a and Fig. 7.18b were at approximately the same location. Hence, the weight change in the distance error did not significantly affect the path's deviation, as such a consequence was already avoided by considering the manipulability cost value.

The cost values and the path deviation behaviour are unique to the kinematic model of the robot arm and the print dimensions. Therefore, different configurations will produce different results. However, the same method can be used for any printing process, provided that the manipulability can be calculated.

A successful print that was printed using the computed path is shown in Fig. 7.18f. When this print was considered alongside the other failed prints observed earlier in Fig. 7.17, it became apparent that there were no print errors and, overall, the spiral print was completely green. This indicates that the manipulability values were higher and were not close to zero (i.e. awkward poses), as was the case in the failed prints shown in Fig. 7.17.

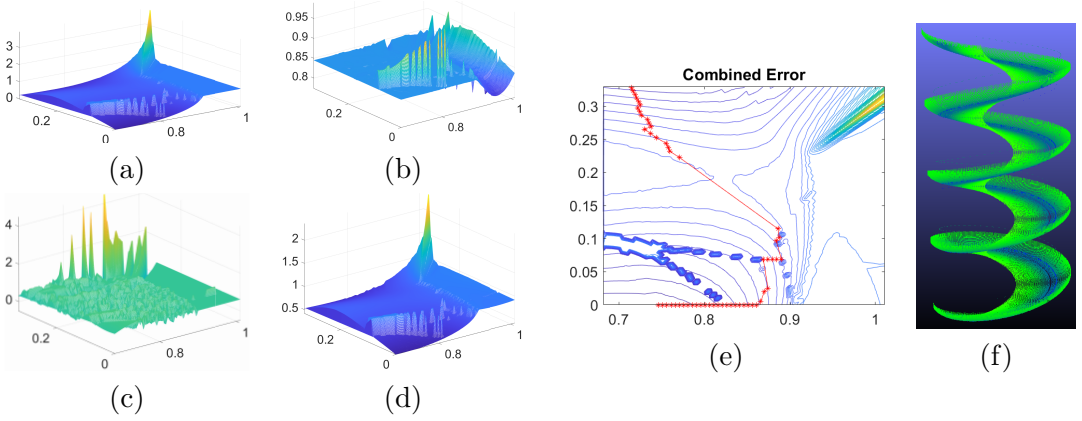

FIGURE 7.18: Mesh plots [11]: a) Inverse manipulability; b) Distance error; c) Rotation error; d) Combined error; e) Combined error contour plot with the generated path; (f) Successful print with the generated path.

7.3 Discussion

This chapter presented a novel radial slicing and a path planning algorithms that can be used to slice objects in the radial direction. The majority of the slicing algorithms developed so far in the literature perform vertical Z-direction slicing [150–152]. Since an excessive amount of support material is necessary, as shown in Fig. 7.12b, such Z-slicing is undesirable in this application. This excess material will cause significant waste of material and time and the removal of supports might damage the spiral's surface quality, which will affect its performance. Therefore, the proposed slicing algorithm can overcome all such limitations when printing helical shaped objects around a rotating column. The proposed slicing algorithm can slice helical shapes in a radial direction, generate tool paths

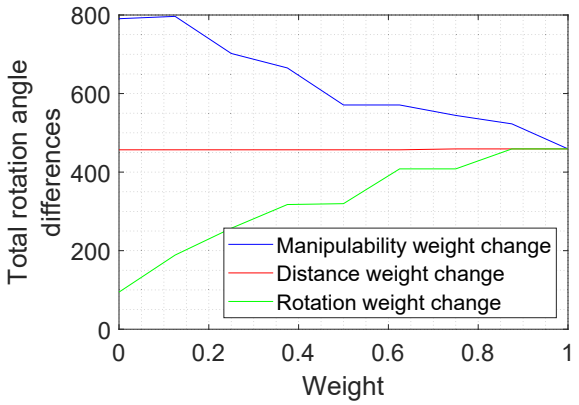

FIGURE 7.19: Path deviation with weight change [11].

and enable simulations to visualise the tool paths. This slicing algorithm's limitations are that it has not been designed to slice hollow structures since it is necessary to have infill to print overhanging areas. Additionally, the relationship between manipulability and print failures has also been demonstrated. Different radial start points affect the print's manipulability, which reveals the need to investigate an optimal path planning method during printing. Therefore, a path planning methodology was proposed for radial printing. The proposed method calculates the optimal path for a print head affixed to an industrial robot mounted on a vertical rail. This path planning method samples the print space and uses a cost function with weights, effectively maximising the manipulability, while seeking to minimise any rotational and positional errors. This method has been shown to reduce failures in printing and to improve the accuracy of the overall print. This path planning method thus eliminates the requirement of trial-and-error error approach and provides a systematic solution.

7.4 Conclusion

Printing a helical object in traditional horizontal layer addition has significant drawbacks and therefore, radial printing has been chosen. Two step process has been proposed to generate tool paths for printing helical objects by vertical layer addition. This process consists of radial slicing and a path planning algorithm based on print space sampling. A simulation environment has been created with the actual dimension of the printer. Simulated results shown that this proposed process eliminates the print errors and improve the manipulability during the overall printing process.

Chapter 8

Sensor Placement in 3D-Printed Objects using Voxel-based Optimisation

Determining where an embedded 3D printed sensor should be placed within a large 3D printed object is a new and quite different problem from that found in traditional sensor placement because, sensors are printed inline with the 3D printed object. Whereas traditional sensor placements, sensors are placed in the object separately. Several additional factors must be considered for this application, one of which is the dexterity or ability of the robot arm to print a sensor at a certain location or "printability", as investigated in chapter 7, which is quantified as the measure of normalised manipulability and ranges from 0 to 1. This printability measure can be used to quantify the ability to print a 3D printed sensor in a certain location. Another factor to consider is the design of the sensor. Since conductive traces in the sensor need to be printed inline, the way the traces are arranged is important. This is because sensors with different designs printed at the same location will require the robot arm to follow different paths, necessitating different dexterity levels. The other factor that must be considered is discouraging, or even forbidding, the placement of sensors in certain areas. There are different reasons to avoid placement in certain areas, such as the impact to the overall structure, where sensing material types in a load-bearing

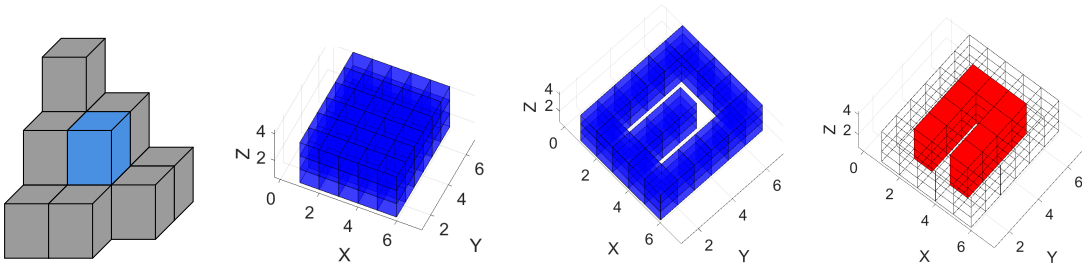

(a) (b) (c) (d)

FIGURE 8.1: Voxel illustrations [12]: a) Set of voxels with one voxel shaded; b) 3D voxels in a size of 3 x 6 x 3; c) Base voxels, V_l; d) Sensor voxels, V_s.

area might reduce the object's structural integrity. This chapter proposes a novel sensor placement method for 3D printed objects using voxels. Voxels are the 3D equivalent of 2D pixels [210]. This chapter proposes extending 2D kernels, which have been used in image processing, to 3D space for sensor placement [211].

8.1 Methodology

8.1.1 Voxels

Voxels, also known as volume pixels, are the 3D equivalent of 2D pixels [210]. Voxels represent a value in a regular grid in 3D space. There are various applications of voxels, including in medicine [212], computer graphics [213], and robot perception [214]. For computationally expensive tasks, such as mapping, meshing, matrix-based solution methods and volume integration, voxels reduce the complexity [215]. A set of voxels with one voxel shaded is shown in Fig. 8.1a.

8.1.2 Extension of 2D Kernels into 3D Space

In image processing, a kernel is a 2D mask or a matrix used for various operations, including sharpening, blurring and edge detection [216]. Fig. 8.2a shows such a matrix with the weight of a cell, is $W_{i,j} \in \mathbb{R}$, for the row index, j and the column index, i. This chapter proposes extending the 2D kernel into 3D space where the weight in a voxel is $W_{i,j,k}$ and

the Z-index is k. A 3D kernel was created, as shown in Fig. 8.1b, when a 2D kernel is extended into 3D space, as in Fig. 8.2a.

8.1.3 Inclusion of Sensor Placement Aspects Using Voxels

The proposed method is based on voxelising (converting the 3D object to voxels) the object and the sensor that needs to be placed. This method is followed by identifying sets of voxels in the size and shape of the sensor and placing them in the object while considering different constraints. A single objective function has been proposed to represent all the factors to evaluate a given location for the placement of sensors.

A sensor can have an arbitrary 3D shape. For example, consider a strain sensor with "U"-shaped conductive traces and a cuboid shape. There are two types of voxels defined within the cuboid. Base voxels, which surround the conductive traces (Fig. 8.1c), and sensor voxels, which overlap with conductive traces (Fig. 8.1d). Figs 8.1c and d show these voxels separately, despite their residing in the same cuboid. Two types of voxels were defined so that it was possible to assign two separate values to each: the weight of a sensor voxel, W_S, and the weight of a base voxel, W_B. The voxel size can be tuned based on the required granularity and the minimum trace width of the conductive traces. Consider an arbitrary distribution of a property, $X_{i,j,k} \in \mathbb{R}$, in 3D space. Assume this to be the property that the sensor is used to measure—strain, in this example. This research aims to consider aspects of the sensor placement, such as printability, the design of the sensor, information gain and the ability to discourage sensor placement in certain areas. The following sections describe how voxels incorporate these various aspects. For simplicity and clarity, a single-layer voxel set was used as an example. The selected kernels with weight values are shown in Fig. 8.2b, in which $W_S = 2$ and $W_B = 1$. The grey-coloured voxels are sensor voxels. An example of strain distribution ($X_{i,j}$) is shown in Figs 8.2c and d in two different potential sensor locations.

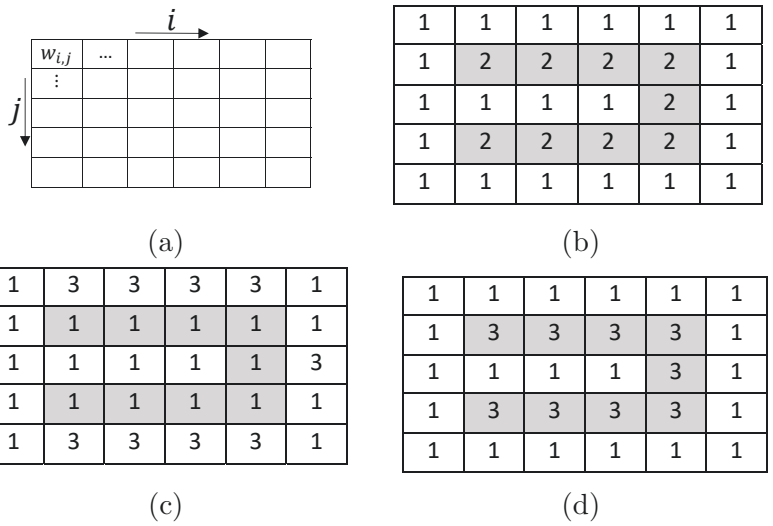

1	1	1	1	1	1
1	2	2	2	2	1
1	1	1	1	2	1
1	2	2	2	2	1
1	1	1	1	1	1

1	3	3	3	3	1
1	1	1	1	1	1
1	1	1	1	1	3
1	1	1	1	1	1
1	3	3	3	3	1

1	1	1	1	1	1
1	3	3	3	3	1
1	1	1	1	3	1
1	3	3	3	3	1
1	1	1	1	1	1

FIGURE 8.2: Kernel illustrations [12]: a) General 2D kernel; b) Selected kernel; c) Location A; d) Location B.

8.1.3.1 Design of the Sensor

In general, an integrated 3D printed sensor will occupy some volume within a larger object. The sensor has a shape that depends on the arrangement of the conductive traces, which are used to measure the parameters of interest, such as the temperature or strain. Additionally, since the sensor should be placed inside the object, within its physical dimensions and, therefore, the sensor's volume should also be considered. The shape and volume of the voxel set were chosen to match the shape and sensor volume to address these factors.

8.1.3.2 Information Gain

For a given object, and a parameter of interest that is to be measured in that object, the parameters value may be unequally distributed within the object. A rigid body exposed to a heat or load source at one point will experience a range of temperatures and loads throughout the body. Concentration points may exist, and there may only be a limited number of places in the object wherein the parameter value is high enough to be measured. Less effective measurements will be obtained if the sensors are placed without considering the amount of information that can be gained at all points within the object. An FEM was used in this research to compute the distribution of the parameters that needs to be

measured within the object. This allowed for the estimation of the amount of information that could be extracted at a given location in a simulated model.

A more effective measurement of the parameter would be possible if the conductive traces were placed closer to a high-value parameter distribution. To accommodate this, a weighting method was proposed. Consider the 2D kernel ($W_{i,j}$) in Fig. 8.2b and the two different 2D distributions of the parameter of interest in Figs 8.2c and d. The kernel values in Fig. 8.2b are denoted as $A_{i,j}$, and the kernel values in Fig. 8.2d as $B_{i,j}$. In both locations, there are equal numbers of 3s and 1s; therefore, $\Sigma A_{i,j}$ and $\Sigma B_{i,j}$ are equal. However, $\Sigma(B_{i,j} \cdot W_{i,j})$ has a larger value than $\Sigma(A_{i,j} \cdot W_{i,j})$. Therefore, the proposed weighting kernel methodology favours Location B, even though both locations have the same number of values.

8.1.3.3 Printability: Calculation of a Robot's Ability to 3D Print

It is necessary to print internal traces inline with a conductive material using different patterns that depend on the type of the sensor. Therefore, even though a selected location may be ideal for the information gain, it might be difficult to print the required sensor at this same location. In the developed printer, the robot manipulators were used to move the extrusion head. To quantify the ability to print, a manipulability measure was employed [10]. The measure of manipulability was explained earlier in Chapter 7 Section 7.1.1.7. For the sensor placement, manipulability was used as a distribution in the three-dimensional space and with the decided kernel to evaluate a given voxel location. If the manipulability distribution in a voxel set is $M_{i,j}$, the ability to print at that location (i.e. the printability) can be calculated using $\Sigma(M_{i,j} \cdot W_{i,j})$.

8.1.3.4 Penalties to Discourage Sensor Placement

3D printed sensors have a different material from the base material of the object; hence, their mechanical properties differ from those of the base material of the structure. Therefore, the placement of a sensor in a given location might adversely affect the object's

structural properties. In a large, load-bearing object such as the GSS, this can be an issue. Further reasons, such as aesthetic concerns or attachment points might dictate other places where the sensors should not be embedded. Hence, it is necessary to consider places in which sensors should not be placed. Another distribution, $R_{i,j} \in \{0, 1\}$, was added to the 3D kernel, whereby a 0 value allowed for the placement of a sensor in the grid location and a 1 value forbade its placement. Eq. (8.1) shows the percentage of penalised voxels in a selected location. The number of voxels in a given location at which sensors should not be placed is $n_r \in [0, n(V_l)]$ the number of base voxels is $n_b \in [0, n(V_b)]$ and the number of sensor voxels is $n_s \in [0, n(V_s)]$, where the notation $n(A)$ denotes the number of elements in set A.

$$n_r/(n_b + n_s) \tag{8.1}$$

8.1.4 Steps of Sensor Placement

To incorporate the aforementioned factors, the following steps were taken.

8.1.4.1 Voxelise the 3D Printable Object

The volume and the shape of the printed object were converted into a set of voxels, V_{obj}. The sensor's dimensions were user-defined and dependant on the actual physical dimensions of the sensor (width 56 mm, length 69 mm, height 7 mm).

8.1.4.2 Calculate Printability and Information Value Distributions

A point cloud of manipulability values, $m_{x,y,z}$, was generated, wherein x, y, z represented the Cartesian coordinates using a printing simulation. This point cloud had a value of manipulability and a Cartesian location. For each volume, the point cloud values were averaged. There were lower and upper bounds for the x, y, z values, represented by $x^-, x^+, y^-, y^+, z^-, z^+$, where $x^- < x^+, y^- < y^+, z^- < z^+$ for each voxel in the set. As

shown in Eq. (8.2), for each voxel the manipulability values were averaged, subject to lower and upper bounds. Here, n_{mv} is the number of manipulability points within the voxel. The normalised manipulability set, X_m, is composed with a collection of these averaged manipulability values divided by the maximum voxel manipulability value, m_{max}, as shown in Eq. (8.3) and Eq. (8.4), wherein the number of voxels is n. The distribution of information, X_I, can be calculated using FEA to create a point cloud of parameter values, such as the predicted temperature and strain measurements.

$$m_{v1} = \frac{\sum m_{x,y,z}}{n_{mv}} \tag{8.2}$$

$$m_{max} = max(m_{v1}, m_{v2}, \ldots, m_{vn}) \tag{8.3}$$

$$X_m = \{m_{v1}/m_{max}, \ldots, m_{vn}/m_{max}\} \tag{8.4}$$

8.1.4.3 Select Sensor Location and Sensor Voxel Sets

The next step was to select the subset of the sensor location voxels, V_{loc} ($V_{loc} \subseteq V_{obj}$), whereby each voxel set would encapsulate the overall sensor shape and volume and would thus necessarily have dimensions at least as large as those of the sensor from V_{obj}. These voxel sets were spread throughout the entire object in various orientations. The user selected the orientations and locations for the sensors based on practical application. For large-scale objects, this is important because it simplifies the computations. The best locations were selected from these candidate sensor locations. V_l is the set of "base" voxels that represent the volume that protects, encompasses and determines the physical spacing between two consecutive sensors or traces that themselves are represented by the voxels, V_s. From each voxel location set, V_l ($V_l \in V_{loc}$), a sensor voxel set, V_s ($V_l \subseteq V_{loc}$), was selected in the shape of the conductive traces and the remaining base voxel set was V_b ($V_b = V_l - V_s$).

8.1.4.4 Calculate and Optimise the Objective Function Value for Each Location

A set of voxels, V_r, was selected in the areas in which sensor placement was penalised or forbidden for V_{obj}. Eq. (8.5) shows how the percentage of penalised voxels were calculated for each V_l.

8.1.4.5 Calculating and Optimising the Objective Function Value for Each Location

A set of objective functions were used as the final step to evaluate each potential location while considering all these factors to select the best locations. A slightly different number of voxels were present at each location because converting a sensor shape to a voxel requires an approximation of the original shape. Therefore, for the sensor and base voxel sets, the manipulability and information values were calculated on a per voxel basis as shown in Eq. (8.6) to Eq. (8.9). The objective function is shown in Eq. (8.10), wherein W_R is the weight for the penalised voxels. These weight values can be tuned depending on the importance of the factors for a given application.

$$R_l = \frac{|V_l \cap V_r|}{|V_l|} \tag{8.5}$$

$$I_B = \frac{\sum X_I \cap V_b}{|V_b|} \tag{8.6}$$

$$I_S = \frac{\sum X_I \cap V_s}{|V_s|} \tag{8.7}$$

$$M_B = \frac{\sum X_m \cap V_b}{|V_b|} \tag{8.8}$$

$$M_S = \frac{\sum X_m \cap V_s}{|V_s|} \tag{8.9}$$

$$\begin{aligned} C_l = W_B \cdot I_B + W_B \cdot M_B + W_S \cdot I_S \\ + W_S \cdot M_S - W_R \cdot R_l \end{aligned} \tag{8.10}$$

To identify optimal sensor locations, researchers have used FEM-based methods [172–175], information-based methods [176, 177, 179] and various optimisation methods [171, 180–182]. The proposed optimisation method used in this chapter is similar to pareto-based optimisation [217]. The voxel sets were ranked from the highest C_l value to the lowest after calculating the value of the objective function for each voxel set. The most suitable location was the one with the highest C_l, depending on the requirements; however, multiple sensor locations could also be selected from the remaining ranked list.

8.2 Experimental Results

To perform the FEA, ANSYS was used. Then Matlab was employed for the voxel computations and the Robotics Toolbox [203], developed by Peter Corke, was utilised for the robotic simulations.

8.2.1 Voxelisation of the Object

The 3D printed object in this application was the GSS. The 3D model of the GSS was exported to a STL file using a CAD program (SolidWorks). Fig. 8.3a shows this 3D model. The width, length and height of the spiral were 0.7 m x 0.7 m x 1.4 m, respectively. Using Matlab, the spiral was voxelised into around 100 x 100 x 200 voxels. The voxelised GSS is shown in Fig. 8.3b and Fig. 8.3c provides a closer view of the voxels.

8.2.2 Calculating Printability and Information Distributions

The same simulation environment developed in Chapter 7 and Section 7.1.1.6 was used to obtain a manipulability distribution (also representing printability [10]) for printing. Manipulability values were calculated along all print trajectories and then exported as a point cloud, as shown in Fig. 8.4a. This point cloud was subsequently voxelised and the printability values were averaged and normalised into voxels.

To determine the strain distribution in the GSS as a result of the expected loads from the weight of the slurry, an ANSYS software FEA method was used. Several modelling

decisions were made in the execution of the FEA. For this example, the GSS was approximated by a swept profile. Fig. 8.3a shows the resulting 3D CAD model of the GSS, which was divided into hexahedral mathematical volumes in a process referred to as "meshing". Two mesh elements were used to capture the strain distribution sufficiently through the thickness of the spiral profile. Around 500 mesh elements were used to divide the length of the swept profile. For simplicity, a zero-displacement boundary condition in the model was used to replace the central column that supports the helical spiral-shaped part of a real GSS. Note that this assumption has no impact on the real-world behaviour of the GSS. A downward force of 10 kg, distributed over the spiral surface, was used to represent the operational loads on a GSS. In the simulation, standard gravitational acceleration was enabled. A Poisson's ratio of 0.49, a Young's modulus of 201.8 MPa and a yield strength of 73.5 MPa were used in a linear-elastic material in the model, which are similar to parameter values for the material used in the GSS.

Fig. 8.5 shows the elastic strain distribution of the ANSYS simulation. These results were also exported to a point cloud and averaged and normalised into voxels, so that they could be fused with previously calculated printability values, which is the normalised manipulability measure between 0 and 1.

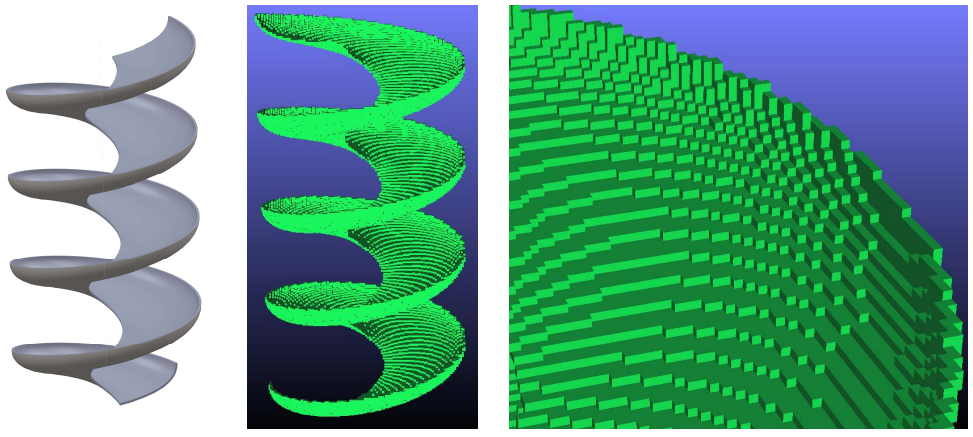

(a) (b) (c)

FIGURE 8.3: 3D models of the spiral [12]: a) A smoothed representation of the spiral surface; b) A voxelised 3D model of the spiral; c) A closer view of the voxels.

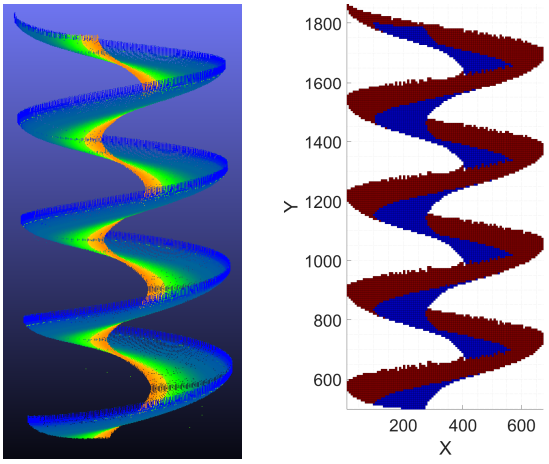

(a) (b)

FIGURE 8.4: a) Manipulability point cloud with the colours representing the value of manipulability from orange to green and to blue indicating the transition from high to low manipulability values [12]. b) An example of penalised voxels where sensors placement is discouraged are shown in red [12].

8.2.3 Location Selection and Sensor Voxels

A voxel set, V_{loc}, in a rectangular shape (length: 9 voxels; width: 8 voxels) that was similar to the base of the strain gauge was calculated using Matlab. A strain gauge was selected for each V_l and V_s in a "U" shape (length: 4 voxels; width: 5 voxels; thickness: 1 voxel). All V_l that selected are shown in Fig. 8.7a and a bottom-up, closer view is shown

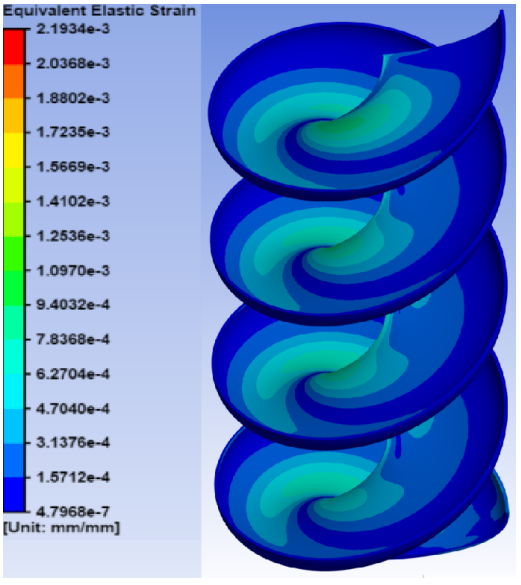

FIGURE 8.5: ANSYS strain simulation result [12].

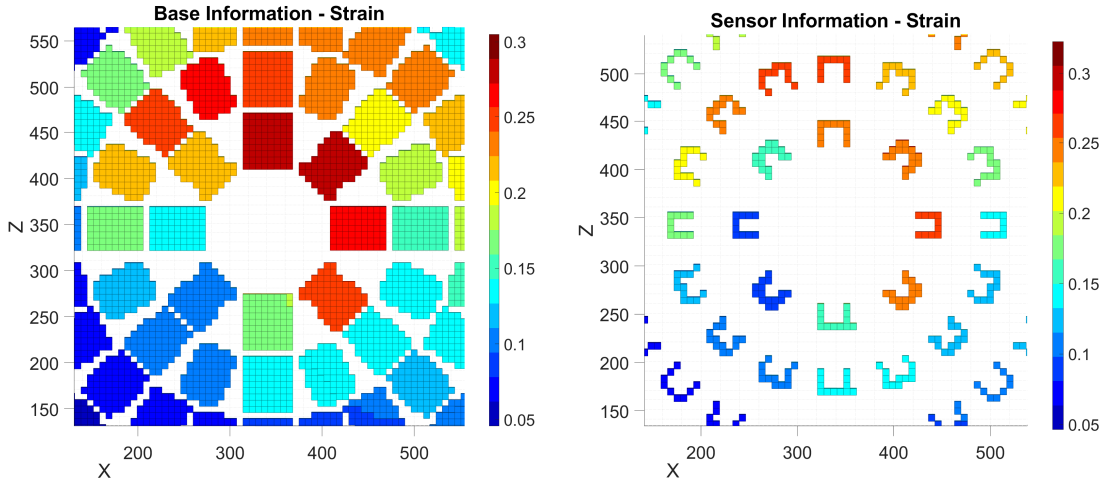

(a) (b)

FIGURE 8.6: Bottom-up viewpoints of the voxels showing the strain values relating to the desirability of their placement [12]: a) Base voxels for strain, V_l; b) Sensor voxels for strain, V_s.

in Fig. 8.6a. The strain point clouds exported from ANSYS became sparse at the end of the spiral; therefore, some voxels sets were missing at the edge of the spiral, as shown in Fig. 8.7a. These blank spots were caused by voxels without any averaged strain values in V_l. The locations in V_l containing more than 80% empty voxels were removed in this experiment. A more finely distributed point cloud may offer a plausible solution to this problem. There was a slightly different number of voxels in the sensor encapsulation, as visible in Fig. 8.6b. This is because of errors that occur when approximating the shape with voxels.

8.2.4 Calculation of the Percentage of Penalised Voxels

Placing sensors in the outer diameter of the GSS is not ideal in this application; therefore, a set of voxels closer to the inner diameter were selected, as shown in Fig. 8.4b, as penalised voxels. The percentages were then calculated for each V_l, as explained in Section 8.1.4.4.

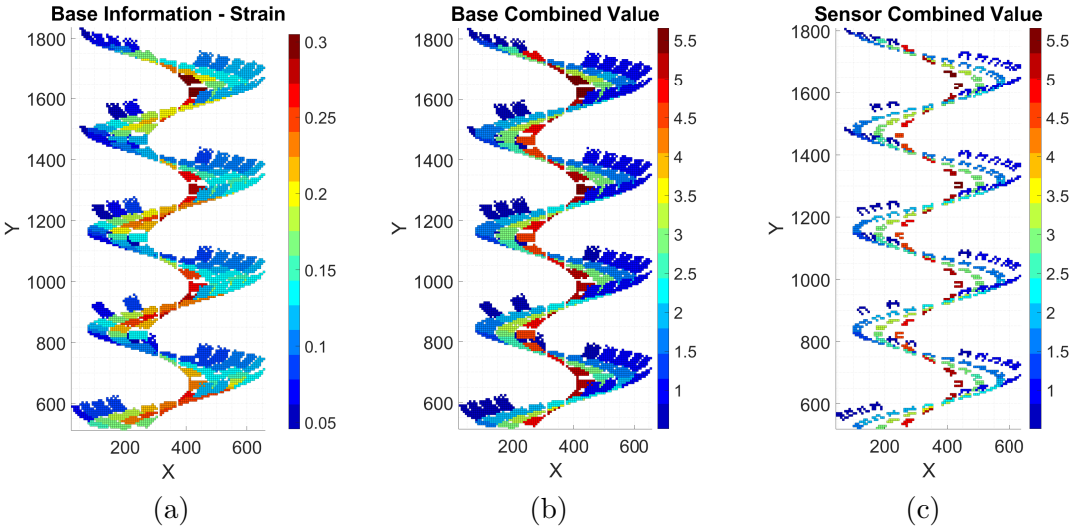

FIGURE 8.7: Voxel sets in the spiral [12] with the colour legend representing the average information per voxel: a) V_l for strain; b) Calculated combined values for V_l; c) Calculated combined values for V_s.

8.2.5 Calculation of the Objective Functions and Best Location Selection

The weighting values were selected according to the importance of the different factors: for the weight of the sensor voxels, $W_S = 3$; for the weight of the base voxels, $W_B = 1.5$; and for the weight of the penalised areas $W_R = 1$. A higher weight value was assigned to

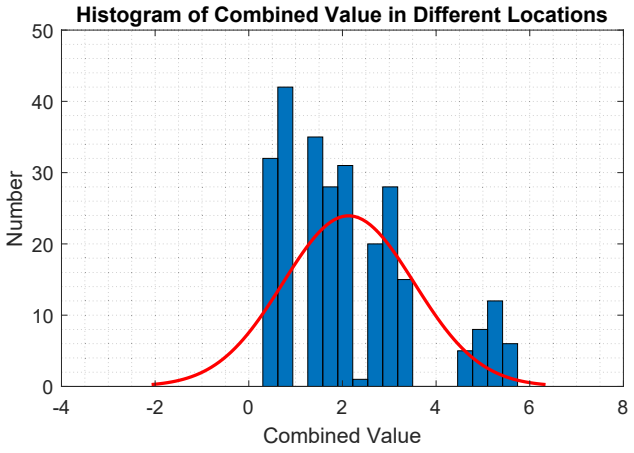

FIGURE 8.8: Histogram of the combined values [12].

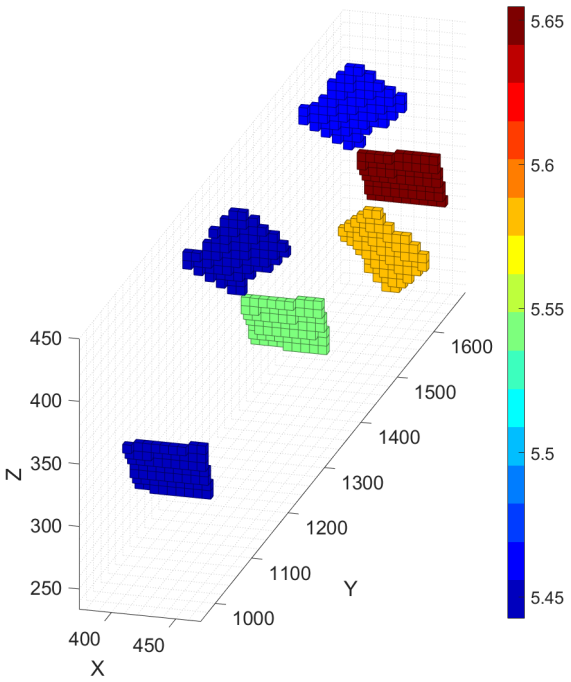

FIGURE 8.9: Six locations with the highest objective value [12].

V_s since the printed traces measure the strain to which they are subjected. Therefore, the weights were selected to bias important conductive traces.

Each location was ranked and the top locations were selected depending on the required number of sensors after calculating the objective function value of each V_l. The calculated combined values from the objective function for V_l and V_s are shown in Figs 8.7b and c. Fig. 8.8 shows a histogram of the distribution of the calculated combined values of the objective function in around 316 sensor locations. The mean objective function value was 2.13 and the minimum and maximum values were 0.41 and 5.65, respectively. The areas near the centre of the spiral appear more suitable for placement since a higher objective function value was observed there, as shown in Figs 8.7b and c. The weight values for the six locations with the highest values are shown in Table 8.1, where $WI_B = W_B \cdot I_B,\ WM_B = W_B \cdot M_B,\ WI_S = W_S \cdot I_S,\ WM_S = W_S \cdot M_S,\ WI_R = W_R \cdot R_l$.

As demonstrated in Fig. 8.4a and Fig. 8.5, this observation aligns with the way in which the highest values of manipulability and strain are spread in this area. It is possible to observe that there are no penalised voxels near the column (Fig. 8.4b), which concurs with

TABLE 8.1: Weighted values of the selected locations [12].

Loc.	WI_B	WM_B	WI_S	WM_S	WI_R	C_l
1	0.40	1.38	0.80	2.86	0	5.44
2	0.43	1.38	0.89	2.86	0	5.55
3	0.45	1.38	0.97	2.86	0	5.65
4	0.41	1.35	0.84	2.84	0	5.44
5	0.40	1.35	0.86	2.84	0	5.45
6	0.46	1.35	0.93	2.85	0	5.59

the absence of zero values in the WI_R column in Table 8.1. A zero under WI_R confirms that the selected location is sensible.

According to the selected criteria, Fig. 8.9 shows the six highest objective value locations or the most suitable positions for the sensors. A spider plot was created, as shown in Fig. 8.10, comparing all five aspects of the objective function. The WI_R was zero because all the locations were outside the area in which sensor placements were discouraged. From Fig. 8.10, the change in $WI_B = 0.06$, $WM_B = 0.03$, $WI_S = 0.17$, $WM_S = 0.02$ and $C_l = 0.21$ hence, each location was determined to have similar values.

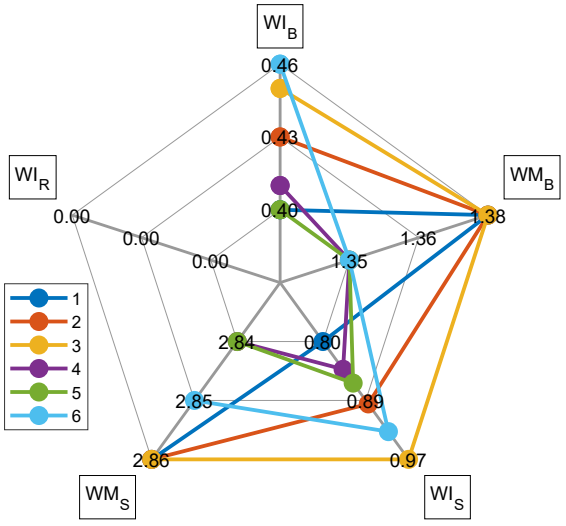

FIGURE 8.10: Spider plot of the selected top six positions [12].

8.3 Discussion and Conclusions

Sensor placement is a critical aspect of structural health monitoring. Sensor placement optimisation will reduce instances of inefficient false positives and will improve the quality of the data. In this application, several specific elements need to be considered. This chapter has proposed a way to place 3D printed sensors into an object while considering the information gain from the sensors; the shape; volume and design of the sensors; the areas in which sensor placement should be discouraged; and the ability to print the sensors in the given locations. The sensor and the object were voxelised to consider the volume and shape of the sensor, which was demonstrated using a "U"-shaped strain sensor. A FEM simulation was conducted to obtain a strain distribution in the GSS since one key sensor that needs to be placed measures the strain. Manipulability measure was used to measure the printability for the sensor placement and the Matlab environment was used to simulate the 3D printing with a robot arm and generate an exportable point cloud that encapsulates the manipulability measures. The penalising of certain voxels was proposed to avoid placing sensors in certain locations. To combine all these aspects, a weighted objective function was suggested, that could be tuned based on the application requirements. A set of potential sensor locations with the highest objective function value was selected in the final step. The experimental results showed that the manipulability and strain distribution of the GSS had higher values near the central column area of the spiral, as visible in Fig. 8.3a and Fig. 8.5. Hence, the locations near the central column of the GSS were selected, as shown in Fig. 8.9. According to the information that can be gathered by each sensor, and the predicted amount and distribution of information available, it would be possible to determine the number of sensors that need to be placed. However, in this research, the user selected the number of sensor locations. Since voxelisation and manipulability calculations are applicable to any robot arm-based 3D printing, the proposed method can be generalised and adapted to 3D printed sensor placement in any 3D printed object.

Chapter 9

Conclusions

This thesis presented 3D printable sensors that can measure various parameters, such as temperature, strain, wear and vibration, which can be embedded in 3D printed objects and non-3D printed sensors to measure parameters like flow rate. The overall objective of the research is to make the spiral "smart" by measuring parameters that impact its performance and lifetime. 3D printing sensors enables the inline printing of sensors in AM, so that post-processing or the placement of sensors will not affect the structural integrity of the object. Additionally, the developed sensors can be printed in any commercially available extrusion-based 3D printer with inexpensive, readily-available filaments.

To achieve the printing of a GSS with various layers, materials and integrated sensors, it was necessary to develop a novel radial slicing algorithm for the bespoke helical GSS printer. Traditional Z-direction slicing cannot be used since it would require an undesirable amount of additional support material and a considerable amount of extra time to print the spiral. Further, the removal of such support material would reduce the spiral's surface quality. The radial slicing algorithm that was presented overcomes the limitations of a traditional slicer, and integrates with a robot arm path planning method that uses manipulability as a printability measure. For the radial slicing and printing, the path planning from the spiral's central column to the end of the spiral was conducted using a weighted cost function. This planning method works to maximise the printability, while

minimising the Cartesian error and the rotation error as the end effector tool executes the radially sliced print trajectories.

After developing 3D printable sensors along with radial slicing and path planning algorithms for 3D printing, the final step was to determine the ideal sensor placement locations. The method proposed in this thesis was specifically designed for 3D printed sensor placement into 3D printed objects. The proposed method is based on voxels and considers information gain, printability and the areas in which sensor placement needs to be discouraged. The experimental results revealed that the proposed methodology could incorporate all these factors.

This thesis presented and covered the development of 3D printed sensors, the creation of slicing and path planning algorithms for 3D printing and the identification of optimal locations for the placement of the sensors.

9.1 Summary of Contributions

9.1.1 A 3D Printable Wear Sensor That Can Measure the Location and the Depth of the Wear

The 3D printed wear sensor proposed can be used to measure both depth of the wear and the wear location. The sensor was printed using carbon-based conductive filament, and the experiment showed that the sensor is capable of measuring wear using the resistance measurements in real-time. A cluster of such sensors with the proposed pattern will help to get a three-dimensional view of the wear. This work was published in the International Symposium on Automation and Robotics in Construction (ISARC 2019) [4].

9.1.2 A 3D Printable Strain Sensor with Temperature Compensation

The proposed 3D printed strain sensor can be printed onto real-world, large-scale equipment, such as the GSS, to measure creep. From the experiments, a near-linear relationship between resistance and strain with minor hysteresis was evident. Additionally, the testing

showed the viscoelastic properties of the strain gauge. Apart from this, standard tensile testing was conducted in non-conductive and conductive PLA with different raster angles to identify the material properties. This work was published in the International Conference on Cybernetics and Intelligent Systems and IEEE Conference on Robotics, Automation and Mechatronics (CIS-RAM 2019) [5].

A temperature compensated strain sensor was developed using the same carbon-based filament and employing the Wheatstone bridge design. This sensor was tested in an insulated chamber. The proposed sensor was able to reduce the error significantly (by 68%) for temperature changes. Additionally, the strain measurement revealed that the printed sensor had low hysteresis and established the near-linear relationship between bending strain and voltage. This work was published in the IEEE International Conference on Robotics and Automation (ICRA 2021) [6].

9.1.3 A 3D Printed Vibration Sensor Based on Electromagnetism

The proposed 3D printed vibration sensor uses a carbon-based conductive filament based on electromagnetic induction. An ANSYS simulation was conducted to establish constraints in the design and provide information on the relationship between several parameters, including velocity and number of turns. Physical testing was conducted, providing an in-depth understanding of the capabilities of the material and prototype. This work is under review in the Q1-ranked journal Sensors and Actuators: A. Physical [7].

9.1.4 An Integrated 3D Printable Temperature Sensor

The developed 3D printed temperature sensor is capable of being embedded into a 3D printed object. The results showed that the sensor was capable of measuring the temperature within the acceptable error margin. This sensor will help to address the requirement for embedding sensors inside objects, by ensuring that the sensor will not affect the object's structural integrity. The proposed method requires inexpensive material and a commonly available 3D printer. This work was published in the Australasian Conference on Robotics and Automation (ACRA 2020) [8].

9.1.5 A Sensor Fusion Approach for Partially-filled Pipe Flow Meters

The proposed flow meter is an inexpensive and easily extensible sensor fusion approach to improving the accuracy of the traditional transit-time ultrasonic flow meter in a partially-filled pipe, such as those entering or leaving the GSS. When the flow level is low, common transit-time flow meters fail to accurately measure the inadequate error margin. The proposed method depends on measuring the liquid level using a capacitance-based level sensor and on determining the sound propagation pattern to ascertain the accurate flow rate. This method was tested with different flow levels and proved to calculate an accurate error rate within an acceptable error margin. This work was published in the Q1-ranked IEEE Sensors Journal [9].

9.1.6 A Radial Slicing Algorithm and Optimal Path for Helical 3D Printing

The proposed radial slicing algorithm can be used to slice large-scale helical objects. This method is different to traditional Z-direction slicing. Various helical shapes were sliced and tool paths were generated. These tool paths were then executed in a simulation environment that conformed to the developed printer's physical dimensions. The proposed slicing method overcame the limitations of the traditional slicing method for helical objects, such as undesirable step-wise bumps on the surface and the waste of support material. Additionally, the robot arm's manipulability measure was shown to be a useful analogous to printability. This work was published in the Q1-ranked International Journal of Advanced Manufacturing Technology [10].

During the initial printing simulations, it was observed that the prints could fail if they took certain outward radial paths. Therefore, an optimal radial path planning method was developed and tested. This method sampled the print space, and then devised and utilised a cost function that considered manipulability, the Cartesian error and the rotation error. The approach improved upon the initial trial-and-error method, by providing a systematic technique. This was shown to increase the robot's overall manipulability during printing, which in turn assisted with the embedded sensor placement research. This work was

published in the IEEE International Conference on Control, Automation, Robotics and Vision (ICARCV 2020) [11].

9.1.7 Optimal 3D Printed Sensor Placement in 3D Printed Objects

A method was proposed to address the important aspect of sensor placement for structural health monitoring. The method focused on 3D printed sensor placement in 3D printed objects considering the factors of information gain, printability, design and the sensor's dimensions using a voxel-based approach. The experimental results showed that for the placement of a set of strain sensors, the identified locations were optimised for all the factors considered in 3D printed sensor placement. This work is published in the Q1-ranked Journal of Intelligent Manufacturing [12].

9.2 Discussion of Limitations

Advances in manufacturing are transforming the world's manufacturing industry into its next incarnation: Industry 4.0. This research and development project aimed to create necessary technologies for applying AM to equipment manufacturing for the mining industry. During this research, various sensors were developed. Since the fabrication method of these sensors is independent of their application, these sensors can be used in any 3D printed objects and are not specific to the GSS. Uncertainties in the design would mainly depend on the physical parameters of the printer such as the print accuracy and the properties of the material used. This is also true of the developed partial flow meter. Therefore, all the developed sensors presented in this thesis can measure various parameters of other 3D printable equipment.

The limitations are that the slicing method and the path planning method were developed specifically for radial printing as opposed to traditional Z-direction slicing and vertical layer printing. Therefore, these methods are not generalisable to traditional printing. However, printhead path planning that considers manipulability, the Cartesian error and the rotation error is applicable to any 3D printer that uses a robot arm for printing to optimise the robot arm's dexterity and to reduce print errors.

The proposed sensor placement method for 3D printing considers printability, information gain and the areas in which sensor placement is discouraged. Therefore, the proposed method can be used in any robot-based 3D printing, as it considers all three factors. However, since this method depends on the weighted cost function, it is possible to remove or add various factors. If the printability aspect is removed, the proposed voxel-based sensor placement can be used in any 3D printed sensor placement and is not limited to robot-based 3D printing. Additionally, the proposed method is adaptable and could be complemented by other aspects that need to be considered for the specific requirements of other applications.

9.3 Future Work

In terms of the 3D printable wear sensor, an improved version of the sensor with a similar pattern could be designed to help to obtain a three-dimensional view of the wear. Once the printer is built, it will be possible to investigate the use of such a sensor to get a better picture of the wear.

With the temperature compensated strain sensor, it is possible to investigate and test the use of this sensor to identify the long-term creep of the spiral. Additionally, it is possible to investigate the design of a single, self-contained sensor to measure strain in multiple directions.

For the integrated 3D printable temperature sensor, it is necessary to do more testing regarding the structural integrity if multiple sensors are to be placed closer to each other, particularly if they are embedded in the base structure.

For the 3D printed vibration sensor, a permanent magnet was used. We were unable to create a viable and efficient electromagnet since the 3D printed coil had considerably higher resistance. This is a drawback, eliminating the ability to create a fully 3D printed sensor. Therefore, future research should investigate novel AM techniques for metal and the 3D printing of coils with alternative metal filaments, in pursuit of a viable 3D printed electromagnet.

Ideally, for all the 3D printed sensors that have been developed, the long-term (multi-year) testing should be conducted in order to understand and characterise their long-term performance.

The challenges to be solved to make customised 3D printed sensors feasible and available to the general population in the near future are mainly related to the accessibility of high-accuracy, low-cost, low-maintenance, multi-material printers, which can rapidly switch between feed material without excessive material wastage.

Regarding the partially-filled pipe flow meter, it can be attached to the entry and exit pipes before and after separation. This could make the GSS smarter and able to predict and potentially automatically change the separation cuts and the operating parameters based upon the measured flow entering and exiting the pipes for a GSS.

In terms of future work of the slicing algorithm, it needs to be extended so it can cater to the different types of infills and overhangs. This is because, in some applications, having a different infill will allow the object to be printed with less material in less time. Additionally, improvements to the algorithm are possible so it can more optimally slice complex structures that have overhanging parts.

It is possible to investigate the use of the proposed voxel-based sensor placement algorithms for other sensor placement which are not 3D printed. Since the same concepts of information gain and sensor discouraged areas can be used for conventional non-3D printed sensors.

The next step of the research would be to undertake predictive maintenance using the collected data. Engineers have already developed a digital twin for the GSS and the data collected from various sensors can be used to predict short- and long-term failures. This will include determining a suitable model for understanding the nature of the data and predicting failures or planned maintenance. It will help to reduce the unplanned downtime and, hence, to increase the production output. Additionally, monitored data over long durations, such as for creep and wear, will help to identify potential material-related issues and provide insights to improve the design.

Bibliography

[1] Daniel Gräbner, Simon Dödtmann, Gerrit Dumstorff, and Frieder Lucklum. 3-D-printed smart screw: functionalization during additive fabrication. *Journal of Sensors and Sensor Systems*, 7(1):143–151, 2018.

[2] Sameh Dardona, Alan Shen, and Cagatay Tokgoz. Direct Write Fabrication of a Wear Sensor. *IEEE Sensors Journal*, 18(8):3461–3466, 2018.

[3] Zhouyue Lei, Quankang Wang, and Peiyi Wu. A multifunctional skin-like sensor based on a 3D printed thermo-responsive hydrogel. *Materials Horizons*, 4(4):694–700, 2017.

[4] M I N P Munasinghe, Lewis Miles, and Gavin Paul. Direct-Write Fabrication of Wear Profiling IoT Sensor for 3D Printed Industrial Equipment. In *Int. Symposium on Automation and Robotics in Construction*, pages 862–869, 2019.

[5] Nuwan Munasinghe, Matthew Woods, Lewis Miles, and Gavin Paul. 3-D Printed Strain Sensor for Structural Health Monitoring. In *IEEE Int. Conf. on Cybernetics and Intelligent Systems and the Int. Conf. on Robotics, Automation and Mechatronics*, 2019.

[6] Nuwan Munasinghe, John Masangkay, and Gavin Paul. Temperature Compensated 3D Printed Strain Sensor for Advanced Manufacturing Applications. In *IEEE Int. Conf. on Robotics and Automation*, 2021.

[7] John Masangkay, Nuwan Munasinghe, Peter Watterson, and Gavin Paul. Simulation and Experimental Characterisation of a 3D-Printed Electromagnetic Vibration Sensor. *Sensors and Actuators: A. Physical*, Under Revi, 2021.

[8] Nuwan Munasinghe and Gavin Paul. Integrated 3-D Printable Temperature Sensor for Advanced Manufacturing. In *Australasian Conference on Robotics and Automation*, 2020.

[9] Nuwan Munasinghe and Gavin Paul. Ultrasonic-Based Sensor Fusion Approach to Measure Flow Rate in Partially Filled Pipes. *IEEE Sensors Journal*, 20(11):6083–6090, 2020.

[10] Nuwan Munasinghe and Gavin Paul. Radial slicing for helical-shaped advanced manufacturing applications. *The International Journal of Advanced Manufacturing Technology*, 112(3-4):1089–1100, 2020.

[11] Nuwan Munasinghe and Gavin Paul. Path Planning for Robot Based Radial Advanced Manufacturing Using Print Space Sampling. In *Int. Conf. on Control, Automation, Robotics and Vision*, 2020.

[12] Nuwan Munasinghe, Thomas Romeijn, and Gavin Paul. Voxel-Based Sensor Placement for Additive Manufacturing Applications. *Journal of Intelligent Manufacturing*, 2021.

[13] TWI. What is Advanced Manufaturing, 2021. URL `https://www.twi-global.com/technical-knowledge/faqs/faq-what-is-advanced-manufacturing`.

[14] CSIRO. Advanced manufacturing : A Roadmap for unlocking future growth opporunities for Australia. Technical Report November, 2016.

[15] Kaufui V Wong and Aldo Hernandez. A Review of Additive Manufacturing. *ISRN Mechanical Engineering*, 2012(208760):10, 2012.

[16] Daniel Delgado Camacho, Patricia Clayton, William O'Brien, Raissa Ferron, Maria Juenger, Salvatore Salamone, and Carolyn Seepersad. Applications of Additive Manufacturing in the Construction Industry. In *Automation in construction*, volume 34, pages 1–8, Vilnius, 2017.

[17] George Z Cheng, Erik Folch, Adam Wilson, Robert Brik, Noah Garcia, Raul San Jose Estepar, Jorge Onieva Onieva, Sidhu Gangadharan, and Adnan Majid. 3D Printing and Personalized Airway Stents. *Pulmonary Therapy*, 3(1):59–66, 2017.

[18] Eric P Flynn. Low-cost approaches to UAV design using advanced manufacturing techniques. In *IEEE Integrated STEM Education Conference*, pages 1–4, 2013.

[19] A V Papadopoulos, S A Asadollah, M Ashjaei, S Mubeen, H Pei-Breivold, and M Behnam. SLAs for Industrial IoT: Mind the Gap. In *Int. Conf. on Future Internet of Things and Cloud Workshops*, pages 75–78, 2017.

[20] M Wollschlaeger, T Sauter, and J Jasperneite. The Future of Industrial Communication: Automation Networks in the Era of the Internet of Things and Industry 4.0. *IEEE Industrial Electronics Magazine*, 11(1):17–27, 2017.

[21] Hongyu Pei Breivold and Kristian Sandstrom. Internet of Things for Industrial Automation-Challenges and Technical Solutions. In *IEEE Int. Conf. on Data Science and Data Intensive Systems Internet*, pages 532–539, 2015.

[22] B K Mishra and Alok Tripathy. A preliminary study of particle separation in spiral concentrators using DEM. *International Journal of Mineral Processing*, 94(3-4): 192–195, 2010.

[23] CSRIO. Advanced manufacturing : A Roadmap for unlocking future growth opporunities for Australia. Technical Report November, 2016.

[24] ISO;ASTM. ASTM52900 Standard Terminology for Additive Manufacturing. Technical report, 2015.

[25] Yasmin Tadjdeh. 3D Printing Promises to Revolutionize Defense, Aerospace Industries. *National Defense*, 98(724):20–23, 2014.

[26] Pshtiwan Shakor, Shami Nejadi, Gavin Paul, and Sardar Malek. Review of Emerging Additive Manufacturing Technologies in 3D Printing of Cementitious Materials in the Construction Industry. *Frontiers in Built Environment*, 4, 2019.

[27] E Heissler, F-S Fischer, S Boiouri, T Lehrnann, W Mathar, A Gebhardt, W Lanksch, and J Bler. Custom-made cast titanium implants produced with CAD/CAM for the reconstruction of cranium defects. *International journal of oral and maxillofacial surgery*, 27(5):334–338, 1998.

[28] Sandeep Munjal, Seth S Leopold, David Kornreich, Susan Shott, and Henry A Finn. CT-generated 3-dimensional models for complex acetabular reconstruction. *The Journal of arthroplasty*, 15(5):644–653, 2000.

[29] Paul S D'Urso, Timothy M Barker, W John Earwaker, Lain J Bruce, R Leigh Atkinson, Michael W Lanigan, John F Arvier, and David J Effeney. Stereolithographic biomodelling in cranio-maxillofacial surgery: a prospective trial. *Journal of cranio-maxillofacial surgery*, 27(1):30–37, 1999.

[30] Yong He, Guang-huai Xue, and Jian-zhong Fu. Fabrication of low cost soft tissue prostheses with the desktop 3D printer. *Scientific Reports (Nature Publisher Group)*, 4:6973, 2014.

[31] M Wollschlaeger, T Sauter, and J Jasperneite. The Future of Industrial Communication: Automation Networks in the Era of the Internet of Things and Industry 4.0. *IEEE Industrial Electronics Magazine*, 11(1):17–27, 2017.

[32] Hongyu Pei Breivold and Kristian Sandstrom. Internet of Things for Industrial Automation-Challenges and Technical Solutions. In *IEEE Int. Conf. on Data Science and Data Intensive Systems Internet*, pages 532–539, 2015.

[33] Hiroki Ota, Sam Emaminejad, Yuji Gao, Allan Zhao, Eric Wu, Samyuktha Challa, Kevin Chen, Hossain M. Fahad, Amit K. Jha, Daisuke Kiriya, Wei Gao, Hiroshi Shiraki, Kazuhito Morioka, Adam R. Ferguson, Kevin E. Healy, Ronald W. Davis, and Ali Javey. Application of 3D Printing for Smart Objects with Embedded Electronic Sensors and Systems. *Advanced Materials Technologies*, 1(1):1600013, 2016.

[34] Ran Zou, Xuan Liang, Mohan Wang, Aidong Yan, Paul Ohodnicki, Albert To, and Kevin Chen. Embedding Distributed Temperature and Strain Optical Fiber Sensors in Metal Components Using Additive Manufacturing. In *Conf. on Lasers and Electro-Optics*, pages 3–4, 2018.

[35] Alexander Dijkshoorn, Patrick Werkman, Marcel Welleweerd, Gerjan Wolterink, Bram Eijking, John Delamare, Remco Sanders, and Gijs J M Krijnen. Embedded sensing: Integrating sensors in 3-D printed structures. *Journal of Sensors and Sensor Systems*, 7(1):169–181, 2018.

[36] Yung-Hang Chang, Kan Wang, Changsheng Wu, Yiwen Chen, Chuck Zhang, and Ben Wang. A facile method for integrating direct-write devices into three-dimensional printed parts. *Smart Materials and Structures*, 24(6):65008, 2015.

[37] R. R J Maier, W. N. MacPherson, J. S. Barton, M. Carne, M. Swan, J. N. Sharma, S. K. Futter, D. A. Knox, B. J S Jones, and S. McCulloch. Fibre optic strain and configuration sensing in engineering components produced by additive layer rapid manufacturing. In *IEEE Sensors*, pages 1353–1357, 2011.

[38] Richard Zelený and Jan Včelák. Strain Measuring 3D Printed Structure with Embedded Fibre Bragg Grating. *Procedia Engineering*, 168:1338–1341, 2016.

[39] Dirk Lehmhus, Claus Aumund-Kopp, Frank Petzoldt, Dirk Godlinski, Arne Haberkorn, Volker Zöllmer, and Matthias Busse. Customized Smartness: A Survey on Links between Additive Manufacturing and Sensor Integration. *Procedia Technology*, 26:284–301, 2016.

[40] Ju Kyoung Lee, Hyun Hee Kim, Jae Won Choi, Kyung Chang Lee, and Suk Lee. Development of Direct-printed Tactile Sensors for Gripper Control through Contact and Slip Detection. *International Journal of Control, Automation and Systems*, 16 (2):929–936, 2018.

[41] Md Omar Faruk Emon and Jae Won Choi. Flexible piezoresistive sensors embedded in 3D printed tires. *Sensors (Switzerland)*, 17(3), 2017.

[42] N H Cook. Tool wear sensors. *Wear*, 62(62):49–57, 1980.

[43] R.M. Douglas, J.A. Steel, and R.L. Reuben. A study of the tribological behaviour of piston ring/cylinder liner interaction in diesel engines using acoustic emission. *Tribology International*, 39(12):1634–1642, 2006.

[44] Luis Henrique, Andrade Maia, Alexandre Mendes, Wander Luiz, Wisley Falco, and Alisson Rocha. A new approach for detection of wear mechanisms and determination of tool life in turning using acoustic emission. *Tribology International*, 92(92):519–532, 2015.

[45] Holger Fritsch, Ralf Lucklum, Thomas Iwert, Peter Hauptmann, Dirk Scholz, Erwin Peiner, and Andreas Schlachetzki. A low-frequency micromechanical resonant vibration sensor for wear monitoring. *Sensors and Actuators*, 62:616–620, 1997.

[46] André Bödecker, Christian Habben, Andreas Sackmann, Kai Burdorf, Erhard Giese, and Walter Lang. Manufacturing of a wear detecting sensor made of 17-4PH steel using standard wafer processing technology. *Sensors and Actuators A: Physical*, 171 (1):34–37, 2011.

[47] A.W. Ruff and K.G. Kreider. Deposited thin-film wear sensors: materials and design. *Wear*, 203-204:187–195, 1997.

[48] Holger Lüthje, Ralf Bandorf, Saskia Biehl, and Birte Stint. Thin film sensor for wear detection of cutting tools. *Sensors and Actuators A: Physical*, 116(1):133–136, 2004.

[49] Tobias Dyck, Philipp Ober-Wörder, and Andreas Bund. Calculation of the wear surface and the coefficient of friction for various coated contact geometries. *Wear*, 368-369:390–399, 2016.

[50] Alan Shen, Dustin Caldwell, Anson W.K. Ma, and Sameh Dardona. Direct write fabrication of high-density parallel silver interconnects. *Additive Manufacturing*, 22 (2017):343–350, 2018.

[51] Woo Jin Hyun, Ethan B Secor, Mark C Hersam, C Daniel Frisbie, and Lorraine F Francis. High-resolution patterning of graphene by screen printing with a silicon stencil for highly flexible printed electronics. *Advanced Materials*, 27(1):109–115, 2015.

[52] Alan Shen, Dustin Caldwell, Anson W K Ma, and Sameh Dardona. Direct write fabrication of high-density parallel silver interconnects. *Additive Manufacturing*, 22: 343–350, 2018.

[53] Sen Wai Kwok, Kok Hin, Henry Goh, Zer Dong Tan, Siew Ting, Melissa Tan, Weng Weei Tjiu, Je Yeong Soh, Zheng Jie, Glenn Ng, Yan Zhi Chan, Hui Kim Hui, Kuan Eng, and Johnson Goh. Electrically conductive filament for 3D-printed circuits and sensors. *Applied Materials Today*, 9:167–175, 2017.

[54] Michael Dawoud, Iman Taha, and Samy J Ebeid. Strain sensing behaviour of 3D printed carbon black filled ABS. *Journal of Manufacturing Processes*, 35:337–342, 2018.

[55] Junhui Zhao, Kun Dai, Chenggang Liu, Guoqiang Zheng, Bo Wang, Chuntai Liu, Jingbo Chen, and Changyu Shen. A comparison between strain sensing behaviors of carbon black/polypropylene and carbon nanotubes/polypropylene electrically conductive composites. *Composites Part A: Applied Science and Manufacturing*, 48(1): 129–136, 2013.

[56] G Georgousis, C Pandis, A Kalamiotis, P Georgiopoulos, A Kyritsis, E Kontou, P Pissis, M Micusik, K Czanikova, J Kulicek, and M Omastova. Strain sensing in polymer/carbon nanotube composites by electrical resistance measurement. *Composites Part B: Engineering*, 68:162–169, 2015.

[57] Corinne Mattmann, Frank Clemens, and Gerhard Tröster. Sensor for Measuring Strain in Textile. *Sensors*, 8(6):3719–3732, 2008.

[58] Callen Votzke, Uranbileg Daalkhaijav, Yigit Mengue, and Matthew L Johnston. Highly-Stretchable Biomechanical Strain Sensor using Printed Liquid Metal Paste. In *IEEE Biomedical Circuits and Systems Conference*, pages 1–4, 2018.

[59] Takeo Yamada, Yuhei Hayamizu, Yuki Yamamoto, Yoshiki Yomogida, Ali Izadi-Najafabadi, Don N Futaba, and Kenji Hata. A stretchable carbon nanotube strain sensor for human-motion detection. *Nature Nanotechnology*, 6:296, 2011.

[60] Habib Nassar, Markellos Ntagios, William Taube Navaraj, and Ravinder Dahiya. Multi-material 3D Printed Bendable Smart Sensing Structures. In *IEEE Sensors*, pages 1–4, 2018.

[61] Khaled Elgeneidy, Gerhard Neumann, Michael Jackson, and Niels Lohse. Directly Printable Flexible Strain Sensors for Bending and Contact Feedback of Soft Actuators. *Frontiers in Robotics and AI*, 5(2):1–14, 2018.

[62] Iain A Anderson, Todd A Gisby, Thomas G McKay, Benjamin M O'Brien, and Emilio P Calius. Multi-functional dielectric elastomer artificial muscles for soft and smart machines. *Journal of Applied Physics*, 112(4), 2012.

[63] Andreas Frutiger, Joseph T Muth, and Daniel M Vogt. Capacitive soft strain sensors via multicore-shell fiber printing. *Advanced Materials*, 27(15):2440–2446, 2015.

[64] Lijia Pan, Alex Chortos, Guihua Yu, Yaqun Wang, Scott Isaacson, Ranulfo Allen, Yi Shi, Reinhold Dauskardt, and Zhenan Bao. An ultra-sensitive resistive pressure sensor based on hollow-sphere microstructure induced elasticity in conducting polymer film. *Nature Communications*, 5:1–8, 2014.

[65] A Nag, S Feng, S C Mukhopadhyay, J Kosel, and D Inglis. 3D printed mould-based graphite/PDMS sensor for low-force applications. *Sensors and Actuators, A: Physical*, 280:525–534, 2018.

[66] Joseph T Muth, Daniel M Vogt, Ryan L Truby, David B Kolesky, Robert J Wood, and Jennifer A Lewis. Embedded 3D Printing of Strain Sensors within Highly Stretchable Elastomers. *Advanced Materials*, 26(36):6307–6312, 2014.

[67] Chiranjit Ghosh and Vishnu Priye. Suppression of four-wave mixing in a 22 $\times$ 10 Gbps dense wavelength division multiplexed system by linearly chirped fiber Bragg gratings. *Optical and Quantum Electronics*, 51(1):5, 2018.

[68] Nobuhira Tanaka, Yoji Okabe, and Nobuo Takeda. Temperature-compensated strain measurement using fiber Bragg grating sensors embedded in composite laminates. *Smart Materials and Structures*, 12(6):940–946, 2003.

[69] Chiranjit Ghosh and Vishnu Priye. Temperature compensated high resolution interrogation of FBG strain sensor based on four wave mixing. *IEEE Sensors Journal*, 2020.

[70] Wu Yuan, Alessio Stefani, and Ole Bang. Tunable Polymer Fiber Bragg Grating (FBG) Inscription: Fabrication of Dual-FBG Temperature Compensated Polymer Optical Fiber Strain Sensors. *IEEE Photonics Technology Letters*, 24(5):401–403, 2012.

[71] Wen Wang, Xufeng Xue, Shuyao Fan, Mengwei Liu, Yong Liang, and Minghui Lu. Development of a wireless and passive temperature-compensated SAW strain sensor. *Sensors and Actuators, A: Physical*, 308, 2020.

[72] Bobo Gu, Wu Yuan, Sailing He, and Ole Bang. Temperature Compensated Strain Sensor Based on Cascaded Sagnac Interferometers and All-Solid Birefringent Hybrid Photonic Crystal Fibers. *IEEE Sensors Journal*, 12(6):1641–1646, 2012.

[73] Ming Wen, Xinchun Guan, Hui Li, and Jinping Ou. Temperature characteristics of thick-film resistors and its application as a strain sensor with low temperature-sensitivity. *Sensors and Actuators, A: Physical*, 301:111779, 2020.

[74] Rajarajan Ramalingame, Jose Roberto Bautista-Quijano, Danrlei de Farias Alves, and Olfa Kanoun. Temperature Self-Compensated Strain Sensors based on MWCNT-Graphene Hybrid Nanocomposite. *Journal of Composites Science*, 3(4): 96, 2019.

[75] Daniel Zymelka, Kazuyoshi Togashi, Ryoichi Ohigashi, Takahiro Yamashita, Seiichi Takamatsu, Toshihiro Itoh, and Takeshi Kobayashi. Printed strain sensor array for application to structural health monitoring. *Smart Materials and Structures*, 26(10), 2017.

[76] Daniel Gräbner, Gerrit Dumstorff, and Walter Lang. Simultaneous Measurement of Strain and Temperature with two Resistive Strain Gauges made from Different Materials. *Procedia Manufacturing*, 24:258–263, 2018.

[77] M. Maiwald, C. Werner, V. Zoellmer, and M. Busse. INKtelligent printed strain gauges. *Sensors and Actuators, A: Physical*, 162(2):198–201, 2010.

[78] Bradley Thompson and Hwan Sik Yoon. Aerosol-printed strain sensor using PEDOT:PSS. *IEEE Sensors Journal*, 13(11):4256–4263, 2013.

[79] Ibtesam R. K. Al-Saedi, Farag Mahel Mohammed, and Saifaldeen S Obayes. CNC machine based on embedded wireless and Internet of Things for workshop development. In *Int. Conf. on Control, Automation and Diagnosis*, pages 439–444, 2017.

[80] Anees Mohammad and Sinisa Djurovic. Evaluation of fiber-optic sensing performance for embedded thermal monitoring of electric machinery wound components. In *Mediterranean Conf. on Embedded Computing*, pages 72–76, 2016.

[81] Jonathan Gutleber, Jeffrey Brogan, R.J. Gambino, Christopher Gouldstone, Robert Greenlaw, Sanjay Sampath, Jon Longtin, and Dongming Zhu. Embedded Temperature and Heat Flux Sensors for Advanced Health Monitoring of Turbine Engine Components. In *IEEE Aerospace Conference*, volume 2006, pages 1–9, 2006.

[82] Andreas Wickberg, Jonathan B. Mueller, Yatin J. Mange, Joachim Fischer, Thomas Nann, and Martin Wegener. Three-dimensional micro-printing of temperature sensors based on up-conversion luminescence. *Applied Physics Letters*, 106(13), 2015.

[83] Shicong Wang, Meisong Tong, Yangyang Guan, and Manos M. Tentzeris. 3D Printed Inverted-F Antenna and Temperature Sensor using Microfluidics Technologies. In *IEEE Int. Symposium on Antennas and Propagation and USNC-URSI Radio Science Meeting*, pages 599–600, 2019.

[84] Anya Traille, Sofiene Bouaziz, Stephane Pinon, Patrick Pons, Herve Aubert, Ali Boukabache, and Manos Tentzeris. A wireless passive RCS-based temperature sensor using liquid metal and microfluidics technologies. In *European Microwave Conference*, number October, pages 45–48, 2011.

[85] J. Courbat, Y.B. Kim, D. Briand, and N.F. de Rooij. Inkjet printing on paper for the realization of humidity and temperature sensors. In *Int. Solid-State Sensors, Actuators and Microsystems Conference*, pages 1356–1359, 2011.

[86] Elizabeth Sauerbrunn, Ying Chen, Jeffrey Didion, Miao Yu, Elisabeth Smela, and Hugh A. Bruck. Thermal imaging using polymer nanocomposite temperature sensors. *Applications and Materials Science*, 212(10):2239–2245, 2015.

[87] Shingo Harada, Wataru Honda, Takayuki Arie, Seiji Akita, and Kuniharu Takei. Fully Printed, Highly Sensitive Multifunctional Artificial Electronic Whisker Arrays Integrated with Strain and Temperature Sensors. *ACS Nano*, 8(4):3921–3927, 2014.

[88] Raffaella Di Sante. Fibre Optic Sensors for Structural Health Monitoring of Aircraft Composite Structures: Recent Advances and Applications. *Sensors*, 15(8):18666–18713, 2015.

[89] P Antunes, H Lima, H Varum, and P André. Static and dynamic structural monitoring based on optical fiber sensors. In *Int. Conf. on Transparent Optical Networks*, pages 1–4, 2010.

[90] Jianfei Wang, Yang Yu, Yu Chen, Hong Luo, and Zhou Meng. Research of a double fiber Bragg gratings vibration sensor with temperature and cross axis insensitive. *Optik*, 126(7):749–753, 2015.

[91] Mohd Mansoor Khan, Nishtha Panwar, and Ravi Dhawan. Modified cantilever beam shaped FBG based accelerometer with self temperature compensation. *Sensors and Actuators A: Physical*, 205:79–85, 2014.

[92] Li Wei, Dazhou Jiang, Lingling Yu, Hengchun Li, and Zhuang Liu. A novel miniaturized fiber bragg grating vibration sensor. *IEEE Sensors Journal*, 19(24):11932–11940, 2019.

[93] Bojan Igrec, Marko Bosiljevac, Zvonimir Sipus, Dubravko Babic, and Smiljko Rudan. Fiber optic vibration sensor for high-power electric machines realized using 3D printing technology. In *Photonic Instrumentation Engineering III*, volume 9754, page 975410, 2016.

[94] Dogan Sinar and George K. Knopf. Disposable piezoelectric vibration sensors with PDMS/ZnO transducers on printed graphene-cellulose electrodes. *Sensors and Actuators A: Physical*, 302:111800, 2020.

[95] Rui Zhang and Oliver Amft. Bite Glasses - Measuring chewing using EMG and bone vibration in smart eyeglasses. In *ACM Int. Symposium on Wearable Computers*, pages 50–52, 2016.

[96] Yuanzhao Wu, Yiwei Liu, Youlin Zhou, Qikui Man, Chao Hu, Waqas Asghar, Fali Li, Zhe Yu, Jie Shang, Gang Liu, Meiyong Liao, and Run Wei Li. A skin-inspired tactile sensor for smart prosthetics. *Science Robotics*, 3(22), 2018.

[97] Nicolas Godard, Lucas Allirol, Antoine Latour, Sebastjan Glinsek, Mathieu Gérard, Jérôme Polesel, Fabrice Domingues Dos Santos, and Emmanuel Defay. 1-mW Vibration Energy Harvester Based on a Cantilever with Printed Polymer Multilayers. *Cell Reports Physical Science*, 1(6):100068, 2020.

[98] Bin Yang, Chengkuo Lee, Wenfeng Xiang, Jin Xie, Johnny Han He, Rama Krishna Kotlanka, Siew Ping Low, and Hanhua Feng. Electromagnetic energy harvesting from vibrations of multiple frequencies. *Journal of Micromechanics and Microengineering*, 19(3):035001, 2009.

[99] Qian Zhang and Eun Sok Kim. Vibration Energy Harvesting Based on Magnet and Coil Arrays for Watt-Level Handheld Power Source. *Proceedings of the IEEE*, 102 (11):1747–1761, 2014.

[100] B. Kawa, K. Sliwa, R. Walczak, and V. C. Lee. Inkjet 3D printed vibrational energy harvester. In *Int. Conf. on Micro and Nanotechnology for Power Generation and Energy Conversion Applications*, pages 1–4, 2019.

[101] Control Engineering Europe. Positive displacement meters suited to use in desalination plants, 2013. URL `https://www.controlengeurope.com/article/60935/Positive-displacement-meters-suited-to-use-in-desalination-plants.aspx`.

[102] Sierra Instruments. Improve Boiler Efficiency with Mass Flow Meter Solutions. URL `https://www.sierrainstruments.com/library/tags/boiler-efficiency`.

[103] Primnath Rambissoon. Measuring liquid in half filled pipes. *World Pumps*, 2010(9): 10–12, 2010.

[104] Andrew Godley. Flow measurement in partially filled closed conduits. *Flow Measurement and Instrumentation*, 13(5-6):197–201, 2002.

[105] Ying Yan Qu, Terry Lucke, and Simon Beecham. Measuring Flows in Partially-Filled Pipes in Siphonic Roof Drainage Systems. *Mapan*, 26(4):315–327, 2011.

[106] H Eren. Accuracy in real time ultrasonic applications and transit-time flow meters. In *IEEE Instrumentation and Measurement Technology Conference*, volume 1, pages 568–572, 1998.

[107] N Svedin, E Stemme, and G Stemme. A static turbine flow meter with a micromachined silicon torque sensor. *Journal of Microelectromechanical Systems*, 12(6): 937–946, 2003.

[108] A L S Salustiano Martim, J G Dalfré Filho, Y.D.F.L. De Lucca, and A I Borri Genovez. Electromagnetic flowmeter evaluation in real facilities: Velocity profiles and error analysis. *Flow Measurement and Instrumentation*, 66:44–49, 2019.

[109] Yao Yu Yang and Shih Chung Kang. Crowd-based velocimetry for surface flows. *Advanced Engineering Informatics*, 32:275–286, 2017.

[110] Krohne. Tidalflux 2300 F Technical Datasheet. Technical report, 2013.

[111] ABB Automation Products. Electromagnetic Flowmeter FXP4000. Technical report, 2007.

[112] TOSHIBA. Electromagnetic Flowmeter for Partially-filled Pipes. Technical report, 2019.

[113] Mace USA LLC. XCi Product Manual. Technical report. URL `https://www.instrumart.com/assets/Mace-XCi-Manual.pdf`.

[114] Teledyne Isco. 2150 Area Velocity Flow Module and Sensor. Technical Report November, 2018.

[115] HACH Company. FLO-DAR AV Sensor. Technical report, 2016.

[116] ISCO. Laser Flow Non-Contact Subsurface Velocity Sensor. Technical report, 2018.

[117] Brajesh Kumar, G Rajita, and Nirupama Mandal. A review on capacitive-type sensor for measurement of height of liquid level. *Measurement and Control*, 47(7): 219–224, 2014.

[118] Massimo Arattano and Lorenzo Marchi. Systems and sensors for Debris-flow monitoring and warning. *Sensors*, 8(4):2436–2452, 2008.

[119] N Muhammad Fathur Rahman, Salama Manjang, and Zahir Zainuddin. Water level monitoring using ultrasonic-pipe in open channel. In *Int. Conf. on Quality in Research*, pages 262–266, 2017.

[120] W Liu, G Xie, and L Yang. Research on High-precision Real-time Online Measurement of Liquid Level Changes. In *WASE Int. Conf. on Information Engineering*, volume 1, pages 107–110, 2010.

[121] L Zhu, L Dong, S Liu, and D Sun. Self-adaptive frequency estimation algorithm of improving liquid level measurement precision of LFMCW radar. In *Int. Conf. on Microwave and Millimeter Wave Technology*, pages 1626–1628, 2010.

[122] J Chen and X Xu. A New Level Measurement Method of Acoustic Standing Wave Based on Particle Filter. In *International Workshop on Intelligent Systems and Applications*, pages 1–4, 2009.

[123] P Dr\uagan, M St\uanese, and I Na\cscu. Camera-based liquid level measurement using the refractive properties of the medium. In *IEEE Int. Conf. on Automation, Quality and Testing, Robotics*, pages 1–6, 2018.

[124] Y U Jaehyoung and Hahn Hernsoo. Remote detection and monitoring of a water level using narrow band channel. *Journal of Information Science and Engineering*, 26(1):71–82, 2010.

[125] K Loizou, E Koutroulis, D Zalikas, and G Liontas. A low-cost capacitive sensor for water level monitoring in large-scale storage tanks. In *IEEE Int. Conf. on Industrial Technology*, pages 1416–1421, 2015.

[126] G Lu, M Seto, and K Shida. A new proposal of multi-functional level meter. In *IEEE Int. Conf. on Multisensor Fusion and Integration for Intelligent Systems*, pages 209–212, 2003.

[127] Satish Chandra Bera, Jayanta Kumar Ray, and Subrata Chattopadhyay. A low-cost noncontact capacitance-type level transducer for a conducting liquid. *IEEE Transactions on Instrumentation and Measurement*, 55(3):778–786, 2006.

[128] Hüseyin Canbolat. A novel level measurement technique using three capacitive sensors for liquids. *IEEE Transactions on Instrumentation and Measurement*, 58(10): 3762–3768, 2009.

[129] Huadong Wu. *Sensor Data Fusion for Context-Aware Computing Using Dempster-Shafer Theory*. PhD thesis, 2003.

[130] Lauro Snidaro, Ingrid Visentini, and Gian Luca Foresti. Data Fusion in Modern Surveillance. In *Innovations in Defence Support Systems - 3*, pages 1–21. Springer, 2011.

[131] Won Jae Yi, Oishee Sarkar, Sivisa Mathavan, and Jafar Saniie. Wearable sensor data fusion for remote health assessment and fall detection. In *IEEE Int. Conf. on Electro Information Technology*, pages 303–307, 2014.

[132] Khim Chhantyal, Hakon Viumdal, Saba Mylvaganam, and Geir Elseth. Ultrasonic level sensors for flowmetering of non-Newtonian fluids in open Venturi channels. In *Sensors Applications Symposium*, pages 110–115, 2016.

[133] Wen Li, Qingfang Zhang, Xueke Luo, and Xu Chen. New Method of Flow Measurements Based on CFD for Partially Filled Pipe. In *Int. Conf. on Mathematics, Modeling, Simulation and Statistics Application*, volume 164, pages 49–53, 2019.

[134] Pan Haipeng and Zhou Tianrui. Generation and optimization of slice profile data in rapid prototyping and manufacturing. *Journal of Materials Processing Technology*, 187-188:623–626, 2007.

[135] W Cao and Y Miyamoto. Direct Slicing from AutoCAD Solid Models for Rapid Prototyping. *International Journal of Advanced Manufacturing Technology*, 21(10-11):739–742, 2003.

[136] C C Chang. Direct slicing and G-code contour for rapid prototyping machine of UV resin spray using PowerSOLUTION macro commands. *International Journal of Advanced Manufacturing Technology*, 23(5-6):358–365, 2004.

[137] S H Choi and K T Kwok. Hierarchical slice contours for layered-manufacturing. *Computers in Industry*, 48(3):219–239, 2002.

[138] M Y Zhou. STEP-based approach for direct slicing of CAD models for layered manufacturing. *International Journal of Production Research*, 43(15):3273–3285, 2005.

[139] Jing Hu. Study On STL-Based Slicing Process For 3D Printing. In *Proceedings of the 28th Annual International Solid Freeform Fabrication Symposium*, pages 885–895, 2017.

[140] Zhengyan Zhang and Sanjay Joshi. An improved slicing algorithm with efficient contour construction using STL files. *International Journal of Advanced Manufacturing Technology*, 80(5-8):1347–1362, 2015.

[141] C F Kirschman and C C Jara-Almonte. A parallel slicing algorithm for solid freeform fabrication processes. In *International Solid Freeform Fabrication Symposium*, page 26–33, 1992.

[142] Pinghai Yang and Xiaoping Oian. Adaptive slicing of moving least squares surfaces: Toward direct manufacturing of point set surfaces. *Journal of Computing and Information Science in Engineering*, 8(3):433–442, 2008.

[143] S H Sun, H W Chiang, and M I Lee. Adaptive direct slicing of a commercial CAD model for use in rapid prototyping. *The International Journal of Advanced Manufacturing Technology*, 34(7-8):689–701, 2007.

[144] Hyung Jung Kim, Kyung Hoon Wie, Sung Hoon Ahn, Heon Seong Choo, and Cha Soo Jun. Slicing algorithm for polyhedral models based on vertex shifting. *International Journal of Precision Engineering and Manufacturing*, 11(5):803–807, 2010.

[145] Oliver Porges, Roberto Lampariello, Jordi Artigas, Armin Wedler, Gerhard Grunwald, Christoph Borst, and A Roa. Reachability and Dexterity: Analysis and Applications for Space Robotics. In *Symposium on Advanced Space Technologies in Robotics and Automation*, number 3, pages 1–7, 2015.

[146] Christoph Borst, Franziska Zacharias, Christoph Borst, and Gerd Hirzinger. Capturing robot workspace structure : Representing robot capabilities. In *Int. Conf. on Intelligent Robots and Systems*, number 2007, pages 3229–3236, 2016.

[147] R H Sturges. A Quantification of Machine Dexterity Applied to an Assembly Task. *The International Journal of Robotics Research*, 9(3):49–62, 1990.

[148] Sheila Sutjipto, Daniel Tish, Gavin Paul, Teresa Vidal-Calleja, and Tim Schork. Towards Visual Feedback Loops for Robot-Controlled Additive Manufacturing. In *Robotic Fabrication in Architecture, Art and Design 2018*, pages 85–97. Springer International Publishing, 2019.

[149] Gang Zhao, Guocai Ma, Jiangwei Feng, and Wenlei Xiao. Nonplanar slicing and path generation methods for robotic additive manufacturing. *International Journal of Advanced Manufacturing Technology*, 96(9-12):3149–3159, 2018.

[150] F. A. Adnan, F R M Romlay, and M. Shafiq. Real-time slicing algorithm for Stereolithography (STL) CAD model applied in additive manufacturing industry. *IOP Conference Series: Materials Science and Engineering*, 342(1):012016, 2018.

[151] William Oropallo, Les A. Piegl, Paul Rosen, and Khairan Rajab. Point cloud slicing for 3-D printing. *Computer-Aided Design and Applications*, 15(1):90–97, 2018.

[152] Jiawei Feng, Jianzhong Fu, Zhiwei Lin, Ce Shang, and Bin Li. Direct slicing of T-spline surfaces for additive manufacturing. *Rapid Prototyping Journal*, 24(4), 2018.

[153] Donald A. Klosterman, Richard P. Chartoff, Nora R. Osborne, George A. Graves, Allan Lightman, Gyoowan Han, Akos Bezeredi, and Stan Rodrigues. Development of a curved layer LOM process for monolithic ceramics and ceramic matrix composites. *Rapid Prototyping Journal*, 5(2):61–71, 1999.

[154] Debapriya Chakraborty, B. Aneesh Reddy, and A. Roy Choudhury. Extruder path generation for Curved Layer Fused Deposition Modeling. *Computer-Aided Design*, 40(2):235–243, 2008.

[155] Peter Corke. *Robotics Vision and Control*, volume 75. Springer, 2 edition, 2015.

[156] Pasquale Chiacchio. A new dynamic manipulability ellipsoid for redundant manipulators. *Robotica*, 18(4):381–387, 2000.

[157] K Nagatani, T Hirayama, A Gofuku, and Y Tanaka. Motion planning for mobile manipulator with keeping manipulability. In *IEEE Int. Conf. on Intelligent Robots and Systems*, volume 2, pages 1663–1668, 2002.

[158] E Amir M Ghalamzan, Firas Abi-Farraj, Paolo Robuffo Giordano, and Rustam Stolkin. Human-in-the-loop optimisation: Mixed initiative grasping for optimally facilitating post-grasp manipulative actions. In *IEEE Int. Conf. on Intelligent Robots and Systems*, pages 3386–3393, 2017.

[159] Mario Selvaggio, Amir M Ghalamzan E, Rocco Moccia, Fanny Ficuciello, and Bruno Siciliano. Haptic-guided shared control for needle grasping optimization in minimally invasive robotic surgery. In *IEEE Int. Conf. on Intelligent Robots and Systems*, pages 3617–3623, 2019.

[160] Tommaso Pardi, Valerio Ortenzi, Colin Fairbairn, Tony Pipe, Amir Masoud Ghalamzan Esfahani, and Rustam Stolkin. Planning Maximum-Manipulability Cutting Paths. *IEEE Robotics and Automation Letters*, 5(2):1999–2006, 2020.

[161] Dov Kruger, Rustam Stolkin, Aaron Blum, and Joseph Briganti. Optimal AUV path planning for extended missions in complex, fast-flowing estuarine environments. In *IEEE Int. Conf. on Robotics and Automation*, number April, pages 4265–4270, 2007.

[162] Yu-Chi Lin and Dmitry Berenson. Humanoid Navigation Planning in Large Unstructured Environments Using Traversability - Based Segmentation. In *IEEE Int. Conf. on Intelligent Robots and Systems*, pages 7375–7382, 2018.

[163] Nikolaus Vahrenkamp, Tamim Asfour, Giorgio Metta, Giulio Sandini, and Rudiger Dillmann. Manipulability analysis. In *IEEE RAS Int. Conf. on Humanoid Robots*, pages 568–573, 2012.

[164] Peter Leven and Seth Hutchinson. Using manipulability to bias sampling during the construction of probabilistic roadmaps. In *IEEE Transactions on Robotics and Automation*, volume 2, pages 2134–2140, 2002.

[165] Riad Menasri, Amir Nakib, Hamouche Oulhadj, Boubaker Daachi, Patrick Siarry, and Gaetan Hains. Path planning for redundant manipulators using metaheuristic for bilevel optimization and maximum of manipulability. *IEEE Int. Conf. on Robotics and Biomimetics*, (12):145–150, 2013.

[166] Yi Tan and Limao Zhang. Computational methodologies for optimal sensor placement in structural health monitoring: A review. *Structural Health Monitoring*, 19 (4):1287–1308, 7 2020. ISSN 1475-9217.

[167] Hoon Sohn, Charles R Farrar, Francois Hemez, and Jerry Czarnecki. A Review of Structural Health Monitoring Literature. *Library.Lanl.Gov*, pages 1–7, 2001.

[168] Gavin Paul, Stephen Webb, Dikai Liu, and Gamini Dissanayake. Autonomous robot manipulator-based exploration and mapping system for bridge maintenance. *Robotics and Autonomous Systems*, 59(7):543–554, 2011.

[169] Wieslaw Ostachowicz, Rohan Soman, and Pawel Malinowski. Optimization of sensor placement for structural health monitoring: a review. *Structural Health Monitoring*, 18(3):963–988, 2019.

[170] L. Michael Santi, T. Shane Sowers, and Robert B. Aguilar. Optimal sensor selection for health monitoring systems. In *AIAA/ASME/SAE/ASEE Joint Propulsion Conference and Exhibit*, 2005.

[171] Ting-Hua Yi and Hong-Nan Li. Methodology Developments in Sensor Placement for Health Monitoring of Civil Infrastructures. *International Journal of Distributed Sensor Networks*, 8(8):612726, 8 2012. ISSN 1550-1477.

[172] Robert F Guratzsch and Sankaran Mahadevan. Structural Health Monitoring Sensor Placement Optimization Under Uncertainty. *American Institute of Aeronautics and Astronautics Journal*, 48(7):1281–1289, 2010.

[173] Ting-Hua Yi, Hong-Nan Li, and Ming Gu. A new method for optimal selection of sensor location on a high-rise building using simplified finite element model. *Structural Engineering and Mechanics*, 37(6):671–684, 2011.

[174] D.C. Kammer. Sensor Placement for On-Orbit Modal Identification and Correlation of Large Space Structures. In *IEEE American Control Conference*, number 1, pages 2984–2990, 1990.

[175] Cyrille Stephan. Sensor placement for modal identification. *Mechanical Systems and Signal Processing*, 27(1):461–470, 2012.

[176] Costas Papadimitriou and Geert Lombaert. The effect of prediction error correlation on optimal sensor placement in structural dynamics. *Mechanical Systems and Signal Processing*, 28:105–127, 2012.

[177] Costas Papadimitriou. Pareto optimal sensor locations for structural identification. *Computer Methods in Applied Mechanics and Engineering*, 194(12-16):1655–1673, 2005.

[178] Gavin Paul, Dikai Liu, Nathan Kirchner, and Gamini Dissanayake. An effective exploration approach to simultaneous mapping and surface material–type identification of complex three-dimensional environments. *Journal of Field Robotics*, 26 (11-12):915–933, 2009.

[179] M. Meo and G. Zumpano. On the optimal sensor placement techniques for a bridge structure. *Engineering Structures*, 27(10):1488–1497, 2005.

[180] Huidong Gao and Joseph L Rose. Sensor placement optimization in structural health monitoring using genetic and evolutionary algorithms. In *Smart Structures and Materials 2006: Sensors and Smart Structures Technologies for Civil, Mechanical, and Aerospace Systems*, volume 6174. International Society for Optics and Photonics, 2006.

[181] A Rama Mohan Rao and Ganesh Anandakumar. Optimal placement of sensors for structural system identification and health monitoring using a hybrid swarm intelligence technique. *Smart materials and Structures*, 16(6):2658, 2007.

[182] Stefka Fidanova, Pencho Marinov, and Enrique Alba. Ant algorithm for optimal sensor deployment. In *Computational intelligence*, pages 21–29. Springer, 2012.

[183] Liu Fuqing and Zhang Lingmi. Successive method for optimal placement of actuators and sensors. *Journal of Astronautics*, 3(21):64–69, 2000.

[184] Jian-Fu Lin, You-Lin Xu, and Siu-Seong Law. Structural damage detection-oriented multi-type sensor placement with multi-objective optimization. *Journal of Sound and Vibration*, 422:568–589, 2018.

[185] Hyun Hwang, Jun Han Bae, and Byung Cheol Min. Design guidelines for sensor locations on 3D printed prosthetic hands. In *IEEE Int. Conf. on Robotic Computing*, pages 412–417, 2017.

[186] N H Cook. Tool wear sensors. *Wear*, 62(62):49–57, 1980.

[187] Protopasta. Electrically Conductive Composite PLA, 2021. URL `https://www.proto-pasta.com/products/conductive-pla`.

[188] National Instruments. Measuring Strain with Strain Gauges. Technical report, 2016. URL `http://www.ni.com/white-paper/3642/en/`.

[189] National Instruments. Measuring Strain with Strain Gages. Technical report, 2015. URL `https://www.ni.com/en-au/innovations/white-papers/07/measuring-strain-with-strain-gages.html`.

[190] Keith R. Cheatle. *Fundamentals of Test Measurement Instrumentation*. 2006.

[191] University of Delaware. Design Studio: Instron E10000, 2021. URL `https://me.udel.edu/academics/design-studio/equipment/instron-e10000/`.

[192] Prusa Research. Original Prusa i3 Multi Material 2.0 - Prusa3D, 2021. URL `https://www.prusa3d.com/original-prusa-i3-multi-material-2-0/`.

[193] ASTM International. ASTM D638-14, Standard Test Method for Tensile Properties of Plastics, 2014. URL `www.astm.org`.

[194] TENMA. Function / Arbitrary Waveform Generator. Technical report, 2018.

[195] Keysight-Technologies. Keysight InfiniiVision 2000 X-Series Oscilloscopes. Technical report, 2000.

[196] Matej Simurda, Lars Duggen, Benny Lassen, and Nils T Basse. Modelling of transit-time ultrasonic flow meters under multi-phase flow conditions. *IEEE International Ultrasonics Symposium*, pages 1–6, 2016.

[197] Ltd Dalian Hipeak Instruments Development Co. Ultrasonic Flow Meter User Manual. Technical report.

[198] A Schroder, M Kupnik, P O'Leary, E Benes, and M Groschl. A Capacitance Ultrasonic Transducer With Micromachined Backplate for Fast Flow Measurements in Hot Pulsating Gases. *IEEE Sensors Journal*, 6(4):898–905, 2006.

[199] Larry Conrad Keven;Lynnworth. Fundamentals of Ultrasonic Flow Meters. *Journal of Chemical Information and Modeling*, 200:52–61, 2002.

[200] Texas Instruments. FDC1004 4-Channel capacitance-to-digital converter for capacitive sensing solutions. *Data Sheet*, pages 1–33, 2015.

[201] Wang and David. Capacitive-Based Liquid Level Sensing Sensor Reference Design. Technical Report January, 2015. URL `www.ti.com`.

[202] M Szilvási-Nagy and Gy Mátyási. Analysis of STL Files. *Mathematical and Computer Modelling*, 38(7-9):945–960, 2003.

[203] P. Corke. Robotics Toolbox. URL `https://petercorke.com/toolboxes/robotics-toolbox/`.

[204] John Q Gan, Eimei Oyama, Eric M Resales, and Huosheng Hu. A complete analytical solution to the inverse kinematics of the Pioneer 2 robotic arm. *Robotica*, 23(1):123–129, 2005.

[205] Pannawit Srisuk, Adna Sento, and Yuttana Kitjaidure. Inverse kinematics solution using neural networks from forward kinematics equations. In *Int. Conf. on Knowledge and Smart Technology*, pages 61–65, 2017.

[206] D Manocha and J F Canny. Efficient inverse kinematics for general 6R manipulators. *IEEE Transactions on Robotics and Automation*, 10(5):648–657, 1994.

[207] Pratik J Parikh and Sarah S Y Lam. A hybrid strategy to solve the forward kinematics problem in parallel manipulators. *IEEE Transactions on Robotics*, 21(1):18–25, 2005.

[208] T Yoshikawa. Manipulability and redundancy control of robotic mechanisms. In *IEEE Int. Conf. on Robotics and Automation*, volume 2, pages 1004–1009, 1985.

[209] 3D point cloud and mesh processing software Open Source Project, 2021. URL `https://cloudcompare.org/`.

[210] Yahya Bougdid and Zouheir Sekkat. Voxels Optimization in 3D Laser Nanoprinting. *Scientific Reports*, 10(1):10409, 2020.

[211] J E Lavín-Delgado, J E Solís-Pérez, J F Gómez-Aguilar, and R F Escobar-Jiménez. A New Fractional-Order Mask for Image Edge Detection Based on Caputo–Fabrizio Fractional-Order Derivative Without Singular Kernel. *Circuits, Systems, and Signal Processing*, 39(3):1419–1448, 2020.

[212] W Wijaya, M.A. Ali, R Umer, K.A. Khan, P.A. Kelly, and S Bickerton. An automatic methodology to CT-scans of 2D woven textile fabrics to structured finite element and voxel meshes. *Composites Part A: Applied Science and Manufacturing*, 125: 105561, 2019.

[213] K B Rahmat, D Dharma, and A Manaf. Rendering Speed Improvement for Particle Based Fluid Simulation on GVDB Voxels using Whitted Raytracing. In *Int. Conf. on Data and Software Engineering*, pages 1–6, 2019.

[214] G Paul, L Liu, and D Liu. A novel approach to steel rivet detection in poorly illuminated steel structural environments. In *Int. Conf. on Control, Automation, Robotics and Vision*, pages 1–7, 2016.

[215] T I Zohdi. Rapid Voxel-Based Digital-Computation for Complex Microstructured Media. *Archives of Computational Methods in Engineering*, 26(5):1379–1394, 2019.

[216] Jay Hoon Jung, Yousun Shin, and YoungMin Kwon. Extension of convolutional neural network with general image processing kernels. In *IEEE Region 10 Conference*, pages 1436–1439, 2018.

[217] Shafaq B Chaudhry, Victor C Hung, Ratan K Guha, and Kenneth O Stanley. Pareto-based evolutionary computational approach for wireless sensor placement. *Engineering Applications of Artificial Intelligence*, 24(3):409–425, 2011.